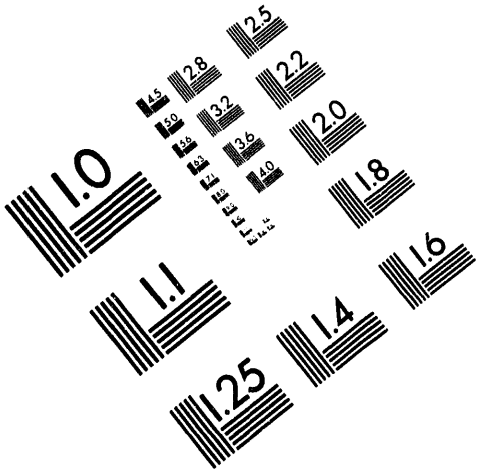

Association for Information and Image Management

1100 Wayne Avenue, Suite 1100
Silver Spring, Maryland 20910

301/587-8202

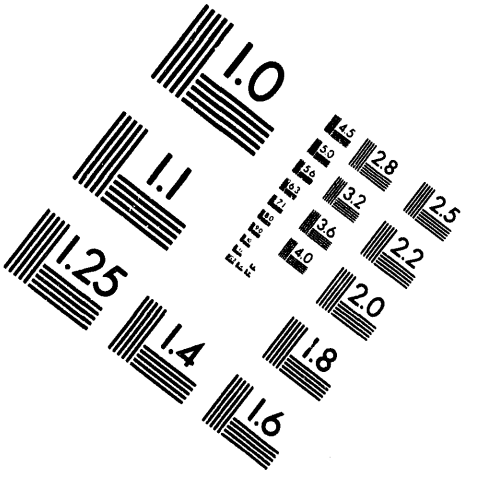

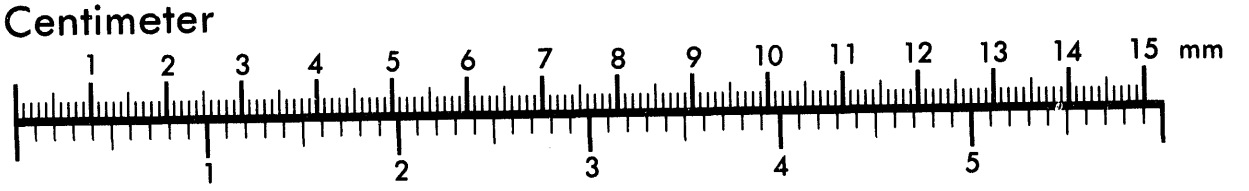

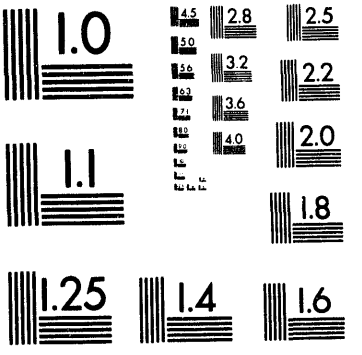

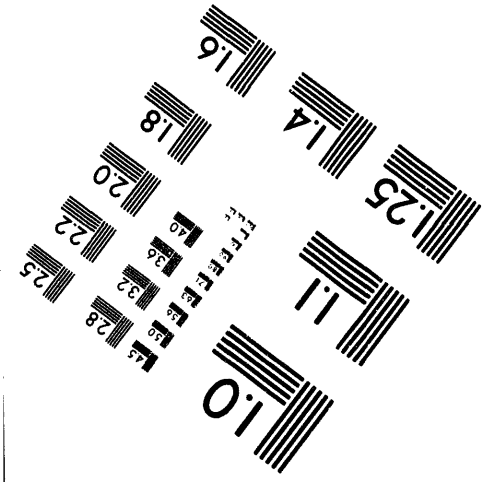

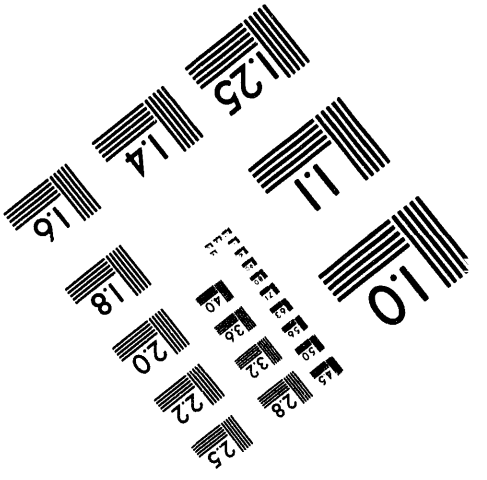

MANUFACTURED TO AIIM STANDARDS
BY APPLIED IMAGE, INC.

1 of 2

LBL-35671

Resonant Tunneling in Small Current-Biased Josephson Junctions

John Mark Schmidt
(Ph.D. Thesis)

Department of Physics, University of California
and
Materials Science Division,
Lawrence Berkeley Laboratory,
University of California,
Berkeley, CA 94720

May 1994

This work was supported by the California Competitive Technology Program and by the Director, Office of Energy Research, Office of Basic Energy Sciences, Materials Sciences Division of the U.S. Department of Energy under contract number DE-AC03-76SF00098.

Resonant Tunneling in Small Current-Biased Josephson Junctions

by

John Mark Schmidt

Resonant Tunneling in Small Current-Biased Josephson Junctions

by

John Mark Schmidt

ABSTRACT

The effects of resonant tunneling between bound quantum states of a macroscopic system is studied both theoretically and experimentally. The macroscopic system studied theoretically is the current-biased Josephson tunnel junction. Several novel effects are predicted to arise as a result of resonant tunneling, including a series of voltage peaks along the supercurrent branch of the current-voltage characteristic, and the enhancement of the rate of escape from the zero voltage state to the voltage state at particular values of bias current. A theoretical model is developed which is used to estimate the magnitude and duration of the voltage peaks, and to estimate the enhancement of the escape rate, which appears as peaks in the rate as a function of bias current.

An experimental investigation was carried out in an attempt to observe these predicted peaks in the escape rate distribution. The device used in this study was the current-biased DC SQUID, which is shown to be in the appropriate limit dynamically equivalent to a Josephson junction with an adjustable critical current. DC SQUIDs with capacitances of 15 to 37 fF and critical currents of 160 to 300 nA were fabricated from aluminum using electron-beam lithography and bilayer resist shadow mask techniques. Electrical contact to each SQUID was made through high resistance thin film leads located on the substrate. These resistors provided a high impedance at the plasma frequency which is shown to be necessary for the isolation of the SQUID from its

electromagnetic environment. Measurements were carried out on a dilution refrigerator at temperatures as low as 19 mK. No evidence was found for resonant tunneling. This is attributed to effective temperatures of hundreds of millikelvin, as indicated by the observed SQUID behavior. The behavior is well explained by a heating model where the high effective temperatures are generated by the ohmic heating of the electron gas of the isolation resistors, which decouples from the phonon system in an effect known as the hot electron effect. The prospects for further theoretical and experimental research are discussed.

TABLE OF CONTENTS

ACKNOWLEDGMENTS

I would first like to thank my advisor, Professor John Clarke, for all his contributions made throughout my long association with his group. He showed great confidence in me by taking me on at an early stage, and maintained confidence and provided support throughout the course of my research, including many frustrating periods. I owe much of my development as a scientist to the environment he provided.

I acknowledge the receipt of financial support during the course of my graduate work, which came in the form of a fellowship from the National Science Foundation and a stipend from the United States Department of Energy, administered through Lawrence Berkeley Laboratory.

Several members of the UC Berkeley faculty deserve my special thanks. I am grateful to Professor Theodore Van Duzer of the Electrical Engineering department for the free and unlimited use of his scanning electron microscope, which I used to perform all of my electron beam lithography. The work in this thesis probably could not have been performed without the use of this machine, which during most of this project was the only e-beam lithography system available at UC Berkeley and perhaps in the Bay Area. I must thank Professor Dan Rokhsar of the Physics department for useful discussions, and in particular for providing certain "magic words" which allowed me to advance my theoretical model past a particular spot at which I was stuck. In addition, I thank him for performing a critical reading of a manuscript.

I would like to both thank and complement the staff of the Microfabrication Laboratory. They provided ready assistance every time I needed it, and operate an astonishingly efficient and professional laboratory.

The staff of the Physics department deserves my thanks for much of the behind the scene support I received over the years. The machinists in the shop receive my admiration for their excellent skills. In particular I would like to thank Andy Brocato, the machinist who made most of the gadgets I requested, for his fine work, ready assistance, artful welding, and unique sense of humor. I would also like to thank Al Daft, who remarkably managed to keep both the student shop and his sanity in excellent shape for many years despite the unwitting diametrical efforts of the shop users. Several people helped to unravel the red tape and fight the forces of bureaucracy which can bog down a student trying to focus on his research. I would like to thank the Clarke group's assistants, Rita Jones and Barbara Salisbury. In Student Services, I thank Anne Takizawa and fondly remember Ken Miller.

I must thank the members of the Clarke group, both past and present. Some of these members were here far enough in the past that I have never met them; however I have benefited from the use of equipment they designed or constructed. The members I have overlapped with I thank for providing me with helpful suggestions, illuminating discussions, the loans of equipment often made in a pinch, and an always friendly environment. In particular I must thank those with whom I shared the B231 Birge Hall laboratory for almost a third of each day for almost a third of my life: Andrew Cleland, Mark Ferrari, Tim Shaw, Dave Cooperberg, Alex Rimberg, and Teressa Ho. I could not help but become good friends with these people, not because we were all trapped together in a room with no windows for so long, but because I was fortunate that they are all such friendly, helpful, talented, and generally wonderful people (and thank goodness they are, for we *were* all trapped together in a room with no windows for so long!). In particular I thank Mark Ferrari for providing great friendship, humor, and for patiently participating in the hundreds of conversations I initiated with a description of the washboard potential. I cannot overstate the positive impact Andrew Cleland has had on my experience at Berkeley. He taught me a great deal about experimental physics by patiently and

thoroughly explaining on countless occasions some piece of physics or experimental technique. He has a remarkable sense of strategy and can get to the heart of a problem very quickly, and frequently used his insight to provide me with crucial suggestions. Working with him was truly an honor and a pleasure, and I only hope to have absorbed some of his many talents.

Finally, I thank my friends both inside and outside the physics community for all their support and for helping me keep a healthy perspective. I thank my family for their love and support, and especially thank my parents, who provided for and endured the particularly long education of their child. Most importantly, I thank my wife Serena for her unfailing love, care, and companionship.

CHAPTER 1

Introduction

In exploring the validity of the application of quantum mechanics to macroscopic systems [1, 2], one often chooses the current-biased Josephson junction as a system to study, both theoretically and experimentally. The phase difference ϕ between the superconducting condensates in the electrodes obeys an equation of motion identical to that of a particle moving in a cosine potential that is tilted in proportion to the bias current [3, 4]. The kinetic energy of the particle is characterized by the charging energy $E_C = e^2/2C$ of the junction capacitance C, while the amplitude of the cosine potential is characterized by the Josephson coupling energy $E_J = \hbar I_C/2e$, where I_C is the critical current of the junction. For bias currents below I_C, this "tilted washboard" potential consists of a set of wells in which the particle can be trapped, whereas above the critical current the particle can move freely down the potential. Treating this macroscopic system quantum mechanically, one expects to find distinctly non-classical features. Two such features occur in junctions having $E_J >> E_C$ and have been verified experimentally. One is the existence of quasi-bound states in the wells with discrete energy levels [5], demonstrated with microwave spectroscopy techniques. The other is the macroscopic quantum tunneling of the particle from one of these bound states into the continuous

spectrum of free running states [6-10]. In this limit, the phase ϕ is localized and can be treated semi-classically.

In the past several years a great deal of both theoretical and experimental research [11-13] has been focused on the opposite low-capacitance (femtofarad) limit $E_C >> E_J$ where the barriers are reduced to the point where the particle is free except for a weak periodic potential. Here the charging energy becomes the dominant energy scale, and the charge transfer process dominates the dynamics. In the quantum mechanical description, the charge on the junction capacitor which is the variable conjugate to ϕ becomes a highly localized semi-classical variable, while the phase wavefunction becomes extended, as dictated by the uncertainty principle. One of the novel quantum mechanical effects predicted for such a system is coherent Bloch wave oscillations [11].

In the intermediate regime $E_C \approx E_J$ each well contains only a few states. These states are still quasi-bound, but the coupling between states in other wells is greatly increased. The possibility of another quantum-mechanical process occurring in this regime has been suggested [14, 15], namely the quantum tunneling from one of the bound states of a potential well into another bound state in an adjacent well. This process, called resonant tunneling, occurs when the bias current is such that the ground state energy of one well is equal to the energy of an excited state in the adjacent well. The tunneling between the two states is coherent; when the system is prepared in one of the states, which are not eigenstates of the Hamiltonian, it will oscillate in time between the two. This is analogous to the well-known ammonia molecule resonance, and to the predicted macroscopic quantum coherent superposition of states of an rf-SQUID [1, 2]. One important distinction between the case of the SQUID and the problem at hand is that in the former case the resonance studied is between two local ground states, whereas in the latter case one of the states is excited.

Once the system has undergone a resonant tunneling transition to an excited state, it can either decay to a lower state, or continue to tunnel. These competing processes

each lead to observably distinct results in the behavior of the junction. If, after tunneling to the excited state, the system decays to the local ground state, the entire process may repeat, resulting in the movement of the particle from well to well down the potential (path A in Fig. 1-1). Because this motion corresponds to a nonzero voltage across the junction, we expect that the resonant tunneling process will be reflected in the supercurrent portion of the current-voltage characteristic as a series of voltage spikes (Fig. 1-2 (a)), each spike corresponding to an aligned pair of states. This structure is unusual in that it can occur for bias currents which are much less than the critical current. This macroscopic process is similar to that occurring in semiconductor superlattices at the microscopic level [16, 17], where increases in conductivity are observed when a strong electric field brings electronic energy levels of adjacent wells into alignment. In contrast to the process of sequential tunneling and decay, additional resonant tunneling events occurring before the decay to the ground state could lead eventually to the transition of the system to the free running state (path B in Fig. 1-1), thereby destroying the spike structure. Here one should instead observe a switching of the junction from the supercurrent branch to the quasiparticle branch at a value of bias current below the thermodynamic critical current (Fig. 1-2 (b)).

Resonant tunneling in a Josephson junction is of interest not only as a novel phenomenon in its own right, but also because of its possible effect on the coherent Bloch oscillations. It has been suggested [18] that for values of bias current in the vicinity of the resonances the resonant tunneling transition to excited states will break the coherence of the Bloch oscillations. The importance of the resonant tunneling transition was also noted by Kondo [19], who, in order to examine the suppression of Bloch oscillations by Zener tunneling, numerically integrated the Schrödinger equation for this system. The wavefunctions he obtained explicitly show the resonance, although the dynamics of the resonant transition were not investigated in that work.

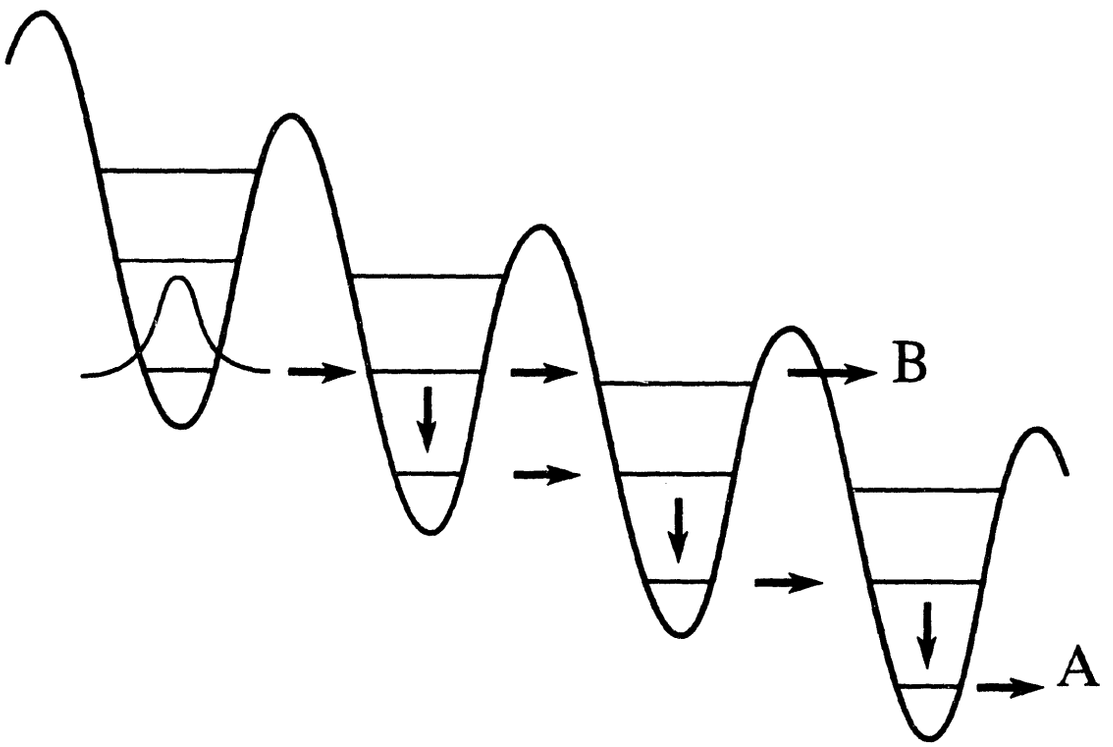

FIGURE 1-1. Two possible transition paths for the particle started in a ground state. Motion along path A, an alternating sequence of resonant tunneling and decay transitions, results in steady phase slips. Motion along path B, which is a sequence of successive resonant tunneling transitions, results in escape to the free-running state.

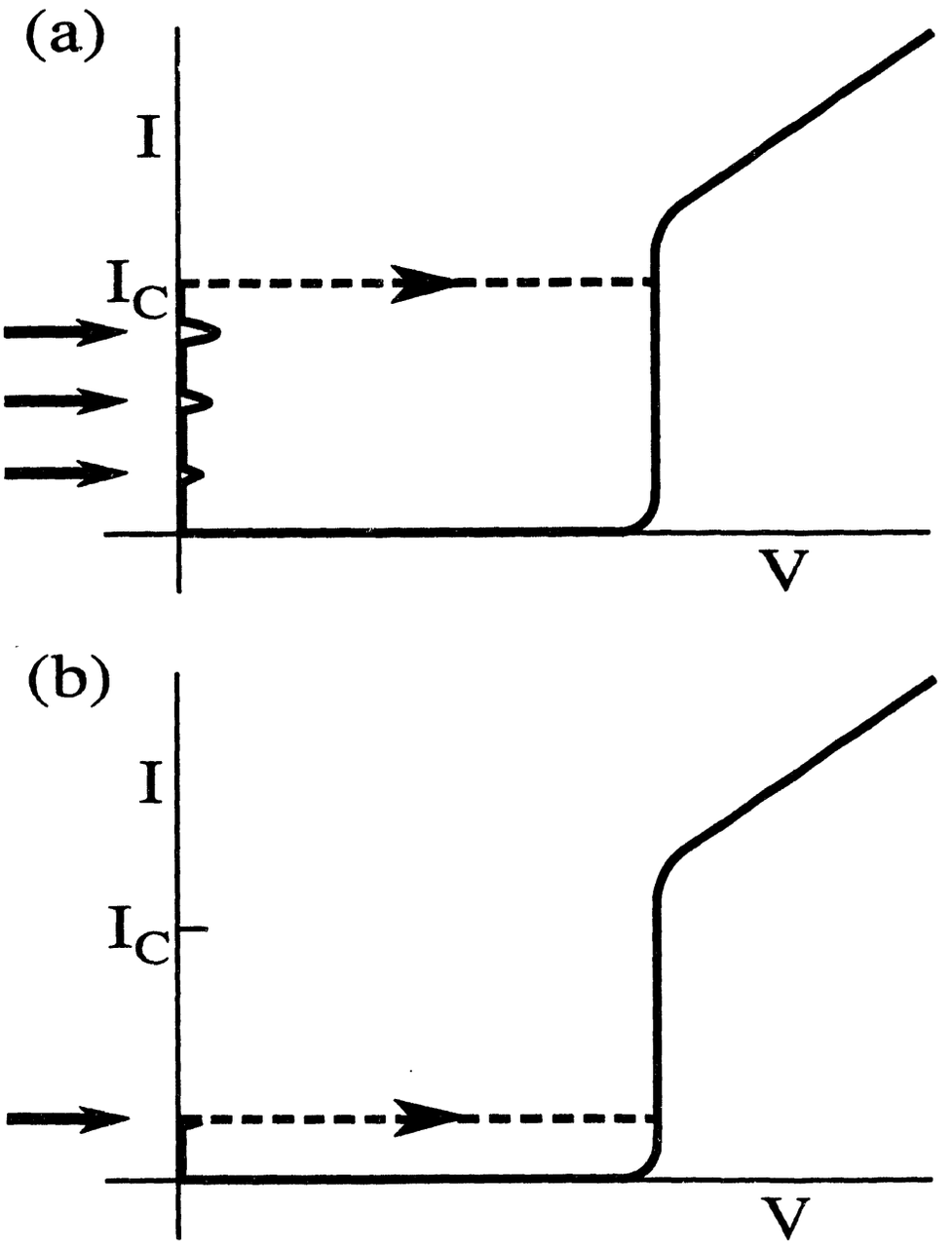

FIGURE 1-2. Schematic representations of the current-voltage characteristic: (a) steady phase slips (path A in Fig. 1-1) result in voltage peaks along the supercurrent branch which correspond to the alignment of energy levels; (b) escape (path B in Fig. 1-1) results in a switching current greatly reduced from the thermodynamic critical current I_C. These features are indicated by arrows.

The study of resonant tunneling could also shed light on a long-standing debate over whether the potential described above should be defined over the extended interval $[-\infty,\infty]$ or merely over the finite interval $[0, 2\pi]$. Classically these two descriptions are identical, but in a quantum mechanical description differences arise when the wavefunction extends over lengths greater than 2π. A gedanken experiment, which treats a single junction as the limiting case of an rf SQUID with an infinitely large superconducting loop, argues in favor of the infinite interval [11]. However, many hold that the phase defined over an interval greater than a 2π is physically meaningless. Resonant tunneling implicitly requires an infinite interval because it is essentially the coherent superposition of wavefunctions which are offset from each other by 2π. An experimental verification of its existence would support the validity of the infinite interval, although some authors have shown [20] using a finite interval approach that certain resonances can appear at the same values of bias current that the infinite interval treatment predicts resonances to occur.

In this thesis, I present my studies of the phenomenon of resonant tunneling, both theoretical and experimental. The theoretical studies were undertaken first in order to develop the framework necessary to design an experiment intended to demonstrate the existence of the effect. Although other authors had undertaken theoretical studies of the resonant tunneling phenomenon in Josephson junctions, these early studies [15, 21] had not taken into account all the features of the problem which we believe to be important. Most notable among these are the coherence of the tunneling, and the competition between decay and successive tunneling. The coherence of the transition from one bound state to another must be included because the probability of return tunneling is not necessarily negligible, implying that Fermi's Golden Rule may be invalid in some situations. Although decay and successive tunneling rates are directly compared in ref. [21], I suspected that these quantities require a more detailed consideration within the context of the dynamics of the system. Zhuravlev and Zorin [22] concurrently developed

a theory employing a similar approach to mine which includes the coherence of the resonant tunneling transition. However, they did not estimate the energies of the states in the wells beyond a harmonic approximation. The anharmonicity of the potential has important implications for the dynamics, for it creates a misalignment of levels at resonance which acts to suppress subsequent tunneling once an initial resonant tunneling event occurs, and thus suppresses escape to the free-running state. To what extent this misalignment would act to suppress escape, and to what extent damping would tend to oppose this suppression through lifetime broadening was an open question when I undertook this research. Because of these weaknesses in the existing theory, I developed the model which is presented in Chapter 2. This theory takes into account in a comprehensive manner all of the aspects of the problem mentioned above. However, many important additional considerations were left out of my model as well, because of the relative difficulty involved in including them. Because these are important for an experimental study of the effect, I have included a survey of these topics in Chapters 3.

To my knowledge no previous experimental work had been performed on Josephson junctions in this limit as a primary focus of the research. One investigation [13] which focused on the charging limit included a few junctions in the intermediate limit, but these devices did not have well characterized measuring circuitry. The external loading of junctions has been demonstrated to be of primary importance in determining the dynamics of tunnel junctions both in the large capacitance [9, 10, 23] ($E_J >> E_C$) and small capacitance [24, 25] ($E_C >> E_J$) limits, so it was most certainly a necessary consideration in the intermediate regime as well. This is substantiated by the experimental work which most closely paralleled my research, completed by Kautz and Martinis [26] at about the time I had completed my theoretical work. Their measurements were performed on devices in a parameter range similar to mine and also utilized a measuring setup similar to mine. Their results could be explained by models which were entirely classical and relied heavily on the accurate modeling of the

measuring circuitry. Although their measurements were carried out at temperatures too great to observe resonant tunneling and the observed behavior was adequately described by classical mechanics, their results form a very important basis for understanding Josephson junctions in this limit as one makes the transition to the quantum-dominated behavior where resonant tunneling is predicted to occur. For this reason their results which are most relevant to my work are discussed in Chapter 3.

This background of experimental and theoretical work allowed me to design and carry out an experiment to search for a signature of resonant tunneling. The strategy of my approach is discussed in Chapter 4, and details of my experimental technique are given in Chapter 5.

The results of these measurements are presented in Chapter 6. Although I had long anticipated it as a potential problem, my results clearly demonstrate that ohmic heating problematically increased the temperature of the devices I tested to well above the temperatures where resonant tunneling is expected to occur. These devices were constructed according to the requirements dictated by the models outlined in Chapters 2-4, used in conjunction with the approach I chose to demonstrate the effect. Unfortunately, the model which best explains the heating behavior also implies there is little one can do to avoid this problem by using variants of my approach. A discussion of some possible minor improvements is given in Chapter 7.

Although these experimental results are discouraging as far as demonstrating the resonant tunneling phenomenon, they serve to identify some of the important features of devices operating in this regime, and verify the validity of several of the results obtained in the theoretical discussion. Thus, these results will be important in directing any further experimental work toward identifying the effect.

CHAPTER 2

A Model Theory of Resonant Tunneling

In this chapter I present my model theory for the resonant tunneling effect. As noted in the introduction, it is by no means a complete theory, but provides a significant advance over theories existing at the time of its development, and using its results I can conclude which effects due to resonant tunneling are observable experimentally. Most of the results in this chapter were presented previously [27].

I estimate the magnitude, width, and duration of the voltage peak developed before the junction switches to the normal state, and the rate at which this switching occurs. These quantities are computed for a range of junction parameters. My approach is as follows: The analysis is for zero temperature, and I consider the effects of dissipation only to supply a decay mechanism, neglecting its effect on tunneling rates [28, 29]. Using a perturbative technique, I calculate the energy levels of the quasi-bound states, starting with a harmonic approximation in each well. I use the WKB method to estimate the coupling between states in adjacent wells and the tunneling rate to the free running states. I then use a density matrix approach to investigate the motion of the system when the junction is biased at or near resonance. In this way I am able to include both coherent and incoherent transitions in a comprehensive manner.

The results of this theory imply that the most readily observable signature of resonant tunneling in a Josephson junction is not the voltage peaks, but rather the unique distribution of rates at which the junction switches to the normal state. This distribution is non-monotonic in the bias current, exhibiting peaks at values of current corresponding to resonances.

2.1 The Resistively Shunted Junction Model

Many of the essential features of Josephson junction behavior can be understood by using the resistively shunted junction (RSJ) model [3, 4], which describes the junction's electrical characteristics through the classical dynamics of the coordinate ϕ, which is the phase difference between the superconducting condensates of the electrodes. This model is consequently the logical starting point for understanding macroscopic quantum behavior exhibited by the junction as well. In this model, the junction is described by the circuit illustrated in Fig. 2-1. It consists of an ideal Josephson element with critical current I_c in parallel with a capacitance C and a shunt resistance R. The Josephson element obeys the current and voltage relationships

$$I = I_c \sin\phi \tag{2-1}$$

and

$$V = \frac{\hbar}{2e}\dot{\phi} \ , \tag{2-2}$$

and its critical current at temperature T is given by the Ambegaokar and Baratoff [30] relation

$$I_c = \frac{\pi\Delta(T)}{2eR_N}\tanh\frac{\Delta(T)}{2k_BT} \tag{2-3}$$

in the weak-coupling limit. Here R_N is the normal tunnel resistance of the junction, and $\Delta(T)$ is the superconducting gap parameter for the electrode material, which I assume is the same for both electrodes for simplicity, and k_B is Boltzmann's constant. Strictly speaking, the shunt resistance R is a constant in the RSJ model, but a common extension of the model is to replace this element with a more general element, possibly nonlinear,

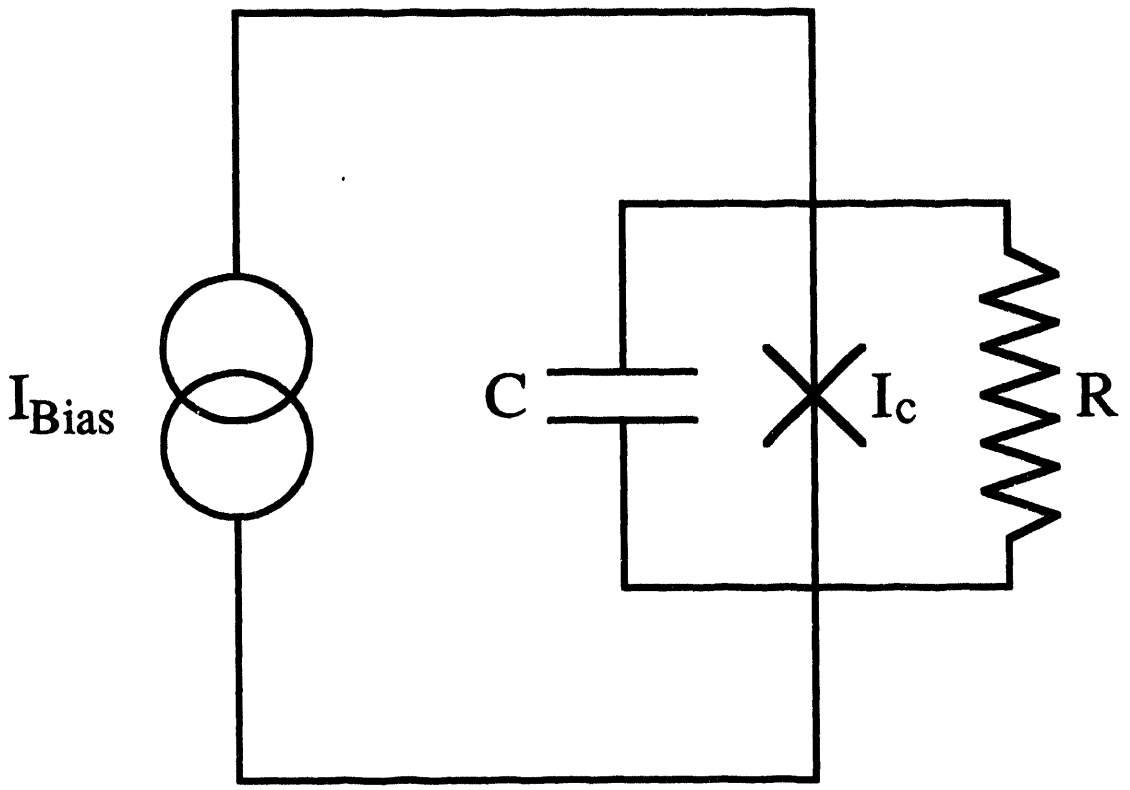

FIGURE 2-1. Circuit diagram for the Resistively Shunted Junction (RSJ) model.

which more accurately represents the circuit in parallel with the junction, including the effects of quasiparticle and leakage currents in the junction and other external circuitry attached to the junction. This type of model will be considered in greater detail in Chapter 3. For the present I will assume a simple ohmic shunt, although I have allowed the value of R to possibly differ from the tunnel resistance R_N. When the junction is biased with a constant current I_{Bias}, Kirchoff's law may be applied along with Eqs. (2-1) and (2-2) to yield the equation of motion

$$\left(\frac{\hbar}{2e}\right)^2 C\ddot{\phi} + \left(\frac{\hbar}{2e}\right)^2 \frac{1}{R}\dot{\phi} + \left(\frac{\hbar}{2e}\right) I_c \sin\phi = \left(\frac{\hbar}{2e}\right) I_{Bias} \quad . \tag{2-4}$$

This is the equation of motion for a particle with mass proportional to the capacitance which experiences viscous damping inversely proportional to the resistance, subject to a force which can be derived from the potential

$$\tilde{V}(\phi) = -E_J \cos\phi - E_J \frac{I_{Bias}}{I_c}\phi \tag{2-5}$$

where $E_J = \hbar I_c/2e$ is the Josephson coupling energy.

To quantize this system, I must obtain the Hamiltonian. To do so, I must drop the damping term in Eq. (2-4). The damping will be reintroduced later as a perturbation to the system. The Hamiltonian is given by

$$\tilde{H} = -4E_C \frac{d^2}{d\phi^2} - E_J \cos\phi - \frac{I}{I_c} E_J \phi \tag{2-6}$$

where $E_C = e^2/2C$ is the charging energy for the junction capacitance. This Hamiltonian is the starting point for the quantum mechanical description of this macroscopic system.

2.2 Harmonic Oscillator Approximation and Perturbative Solutions

Multiple Harmonic Wells Approximation

I will now obtain approximate solutions to the time independent Schrödinger equation obtained using the Hamiltonian given in Eq. (2-6). Focusing on the well located at the origin, one can separate $\tilde{H}$ into harmonic and anharmonic parts by writing

$$\tilde{H} = \tilde{H}^0_{SHO} + \Delta\tilde{H} \ , \tag{2-7}$$

where $\tilde{H}^0_{SHO}$ is the Hamiltonian for the simple harmonic oscillator,

$$\tilde{H}^0_{SHO} = -4E_C \frac{d^2}{d\phi^2} + \frac{E_J}{2}\phi^2 - E_J \ , \tag{2-8}$$

and $\Delta\tilde{H}$ contains the term linear in ϕ together with quartic and higher order terms. If the eigenfunctions of $\tilde{H}^0_{SHO}$ are sufficiently localized, the harmonic Hamiltonian will allow me to obtain approximate solutions for the energies of the states localized in this well of the washboard potential, and I may consider $\Delta\tilde{H}$ as a perturbation to $\tilde{H}^0_{SHO}$.

For ease of algebraic manipulation I define the parameter $\nu = \sqrt{E_J / 2E_C}$ and let $\phi = x\sqrt{2/\nu}$. Physically, ν corresponds roughly to the number of levels in the well. In addition, I choose the energy unit to be the zero point energy of the oscillator $\sqrt{2E_C E_J} = \hbar\omega_p / 2$ (ω_p is 2π times the plasma frequency). I thus obtain (dropping the tilde in these units)

$$H^0_{SHO} = -\frac{d^2}{dx^2} + x^2 - \nu \ , \tag{2-9}$$

which has the energy spectrum

$$E_m^0 = -\nu + 2m + 1, \qquad (m = 0, 1, 2, \ldots) \ . \tag{2-10}$$

In these units, the full Hamiltonian (2-6) is given by

$$H = -\frac{d^2}{dx^2} + V(x) \ , \tag{2-11}$$

where V(x) is the potential

$$V(x) = \nu\cos(x\sqrt{2/\nu}) - sx\sqrt{2\nu} \ , \tag{2-12}$$

and s is the reduced current $s = I_{Bias}/I_C$. The energy spectrum of H forms a Wannier-Stark ladder. Thus, given the levels E_m located in a particular well, I can generate the full set of levels

$$F_{n,m} = E_m - 2\pi s\nu n \ , \tag{2-13}$$

where n is the integer which labels the nth well. If I take E_m^0 as an approximation to the actual levels E_m, I find that at particular values of bias current $I_{Bias} = I_m^{res}$ the ground state of the nth well is degenerate with the mth state of the (n + 1)th well, that is

$$F_{n,0} = F_{n+1,m} \ , \tag{2-14}$$

when

$$I_m^{res} = I_c \frac{m}{\pi\nu} = m\frac{e}{\pi}\omega_p \ . \tag{2-15}$$

This is the condition for resonance obtained previously [14, 15, 18]. Note that in this approximation the resonance peaks will be equally spaced along the current axis. Also, note that the degeneracies which occur at resonance are multiple. For example, at $I = I_m^{res}$, $F_{n+1,m} = F_{n+2,2m}$ in addition to the degeneracy given by Eq. (2-14), and so on. This implies that successive resonant tunneling events may be an important transition sequence. Therefore, I next investigate to what extent these additional degeneracies are removed by the inclusion of corrections to $F_{n,m}$.

Energy Level Corrections

I wish to calculate the corrections $\Delta E_m = E_m - E_m^0$ for the energy levels which appear upon inclusion of the anharmonic perturbation ΔH. These corrections can be obtained using time-independent perturbation theory with harmonic oscillator eigenfunctions as a basis, and the results expanded as a power series in $1/\nu$. This assumes that the coupling to the states in adjacent wells is negligible, which I will show later is justified.

To obtain corrections of order ν^{-2} one must carry the linear term in ΔH to fourth order in a perturbation expansion, noting that s is of order ν^{-1} at resonance. This is unnecessarily tedious; instead I can expand the potential about the minimum of the 0th well, which is located at $x_0 = \sqrt{\nu/2}\sin^{-1}s$. Letting $x = x_0 + \Delta x$, I can write Eq. (2-11) as

$$H = H_{SHO}^2 + H_s + H_a \tag{2-16}$$

where

$$H_{SHO}^2 = \frac{d^2}{d\Delta x^2} + \sqrt{1-s^2}(\nu + \Delta x^2) - s\nu\sin^{-1}s\ , \tag{2-17}$$

$$H_s = \sqrt{1-s^2}\left[\nu - \Delta x^2 - \nu\cos(\Delta x\sqrt{2/\nu})\right], \tag{2-18}$$

and

$$H_a = sv\left[\sin(\Delta x\sqrt{2/v}) - \Delta x\sqrt{2/v}\right] \ . \qquad (2\text{-}19)$$

Since H_S is of order v^{-1}, it must be carried to second order. On the other hand, H_a is of order $v^{-3/2}$ and need only be retained to first order, and its contribution vanishes by parity. I can now recombine H^2_{SHO} and H_S; the resulting Schrödinger equation takes the form of Mathieu's differential equation. Using the asymptotic expansion for the characteristic values of this equation [31], I obtain to second order in $1/v$:

$$\Delta E_m = \frac{vs^2}{2} - \frac{ws^2}{4} - \frac{w^2+1}{16v} - \frac{w^3+3w}{256v^2} \ , \qquad (2\text{-}20)$$

where $w = 2m + 1$.

The dependence of ΔE_m on m shows the levels E_m are not evenly spaced, which means degeneracies only occur in pairs for a given bias current. This will have important consequences for the dynamics for it will tend to suppress sequential resonant tunneling events. By including this correction to the energy levels and using Eq. (2-14) I obtain the value of the bias current at resonance to second order in $1/v$:

$$I_m^{res} = m\frac{e}{\pi}\omega_p\left[1 - \frac{m+1}{8n} - \frac{m^2}{4\pi^2v^2} - \frac{2m^2+3m+3}{128v^2}\right] \ . \qquad (2\text{-}21)$$

Note that because of the anharmonicity of the potential the resonance peaks are not evenly spaced along the current axis.

Coupling Between Wells

Next I consider the coupling between states of different wells. I estimate the matrix elements $H_{n,m,n',m'}$ when the states are degenerate, that is, $F_{n,m} = F_{n',m'}$. We

assume nearest neighbor coupling only, so that $H_{n,m,n',m'} = 0$ for $|n - n'| > 1$. For $n' - n = 1$, I use the WKB method to extend the harmonic oscillator wavefunctions into the region under the barrier. With these semiclassical wavefunctions I obtain estimates of the matrix elements, which are independent of n and are given by

$$H_{0,m,1,m'} = \frac{1}{\pi}\sqrt{G(m)G(m')}\exp(-I_m) \ , \tag{2-22}$$

where

$$I_m = \int_{x_m^-}^{x_m^+}[V(x') - E_m]^{1/2}dx' \ . \tag{2-23}$$

The limits of the integral are the classical turning points where the integrand is zero, and V and E_m are evaluated at the bias current where $F_{0,m} = F_{1,m'}$. The dimensionless parameter G(m) is of order unity and depends weakly on the level index m:

$$G(m) = \frac{\pi^{1/2}}{2^m m!}\left[\frac{2m+1}{e}\right]^{m+1/2} \ . \tag{2-24}$$

Note that the coupling decreases exponentially with the barrier height. The coupling is quite small for values of ν of interest ($\nu \gtrsim 2$), which justifies the earlier assumption that the inter-well coupling is weak.

2.3 Dynamics

General Considerations

Having determined the matrix elements of the Hamiltonian in the basis of states localized in the wells, I am now equipped to study the motion of the system. In particular, I wish to answer two questions: What is the average rate of motion of the particle down the washboard, and how long will this motion persist before the particle undergoes a transition to a free running state? The average rate of motion determines the voltage across the junction before it switches to the normal state, and the lifetime of the process determines the time during which one has to measure this voltage and the distribution of rates at which the junction switches.

I restrict my analysis to the case of the bias current I_{Bias} set at or near its first resonance value I_1^{res}. Here the system consists of a set of bound states which can be subdivided into groups of ℓ_{max} degenerate or nearly degenerate states, where ℓ_{max} is the number of bound states in a well, and each state in a group is from a different well. For convenience, I label states in the kth group, or subsystem, as $\Psi_{k\ell}$, where $k = n - m$ and $\ell = m + 1$ with $k = ..., -2, -1, 0, 1, 2, ...$ and $\ell = 1, 2, ..., \ell_{max}$ (see Fig. 2-2). Within one of these subsystems the states $\Psi_{k\ell}$ are no longer eigenstates, but are mixed because of the nonzero coupling between them. This results in coherent motion among states $\Psi_{k\ell}$ with the same k when the subsystem is started in one of them. In addition to this coherent motion within a subsystem, two types of incoherent transitions out of the subsystem are possible. One is the decay to a state in a lower subsystem, leading to motion down the washboard, and the other is the tunneling from a state $\Psi_{k\ell_{max}}$ to the continuum of free running states, resulting in the junction switching into the normal state. As I perform this calculation in the zero temperature limit, I do not consider thermally induced transitions.

In light of the above, I adopt the following general method of solution: I associate with each subsystem k its density matrix ρ^k, which is of dimension $\ell_{max} \times \ell_{max}$, and

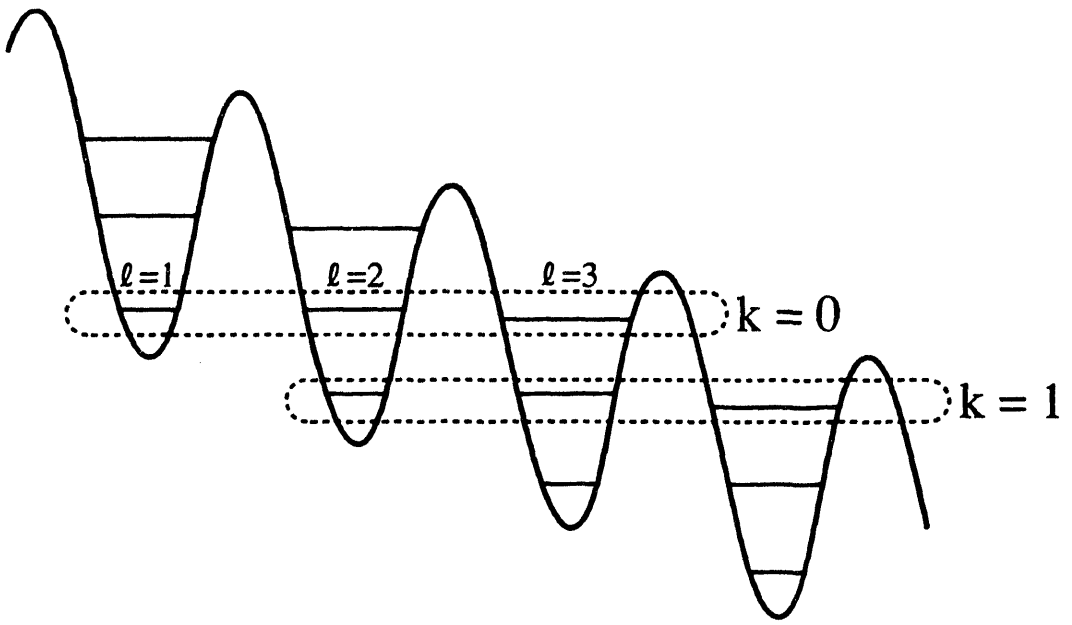

FIGURE 2-2. Subsystems for $\ell_{max} = 3$ (three states per subsystem). The subsystems for k = 0 and k = 1 are each enclosed by the dashed oval.

examine the equations of motion for the entire set of density matrices. Each of these contains terms associated with the coherent motion within that subsystem, and terms representing the incoherent coupling to other subsystems and the set of free running states.

Resonant Tunneling Peak Magnitude and Shape

First I investigate the motion of the system which leads to peak structure on the supercurrent branch of the current-voltage characteristic, shown as path A in Fig. 1-1. The states involved in this motion are Ψ_{k1} and Ψ_{k2} with k = 0, 1, 2, ... Here I exclude the effects of additional states $\Psi_{k\ell}$ with $\ell > 2$, and ignore the possibility of escape. I shall show later that in the cases where the peak structure has a significant lifetime these result only in a small perturbation to the overall motion down the potential; in addition the general method is most clearly illustrated in this simple case and can be extended to include escape in a straightforward way.

Coherent motion within the kth subsystem is described by the matrix representation H_0 of the Hamiltonian in the basis $\{\Psi_{k1}, \Psi_{k2}\}$. Before being coupled, these states differ in energy by an amount σ, which to lowest order in $1/\nu$ depends on the bias current I_{Bias} as

$$\sigma = 2\pi\nu(I_{Bias} - I_1^{res}) / I_c \ . \tag{2-25}$$

Taking the reference energy to be halfway between these energies, I have

$$H_0 = \begin{bmatrix} \frac{\sigma}{2} & \frac{\Delta_1}{2} \\ \frac{\Delta_1}{2} & \frac{-\sigma}{2} \end{bmatrix} , \tag{2-26}$$

where I have defined $\frac{\Delta_1}{2} \equiv H_{0,0,1,1}$ for brevity in notation.

The decay of a state Ψ_{k2} to $\Psi_{k+1,1}$ is induced by damping in the system. The term which represents damping in the classical system cannot be represented in the Hamiltonian formulation used here. However, damping can be added as a perturbation by coupling the system to a large set of harmonic oscillators which receive the energy lost through damping [28, 29]. These oscillators replace the resistive shunt R of the RSJ model and therefore represent the electromagnetic environment coupled to the junction. In my model of resonant tunneling, I include the decay phenomenologically by adding an imaginary term $-i\Gamma_d/2$ (again in units of $\hbar\omega_p/2$) to the energy of state Ψ_{k2}; this results in a characteristic decay rate of $\tilde{\Gamma}_d = \omega_p\Gamma_d/2$ expressed in actual inverse time units. By using the harmonic oscillator bath model of the damping, Esteve, Devoret, and Martinis [32] calculated the complex energy shifts for a macroscopic system subject to damping. In Chapter 3 I will review their results, and show that for the RSJ model their analysis yields a decay rate $\Gamma_d = 2/Q$, where $Q = RC\omega_p$ is the classical quality factor. This result is obtained using a harmonic oscillator approximation for the well of the washboard potential and assuming an ohmic shunt resistor R which provides sufficiently small damping such that $Q >> 1$. This provides me with a rough estimate for Γ_d. The imaginary terms representing decay can be added to the representation of the Hamiltonian as the matrix $-i\Gamma/2$, where

$$\Gamma = \begin{bmatrix} 0 & 0 \\ 0 & \Gamma_d \end{bmatrix} . \tag{2-27}$$

Now suppose that the particle is localized in state Ψ_{01} at time $t = 0$. The usual equation of motion for the density matrix ρ^0 of dimension 2×2 of the $k = 0$ subsystem is modified by the presence of imaginary energy terms; it is now

$$\frac{d}{d\tau}\rho^0 = -i[H_0,\rho^k] - \frac{1}{2}[\Gamma,\rho^k]_+ \ , \qquad (2\text{-}28)$$

where the differentiation is carried out with respect to the dimensionless time variable $\tau = \omega_p t/2$. Equation (2-28) can be solved analytically. The result shows the trace of ρ^0 is not conserved: probability density leaves the $k = 0$ subsystem because of the imaginary energy terms.

Consider next the subsystems with $k > 0$. The probability density leaving a particular subsystem k–1 enters the subsystem k incoherently in the state Ψ_{k1}, where it again begins coherent motion and further decay. I thus include a source term in each of the equations of motion for these subsystems, which become

$$\frac{d}{d\tau}\rho^0 = -i[H_0,\rho^k] - \frac{1}{2}[\Gamma,\rho^k]_+ + \begin{bmatrix} 1 & 0 \\ 0 & 0 \end{bmatrix}\frac{d}{d\tau}\left[1 - \sum_{i=0}^{k-1} \mathrm{Tr}\,\rho^i\right] , \qquad (2\text{-}29)$$

with

$$\rho^k(\tau = 0) = 0 \qquad (k > 0) \ .$$

These equations can be written in a much simpler form by replacing each of the 2×2 density matrices ρ^k by a vector $\tilde{\rho}^k = (\rho^k_{11}, \rho^k_{12}, \rho^k_{21}, \rho^k_{22})^T$, where T indicates the transpose. The system of Eqs. (2-28) and (2-29) then becomes

$$\frac{d}{d\tau}\tilde{\rho}^0 = A\tilde{\rho}^0 \qquad (2\text{-}30)$$

and

$$\frac{d}{d\tau}\tilde{\rho}^k = A\tilde{\rho}^k + B\tilde{\rho}^{k-1} \qquad (k > 0) \qquad (2\text{-}31)$$

with

$$A = \begin{bmatrix} 0 & \frac{i\Delta_1}{2} & \frac{-i\Delta_1}{2} & 0 \\ \frac{i\Delta_1}{2} & \frac{-\Gamma_d}{2} - i\sigma & 0 & \frac{-i\Delta_1}{2} \\ \frac{-i\Delta_1}{2} & 0 & \frac{-\Gamma_d}{2} + i\sigma & \frac{i\Delta_1}{2} \\ 0 & \frac{-i\Delta_1}{2} & \frac{i\Delta_1}{2} & -\Gamma_d \end{bmatrix} \tag{2-32}$$

and

$$B = \begin{bmatrix} 0 & 0 & 0 & \Gamma_d \\ 0 & 0 & 0 & 0 \\ 0 & 0 & 0 & 0 \\ 0 & 0 & 0 & 0 \end{bmatrix} . \tag{2-33}$$

These equations can be solved for any finite number of subsystems since a given subsystem is coupled only to subsystems above it. The result for eight subsystems with $\sigma = 0$ (on resonance) and $\Delta_1 = \Gamma_d$, computed numerically, is shown in Fig. 2-3. Plotting the trace of the density matrix for each subsystem, one can follow the propagation of probability density down the washboard, noting that there is a distribution of rates of motion due to the stochastic nature of the decay process. This distribution appears as a spreading of the quantities Tr $\rho^k(\tau)$ in τ as k increases.

I am now in a position to estimate the expectation value of the rate of motion down the potential. The expectation value for the phase $\langle\phi\rangle$ is given by

$$\frac{\langle\phi\rangle}{2\pi} = \sum_{k=1}^{\infty} k(\rho_{11}^k + \rho_{22}^k) . \tag{2-34}$$

I find that, after an initial transient on the order of the transition time out of the k = 0 subsystem, $\langle\phi\rangle$ is linear in τ. I define γ as the slope of $\langle\phi\rangle/2\pi$ in this region, that is, $(d/d\tau)\langle\phi\rangle/2\pi \rightarrow \gamma$ as $\tau \rightarrow \infty$. I take γ to be the rate of steady motion down the potential,

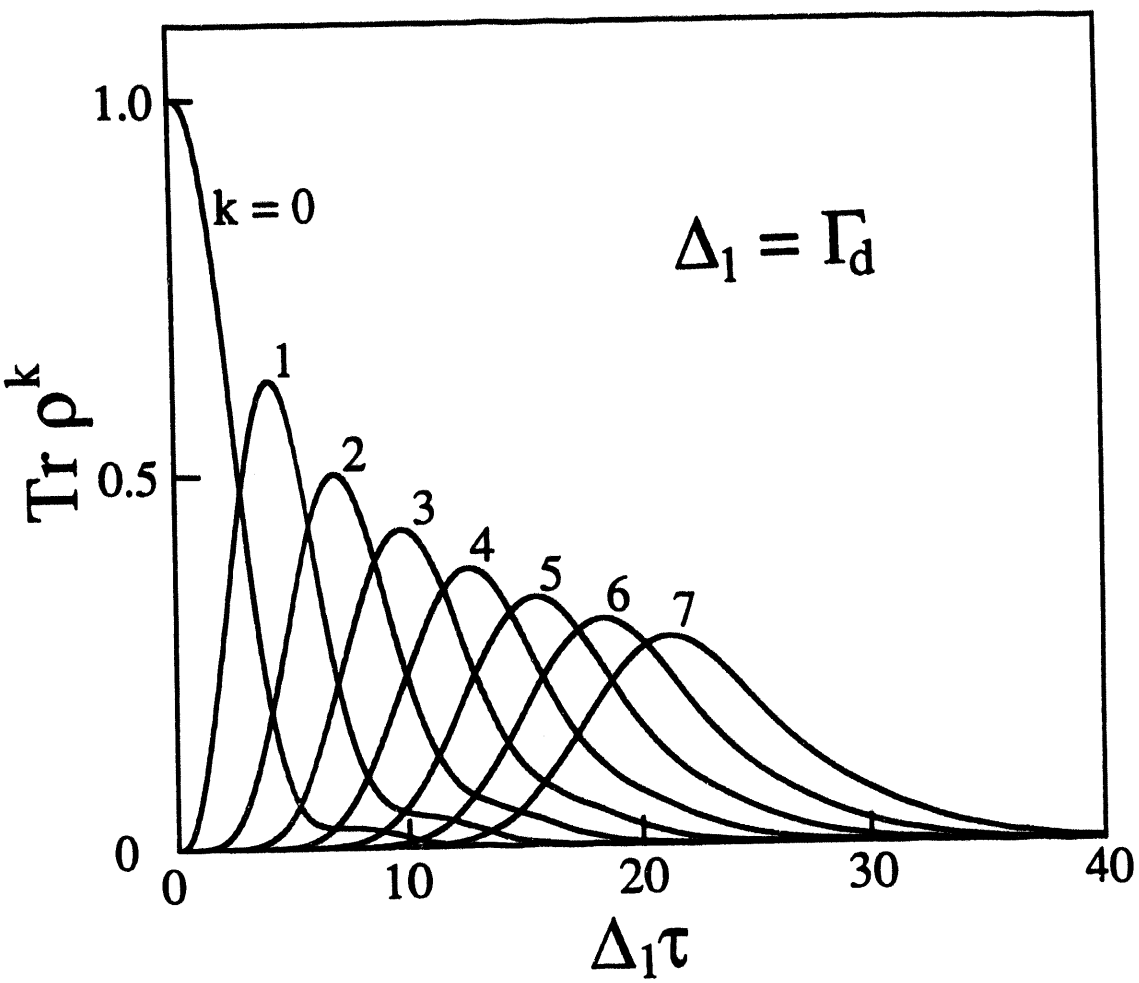

FIGURE 2-3. Propagation of probability density through the first eight subsystems (k = 0 through k = 7). Shown is the time dependence of the traces of the density matrix in each subsystem for $\Delta_1=\Gamma_d$. The time dependence scales inversely with Δ_1 and is thus plotted as a function of $\Delta_1\tau$.

as the initial deviation from this steady motion is simply an artifact of the somewhat artificial initial conditions. The time derivative of $<\phi>/2\pi$ is

$$\begin{aligned}\frac{d}{d\tau}\frac{<\phi>}{2\pi} &= \sum_{k=1}^{\infty} k\,\mathrm{Tr}\frac{d}{d\tau}\rho^k + \sum_{k=0}^{\infty}\frac{d}{d\tau}\rho_{22}^k \\ &= \sum_{k=1}^{\infty} k\xi\cdot(A\tilde{\rho}^k + B\tilde{\rho}^{k-1}) + \sum_{k=0}^{\infty}\frac{d}{d\tau}\rho_{22}^k \\ &= \sum_{k=0}^{\infty}\Gamma_d\rho_{22}^k + \sum_{k=0}^{\infty}\frac{d}{d\tau}\rho_{22}^k \quad ,\end{aligned} \tag{2-35}$$

where the inner product $\xi\cdot\tilde{\rho}$ of $\xi = (1, 0, 0, 1)$ and a vector $\tilde{\rho}$ produces the trace of the associated matrix ρ.

Rather than solve the entire system of Eqs. (2-30) through (2-33) to evaluate this expression, I find that the quantity given in Eq. (2-35) can be extracted from the following simple construction: Defining

$$\tilde{\rho}^{tot} \equiv \sum_{k=0}^{\infty}\tilde{\rho}^k \quad , \tag{2-36}$$

which is the sum of all the subsystem density matrices (in vector form), and summing the system of Eqs. (2-30) through (2-33) over all k, I can write

$$\begin{aligned}&\frac{d}{d\tau}\tilde{\rho}^{tot} = \tilde{A}\tilde{\rho}^{tot}, \\ &\tilde{A} = A + B, \\ &\tilde{\rho}^{tot}(0) = (1,0,0,0)^T .\end{aligned} \tag{2-37}$$

This system, which I refer to as the reduced system, is shown schematically in Fig. 2-4. Physically it corresponds to taking the probability density as it leaves a subsystem and

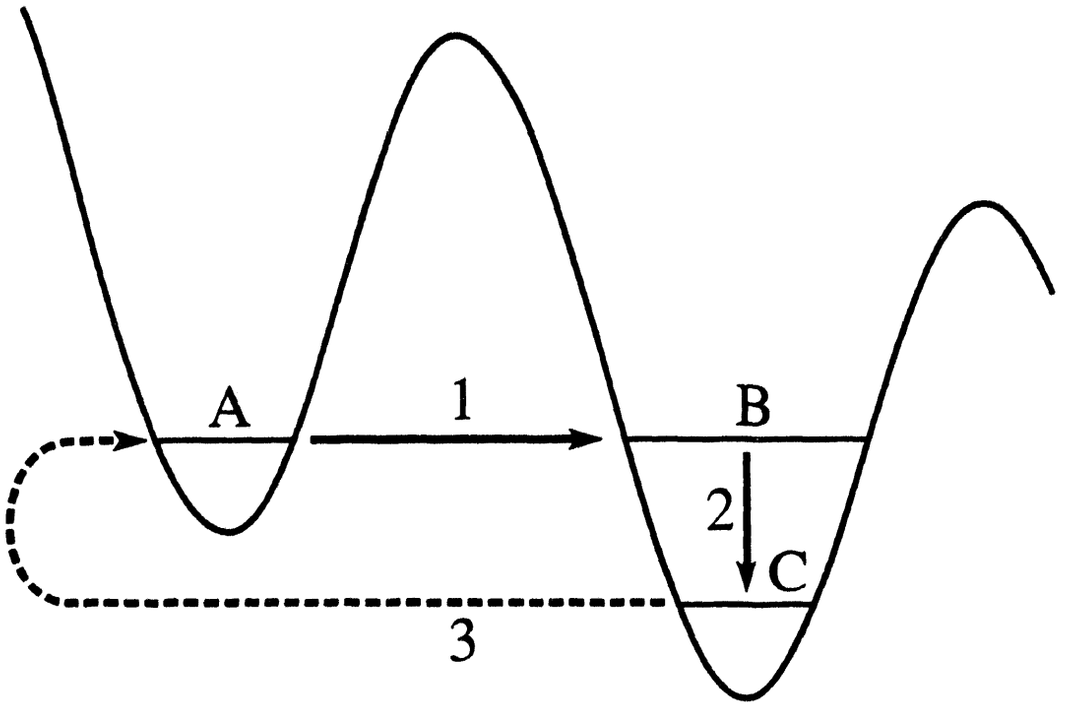

FIGURE 2-4. Schematic representation of the reduced system for $\ell_{max} = 2$. The reduced system consists of states A and B, which are coupled by the coherent transition (1). Probability density leaves state B by decay (2) to state C of the full system. In the reduced system this density is incoherently reintroduced at state A, as shown by the dotted arrow (3).

returning it incoherently to the ground state of the same subsystem. It is in fact the linear superposition of the subsystems, which obey the same equation of motion with the exception of the source terms. Because $\xi \cdot \tilde{A} = 0$, the trace is conserved in the reduced system; the constraint that the particle remain within the set of ground states and first excited states corresponds to probability density remaining in the two states of the reduced system.

The reduced system has the steady state solution (in matrix form)

$$\lim_{\tau\to\infty} \rho^{tot} = \frac{1}{\Gamma_d^2 + 2\Delta_1^2 + 4\sigma^2} \begin{bmatrix} \Gamma_d^2 + \Delta_1^2 + 4\sigma^2 & \Delta_1(i + 2\sigma) \\ \Delta_1(-i + 2\sigma) & \Delta_1^2 \end{bmatrix} \tag{2-38}$$

giving

$$\gamma = \frac{\Gamma_d \Delta_1^2}{\Gamma_d^2 + 2\Delta_1^2 + 4\sigma^2} \ . \tag{2-39}$$

This result for the overall rate γ is plotted at resonance ($\sigma = 0$) as a function of Γ_d in Fig. 2-5. This expression can be explained intuitively for Γ_d/Δ_1 much less than or much greater than unity. When $\Gamma_d/\Delta_1 << 1$, the limiting process is the decay, and the subsystem will undergo many oscillations between its two states before decaying, spending half its time in the excited state. As the decay rate of this excited state is Γ_d, we obtain $\gamma = \Gamma_d/2$ in this limit. In the opposite limit, $\Gamma_d/\Delta_1 >> 1$, the resonant tunneling is the limiting process. Decay occurs shortly after the particle tunnels into the excited state, which is lifetime broadened into a continuous density of states $D(\sigma) = (\Gamma_d/2\pi)/(\sigma^2 + \Gamma_d^2/4)$, and the possibility of tunneling back to the ground state is negligible. Fermi's Golden Rule then applies, giving $\gamma = 2\pi\, |\Delta_1/2|^2\, D(0) = \Delta_1^2/\Gamma_d$.

The voltage developed across the junction at or near resonance due to this steady motion is then simply

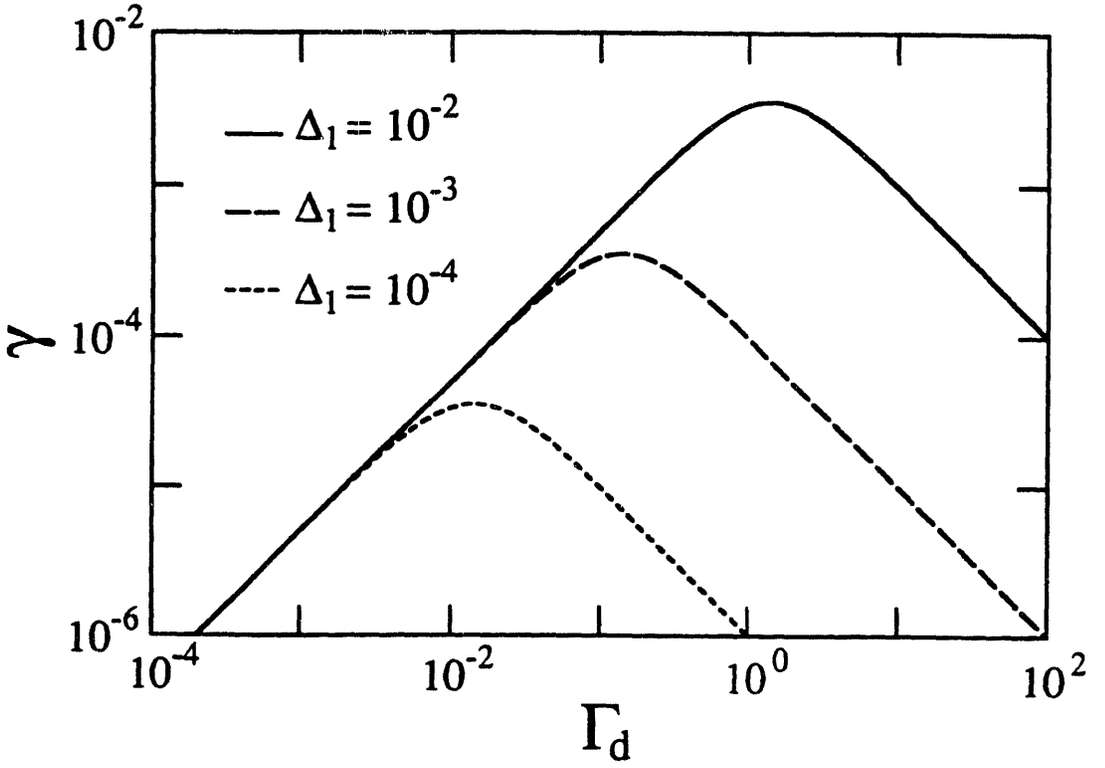

FIGURE 2-5. Rate of motion γ down the washboard at resonance as a function of the decay rate Γ_d for typical inter-well couplings of $\Delta_1 = 10^{-2}$, 10^{-3}, and 10^{-4}.

$$V = \Phi_0 \omega_p \gamma / 2 \tag{2-40}$$

where $\Phi_0 = h/2e = 2.07 \times 10^{-15}$ Wb is the flux quantum. Using the dependence of σ on bias current I_{Bias} given in Eq. (2-25) and treating Δ_1 as a constant, I find that V is Lorentzian-shaped as a function of I_{Bias}, with half-width at half-maximum

$$\Delta I_{Peak} = \frac{e}{\pi} \omega_p \frac{\left(\Gamma_d^2 + 2\Delta_1^2\right)^{1/2}}{4} \quad . \tag{2-41}$$

Note that ΔI_{Peak} scales with the lifetime broadening width $\Gamma_d/2$ of the excited state when $\Gamma_d >> \Delta_1$, and with the coupling $\Delta_1/2$ when $\Gamma_d << \Delta_1$. I can evaluate the voltage given in Eq. (2-41) at resonance in terms of the junction parameters ω_p, ν, and R. Using the expression $\Gamma_d = 2/(RC\omega_p)$ and writing the capacitance as $C = \pi\nu/\omega_p R_Q$, where $R_Q = \pi\hbar/2e^2 = 6.45\ k\Omega$ is the quantum of resistance, I obtain $\Gamma_d = 2R_Q/\pi\nu R$. Taking this result along with my estimate for Δ_1 and $\omega_p/2\pi = 10^{10}$ Hz, I obtain the peak voltage as a function of ν for several ratios of R/R_Q, plotted in Fig. 2-6.

Lifetime of the Peak and Switching Distributions

Next I consider the consequences of additional states in the subsystem and the escape to the free running states. The mixing of the states within a subsystem implies that there is a nonzero probability of finding the particle in one of the states other than Ψ_{k1} and Ψ_{k2}, and in particular, in one of the states $\Psi_{k\ell max}$ which are separated from the set of free running states by a single barrier, allowing escape of the particle to these states via tunneling. These additional states and the tunneling process can be included by a simple extension of the method used above. The additional states are included in the basis for the subsystem. The tunneling, which is an incoherent process characterized by a

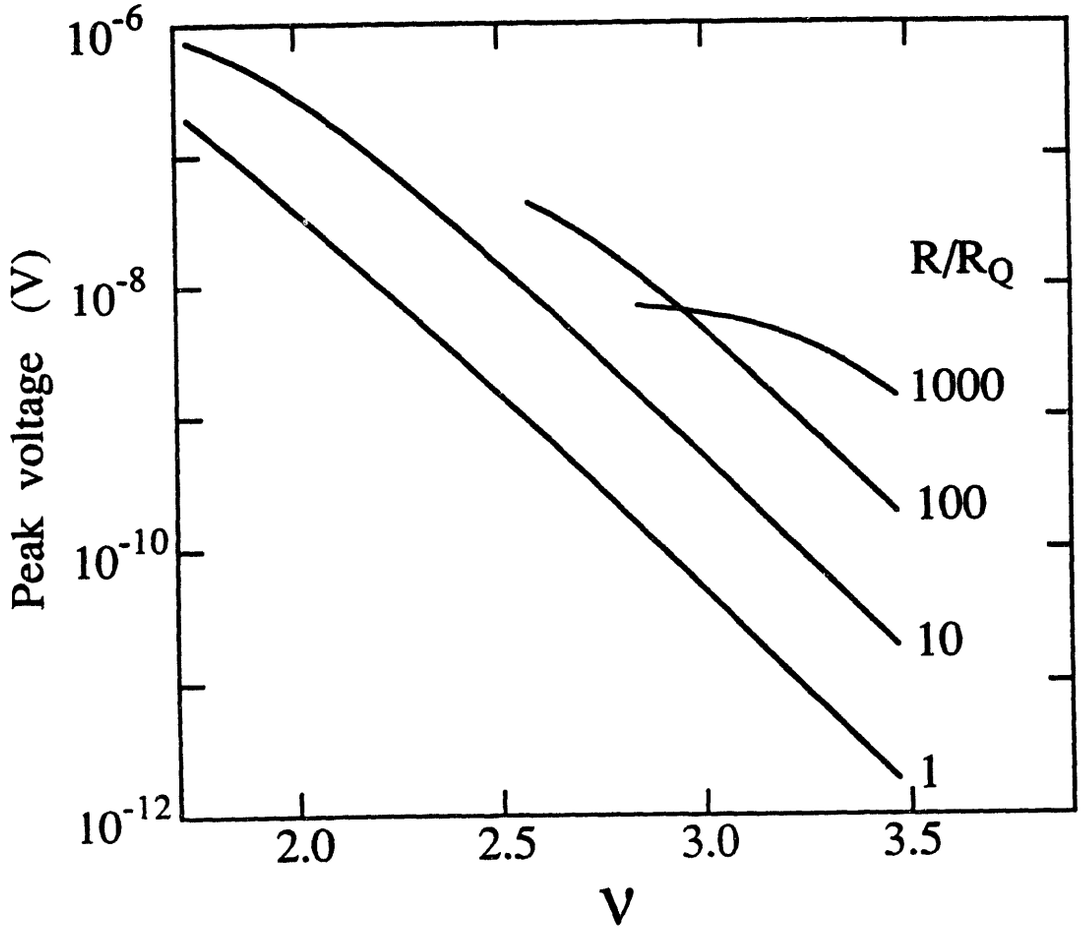

FIGURE 2-6. Maximum voltage developed across the junction by resonant tunneling on the first resonance, plotted as a function of ν for several values of R/R_Q and a plasma frequency $\omega_p/2\pi = 10^{10}$ Hz. The curves for $R/R_Q = 100$ and 1000 are cut off where $\gamma\tau_{life} = 1$ (see text).

constant rate, is added as an imaginary energy term in the energy of the states $\Psi_{k\ell max}$, analogous to the treatment of decay.

This treatment, unfortunately, cannot be continuously applied over the entire range of ν, as it is based on the assumption of the existence of an integral number of distinct bound states in a subsystem, and this is not always a very sharply defined quantity. Using Eqs. (2-10), (2-13), and (2-20) for the energy levels, I find that near resonance there are two bound states in a subsystem for ν roughly between 1.7 and 2.6, and three states for ν between 2.6 and 3.5. More realistically, however, for $\nu \approx 2.6$ the "third state" is actually a continuous density of states which are hybrids combining a localized state and the free running states. In this region of ν the present treatment is not applicable. However, I may apply the method with confidence for the intermediate values of ν in the two ranges $1.7 < \nu < 2.6$ and $2.6 < \nu < 3.5$ and extrapolate these results into the intermediate region $\nu \approx 2.6$.

In each of these two ranges of ν I estimate the tunneling rate from the state $\Psi_{k\ell max}$ into the continuum of free states using the WKB method. The expression for this rate, expressed in units of $\omega_p/2$ and denoted by $\Gamma^{WKB}_{\ell_{max}}$, is

$$\Gamma^{WKB}_{\ell_{max}} = \frac{1}{\pi} G(\ell_{max}) \exp(-2I_{\ell_{max}}) \ , \tag{2-42}$$

where I and G are given by Eqs. (2-23) and (2-24), respectively.

The terms representing coherence in the equations of motion (2-28) and (2-29) remain unchanged in form. However, the matrices H_0 and Γ appearing in these terms must be modified to include the additional states and tunneling rates. For the case of two states per subsystem ($1.7 < \nu < 2.6$), H_0 is as before, while Γ becomes

$$\Gamma = \begin{bmatrix} 0 & 0 \\ 0 & \Gamma_d + \Gamma_2^{WKB} \end{bmatrix} . \tag{2-43}$$

In the case of three states per subsystem ($2.6 < \nu < 3.5$), I include in the subsystem basis the state Ψ_{k3}, which has energy ε relative to the average of the energies of states Ψ_{k1} and Ψ_{k2},. This energy is given by

$$\varepsilon = 3 - 3\pi s\nu - \frac{3s^2}{4} - \frac{5}{4\nu} - \frac{15}{32\nu^2} \tag{2-44}$$

to second order in $1/\nu$. Defining $\Delta_2/2 \equiv H_{0,1,1,2}$, I obtain

$$H_0 = \begin{bmatrix} \frac{\sigma}{2} & \frac{\Delta_1}{2} & 0 \\ \frac{\Delta_1}{2} & \frac{-\sigma}{2} & \frac{\Delta_2}{2} \\ 0 & \frac{\Delta_2}{2} & \varepsilon \end{bmatrix}, \tag{2-45}$$

and

$$\Gamma = \begin{bmatrix} 0 & 0 & 0 \\ 0 & \Gamma_d & 0 \\ 0 & 0 & \Gamma_d + \Gamma_3^{WKB} \end{bmatrix}. \tag{2-46}$$

Note that $|\sigma| + |\varepsilon| >> \Delta_1, \Delta_2$, which implies that at most two of the states are strongly mixed at a given bias current. This tends to suppress the escape rate by reducing the probability of several resonant tunneling events occurring in succession. Also note that I have taken the decay from Ψ_{k3} to $\Psi_{k+1,2}$ to have twice the rate as that from Ψ_{k2} to $\Psi_{k+1,1}$. This is exactly true in the case of the harmonic oscillator [32], as I will show in Chapter 3, and I expect it to be a reasonable approximation in the present case.

The source terms in Eq. (2-29) must be modified to include only the contributions of the decay process. This is most easily done after the transformation from matrices to column vectors has been performed. For example, in the case of two states per well, the source matrix B given in Eq. (2-33) remains unchanged, whereas in matrix A, given by Eq. (2-32), Γ_d is replaced by $\Gamma_d + \Gamma_2^{WKB}$.

Again I can transform the coupled equations of motion for the entire set of subsystems to the equation of motion

$$\frac{d}{d\tau}\tilde{\rho}^{tot} = \tilde{A}\tilde{\rho}^{tot} \tag{2-47}$$

for a single reduced system, which is identical in form to Eq. (2-36) except that now $\tilde{A}$ is either a 4×4 or 9×9 matrix.

The reduced system (2-47) can be solved numerically. As asserted previously, I find that the motion of the two state system is only weakly perturbed by the inclusion of escape, except when ν is small and the resistance R is large. For short times the elements of the density matrix reach approximately the same steady state values as they had before the inclusion of escape. For longer times, however, I find that each of the elements undergoes a slow exponential decay, and the trace is no longer conserved. This decay of the trace corresponds to the escape of probability density via tunneling into the free running states.

The full solution of Eq. (2-47) is a linear combination of solutions, each containing a factor $\exp(\lambda\tau)$ in the time dependence, where λ is one of the eigenvalues of $\tilde{A}$. When escape is not included ρ^{tot} has a steady state solution, which corresponds to the eigenvalue 0. When escape is included, this eigenvalue is shifted slightly in the negative direction along the real axis, and is associated with the slow exponential decay of the trace. It is the negative value of this eigenvalue that I take as the overall escape rate, and the reciprocal of this rate τ_{life} gives the (dimensionless) lifetime of the resonant peak structure. Note that one obtains meaningful results from this method only when the product $\lambda\tau_{life}$ is greater than unity. This quantity is an estimate of the number of inter-well transitions the particle makes before escaping, and when this number is less than one the coupling to the continuum is so strong that the bound state approximation becomes invalid and an alternative approach must be used.

I have calculated both the lifetime $t_{life} = 2\tau_{life}/\omega_p$ at the resonance $I_{Bias} = I_1^{res}$ and the escape rate t_{life}^{-1} as a function of bias current near the resonance, in each case using the same set of parameters I used in calculating the magnitude of the voltage peak. The lifetimes are shown in Fig. 2-7, and the escape rates are shown in Figs. 2-8 and 2-9. In both the lifetime and the escape rates I find small discontinuities at $\nu = 2.6$ which arise between the two and three state treatments. This is not alarming considering the discontinuity inherent in the two methods. The match is in fact remarkably good when one considers that small changes in Δ_1, Δ_2, Γ_2^{WKB}, and Γ_3^{WKB} can greatly increase or decrease the discontinuities, and perhaps better estimates of these quantities would further smooth the transition.

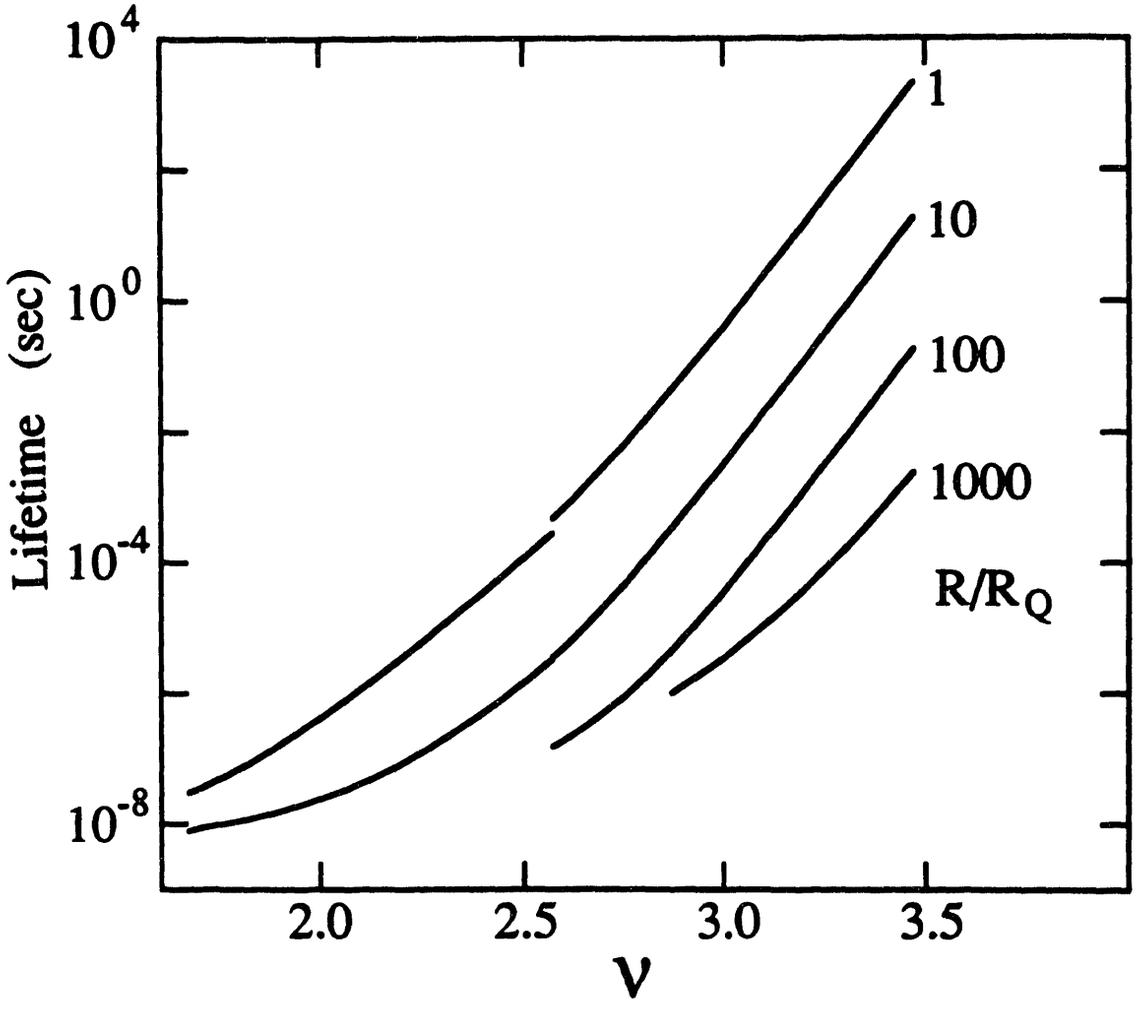

FIGURE 2-7. Lifetime t_{life} of the first voltage peak on resonance $I_{Bias} = I_1^{res}$ before escape occurs, computed with the same set of junction parameters as in Fig. 2-6.

2.4 Prospects for Experimental Observation

The theory presented above identifies two principal candidates for effects which would provide experimental evidence of resonant tunneling, namely voltage peaks on the supercurrent branch of the current-voltage characteristic and the distinctive distribution of rates at which the junction switches to the normal state. In this section I wish to examine the prospects of observing these primary signatures of resonant tunneling.

I focus my attention first on the voltage peaks. Figure 2-6 shows that the magnitude of the voltage is on the order of 1 μV for $\nu = 1.7$ and decreases exponentially with increasing ν, becoming rather small (10^{-12} to 10^{-9} V) for $\nu = 3.5$. On the other hand, the lifetime of the voltage peak ranges from 10^{-8} to 10^{4} sec, as shown in Fig. 2-7. Evidently, in choosing values of ν and R one must balance between measuring an extremely small signal of lengthy duration and a larger signal of extremely short duration. In order to analyze this apparent trade-off, I construct a figure of merit which is the estimated voltage signal at resonance divided by the square root of a measurement bandwidth which I take to be the inverse of the estimated lifetime. Using this approach I obtain values between 10^{-12} and 10^{-10} V $Hz^{-1/2}$ for the entire range $1.7 \leq \nu \leq 3.5$ and $1 \leq R/R_Q \leq 1000$. Since the quietest semiconductor amplifiers have a typical voltage noise of 10^{-9} V $Hz^{-1/2}$, this result implies that the use of such amplifiers for the direct observation of the voltage peaks is most certainly ruled out. However, a more sophisticated method exploiting signal averaging techniques may reveal this structure.

Thus, it appears that the most readily observable effect arising from resonant tunneling is the distribution of rates at which the junction switches to the normal state, shown in Figs. 2-8 and 2-9. The most unusual feature of these distributions is that they are non-monotonic in the bias current, in contrast to those where switching is caused by thermal activation or macroscopic quantum tunneling. Peaks occur in the escape rate for bias currents at the resonance values. In the case of two states per well (Fig. 2-8) a single

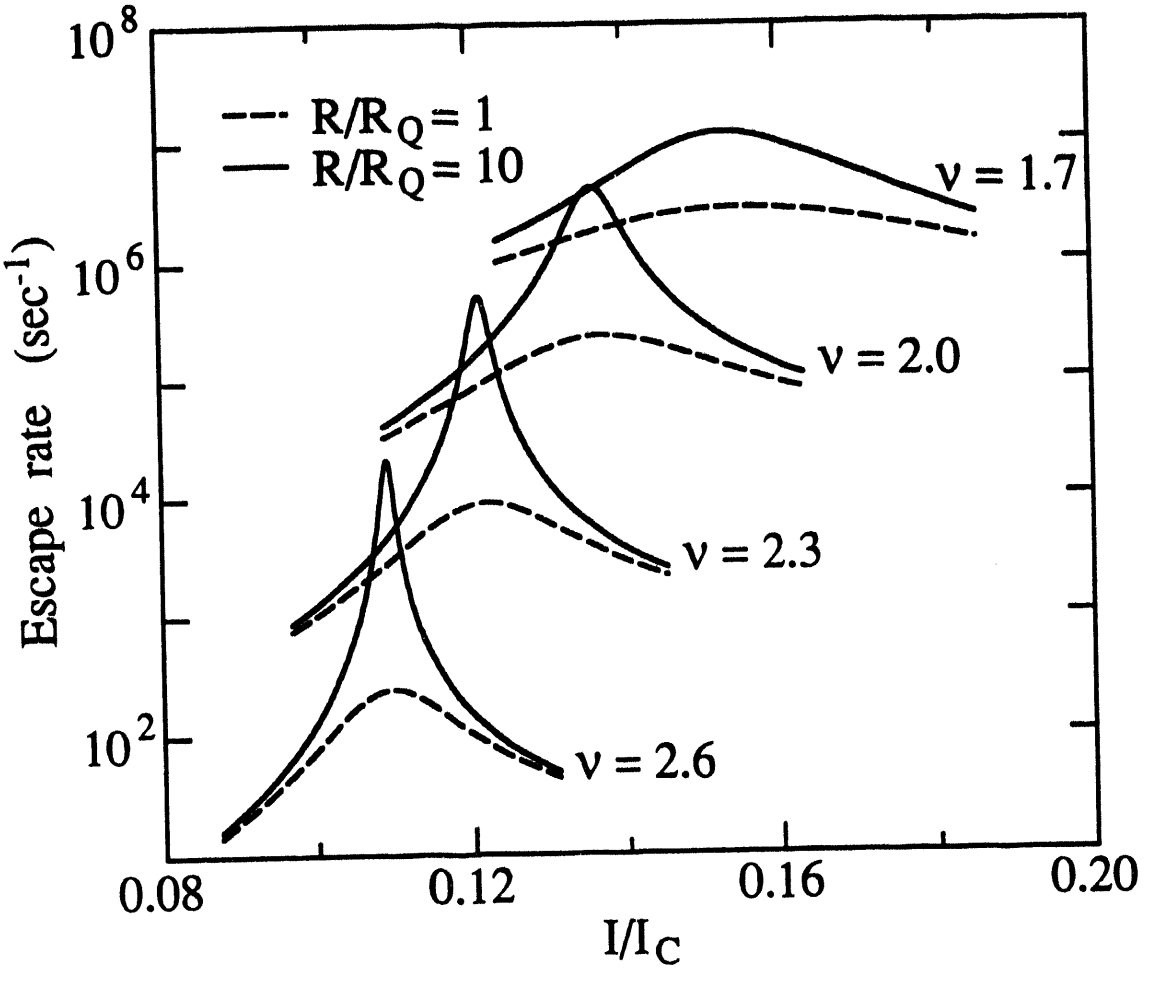

FIGURE 2-8. Distribution of rates at which the junction switches to the normal state as a function of bias current for the case of two states per well, plotted for ν = 1.7, 2.0, 2.3, and 2.6, and R/R_Q = 1 and 10.

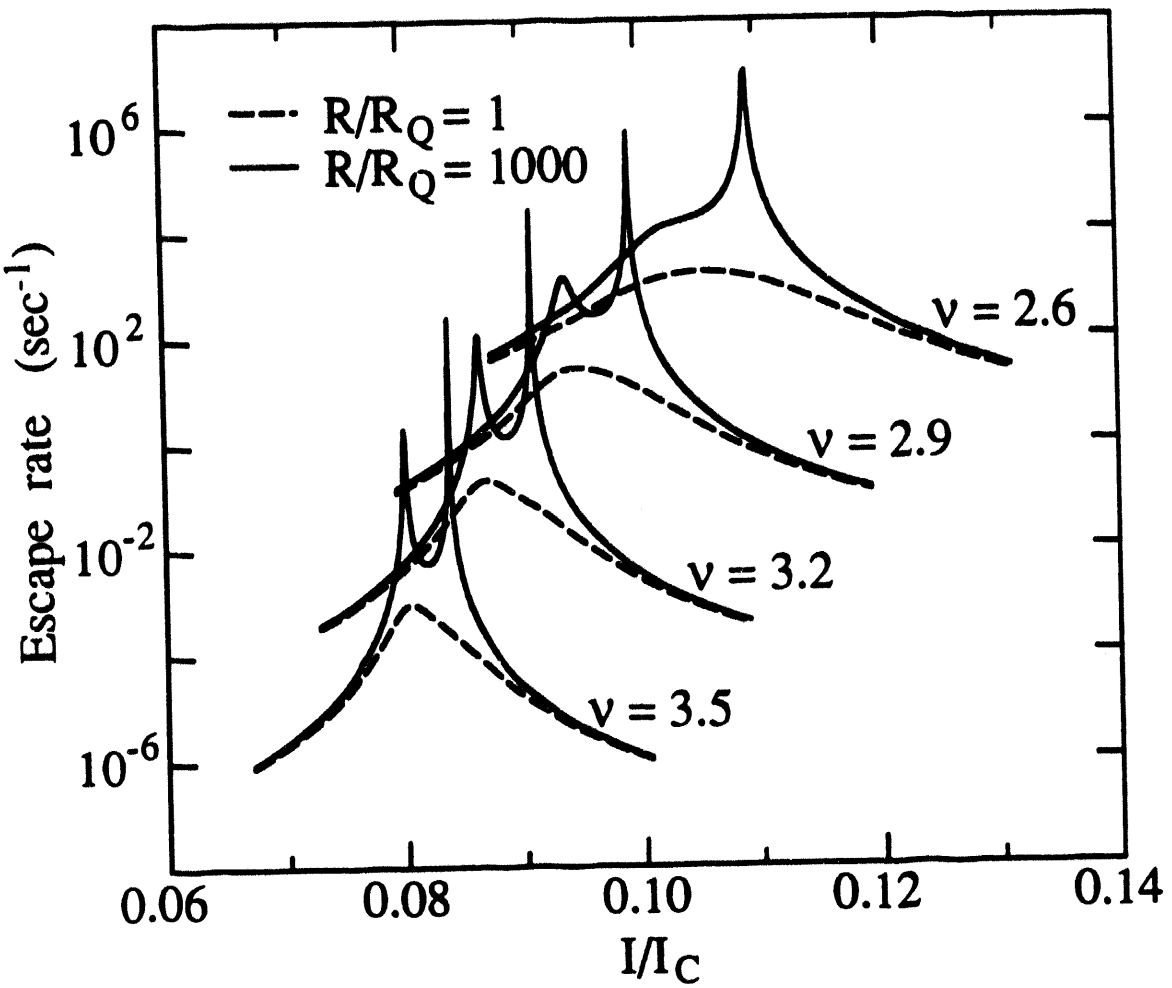

FIGURE 2-9. Distribution of rates at which the junction switches to the normal state as a function of bias current for the case of three states per well, plotted for ν = 2.6, 2.9, 3.2, and 3.5, and R/R_Q = 1 and 1000.

peak appears, corresponding to resonance between states Ψ_{k1} and Ψ_{k2}. In the case of three states per well (Fig. 2-9), additional smaller peaks appear for slightly smaller bias currents, corresponding to resonances between states Ψ_{k1} and Ψ_{k3} and states Ψ_{k2} and Ψ_{k3}. The former is almost as pronounced as the primary resonance peak, while the latter is very small and cannot be seen on the scale of Fig. 2-9. With the exception of this small peak, which is largest for $R/R_Q \approx 100$, I find in general these peaks are most pronounced for the cases of low damping (high resistance) because the particle spends more time in the excited states $\Psi_{k\ell_{max}}$ and therefore has a higher probability of escaping through the final barrier to the free states. The observation of these peaks in the distribution of switching rates would be a direct confirmation of the existence of resonant tunneling in Josephson junction dynamics.

Finally, I note that my results have implications for the Bloch oscillations predicted to occur in the $\nu << 1$ limit. It is apparent that in the region where ν is small and the resistance is large the escape rate is rather high and the particle makes no more than a few transitions to lower subsystems before escaping. Thus, as one reduces the value of ν, for bias currents corresponding to the resonance condition one should expect the Bloch oscillations to be suppressed because of escape to the voltage state.

CHAPTER 3

Beyond the Model Theory

Having presented the quantum theory for resonant tunneling in the previous chapter, which addresses several specific aspects of behavior predicted for a junction in this parameter range, I must now examine some other aspects of small junction behavior which have been theoretically studied and experimentally observed.

The theory of Chapter 2 describes only the motion within the set of potential wells, and the transition out of the wells. It does not address motion of the system which occurs just after a transition out of the wells, specifically whether the free running state will be obtained and sustained. The model examines the relatively simple quantum behavior of a noise-free system at zero temperature, with ohmic damping included only phenomenologically. While providing much useful information about resonant tunneling dynamics, the model is far from a complete picture with regards to representing an actual junction operating in a realistic measurement environment.

The experimental results of Kautz and Martinis (KM) [26] show there is much that one can learn from a completely classical description of a Josephson junction. One can expect that many of the effects which govern the observed classical behavior will carry over into the quantum limit where resonant tunneling is likely to be observed, and

thus a classical description should be a good starting point for identifying behavior that will be influence the design of an experiment to observe resonant tunneling.

The treatment of dissipation in my model was phenomenological. A more rigorous treatment requires the inclusion of the dissipation directly as a part of the quantum system. The proper treatment of dissipation is important, because dissipation not only supplies a decay mechanism, but also breaks coherent superpositions of eigenstates and provides an additional means of coupling between these macroscopic states.

First I will present some classical results obtained from the RSJ model in the $T > 0$ limit. Then I will give a brief description of the KM model and their results, focusing on the aspects which have bearing on a resonant tunneling experiment. In the next section I will present a brief summary of the quantum treatment of dissipation, including a derivation of the phenomenological decay rate I used in Chapter 2, and discuss the correspondence between the quantum limit and the classical limit.

3.1 Classical Models of Small Capacitance Josephson Junctions

Thermal Effects in the RSJ Model

The RSJ model is well studied, and there exist several good references for it [14, 33]. In particular, I found the article by KM [26] gives a very enlightening description of noise-affected dynamics in the RSJ model, primarily because it provides an appropriate background for the discussion of how these dynamics are modified by the addition of a shunt element which is frequency-dependent.

The equation of motion given in Eq. (2-4) for the phase variable ϕ governs classical, fluctuation free (zero temperature) behavior. In this case, the dynamics of the system are straightforward to work out. When the particle is trapped in a well, it remains there until the bias current I_{Bias} is increased to a value greater than the critical current I_c. Only then does it switch to the free-running state, where it remains until the current is reduced to the zero temperature retrapping current I_{r0}. Stewart [3] found that, for low damping

$$I_{r0} = I_c \frac{4}{\pi Q} \quad , \tag{3-1}$$

where the reader is reminded that $Q = RC\omega_p$ is the classical quality factor, which is equal to $\beta_c^{1/2}$ in Stewart's notation. Here "low damping" means $Q >> 1$, and when $Q > 3$, the expression given by Eq. (3-1) is accurate to better than a few percent. It is useful to adopt the terminology of KM and define the state where the particle is trapped in a well as the 0-state, and the free running state as the 1-state.

To include the action of fluctuations present in the system when it is in thermal equilibrium at temperature T, a current noise source I_N is added to the bias current, giving the equation of motion

$$\left(\frac{\hbar}{2e}\right)C\ddot{\phi}+\left(\frac{\hbar}{2e}\right)\frac{1}{R}\dot{\phi}+I_c\sin\phi=I_{Bias}+I_N \quad . \tag{3-2}$$

The noise source I_N, which has autocorrelation

$$\langle I_N(t')I_N(t)\rangle=\frac{2k_BT}{R}\delta(t'-t) \quad , \tag{3-3}$$

represents the Nyquist noise of the shunt resistor.

The noise source affects the transitions between the 0 and 1-states by supplying thermal energy, thereby allowing escape events from the 0-state to occur at bias currents $I_{Bias} < I_c$ and retrapping events to occur at bias currents $I_{Bias} > I_{r0}$. These thermally activated escape and retrap processes have been studied theoretically. The escape process has been studied by several authors [34-37] using the theory of Kramers [38]. The lifetime of the 0-state is given by

$$t_+=\frac{2\pi}{\omega_p}\left[\left(\sqrt{1-s^2}+\frac{1}{4Q^2}\right)^{1/2}-\frac{1}{2Q}\right]^{-1}\exp\left(\frac{\Delta u}{\Gamma}\right) \quad , \quad \Gamma<\frac{2\pi\Delta u}{Q(1-s^2)^{1/4}} \quad , \tag{3-4}$$

$$t_+=RC\frac{\Gamma}{\Delta u}\exp\left(\frac{\Delta u}{\Gamma}\right) \quad , \qquad \Gamma>\frac{2\pi\Delta u}{Q(1-s^2)^{1/4}} \quad , \tag{3-5}$$

Here $\Gamma = 2ek_BT/\hbar I_c$ is the reduced temperature, the reduced energy barrier Δu is

$$\Delta u=2(1-s^2)^{1/2}+2s\cos^{-1}s \quad , \tag{3-6}$$

where $s = I_{Bias}/I_c$ is the reduced bias current. The subscript of t_+ indicates a transition in the positive ϕ direction for $I_{Bias} > 0$. A similar expression for transitions in the negative direction exists, but I will neglect these transitions for they are infrequent compared to the

positive transitions at temperatures and bias currents of interest. Also, in the present work I will only encounter parameters for which the expression given by Eq. (3-4) is appropriate, so henceforth I will only use this expression. The rate of escape Γ_+ from the 0-state is given by the inverse of Eq. (3-4):

$$\Gamma_+ = \frac{\omega_p}{2\pi}\left[\left(\sqrt{1-s^2}+\frac{1}{4Q^2}\right)^{1/2}-\frac{1}{2Q}\right]\exp\left(\frac{-\Delta u}{\Gamma}\right) . \qquad (3\text{-}7)$$

Note that the form of this equation for $Q >> 1$ is an attempt frequency $(1-s^2)^{1/4}\omega_p/2\pi$, which is equal to the frequency of small oscillations in the well, times an Arrhenius factor.

The analogous analytic results for the retrapping problem were only more recently obtained, primarily because the 1-state represents a dynamic non-equilibrium state, in contrast to the 0-state. Ben-Jacob has found that the lifetime of the 1-state is given approximately by

$$t_1 = RC\sqrt{\frac{\pi\Gamma}{\Delta w}}\exp\left(\frac{\Delta w}{\Gamma}\right) , \qquad (3\text{-}8)$$

where

$$\Delta w = \frac{1}{2}Q^2(s-s_{r0})^2 . \qquad (3\text{-}9)$$

Here $s_{r0} = I_{r0}/I_c$. Note that Δw has the form of an activation energy and is approximately equal to the kinetic energy of the particle, which is the energy which must be dissipated in order to trap the particle in a well. The inverse of Eq. (3-8) gives the rate of thermally activated retrapping Γ_1:

$$\Gamma_1 = \frac{1}{RC}\sqrt{\frac{\Delta w}{\pi\Gamma}}\exp\left(\frac{-\Delta w}{\Gamma}\right) . \qquad (3\text{-}10)$$

Note that as $T \rightarrow 0$, the current at which retrapping is likely to take place approaches the zero temperature value given by Eq. (3-1).

The barrier Δu depends only on the bias current, whereas the barrier Δw also depends on the damping of the system through the parameter Q. These functions are plotted in Fig. (3-1) for several values of Q. The barriers Δu and Δw appear as the activation energy in Arrhenius factors in the expressions for Γ_+ and Γ_1. Thus, the relative values of Δu and Δw indicate whether escape or retrapping will dominate at a particular value of s in the thermal limit. In addition, the available thermal energy may be schematically drawn as a horizontal line on this plot, such that when the value of one of these barriers drops below this line, the associated transition becomes active. In particular, one can understand the current-voltage trace which results by slowly increasing and then decreasing the current bias. While a detailed statistical study of the problem of slowly changing the current bias until a transition occurs is undertaken in Chapter 4, for now it is sufficient to note that as the temperature is raised from zero temperature, the average escape current will be reduced from I_c, while the average retrap current will be increased from I_{r0}.

One final note completes my discussion of the RSJ model with a simple ohmic shunt. One might wonder whether a forward transition out of a well is quickly followed by a retrapment on occasion, or if an escape always results in transition to the 1-state. Silvestrini and Cristiano [39] have found that for low temperatures and $Q >> 1$, escape from a well almost always leads to a complete transition to the 1-state when the current bias is well above the value I_{r0}. When I_{Bias} is just greater than I_{r0}, this is also the case because whenever there is sufficient thermal energy for a thermal transition out of a well in the positive direction, there is also enough thermal energy to activate a retrapping process, and this retrapping rate is always much greater than the escape rate for bias currents near I_{r0}.

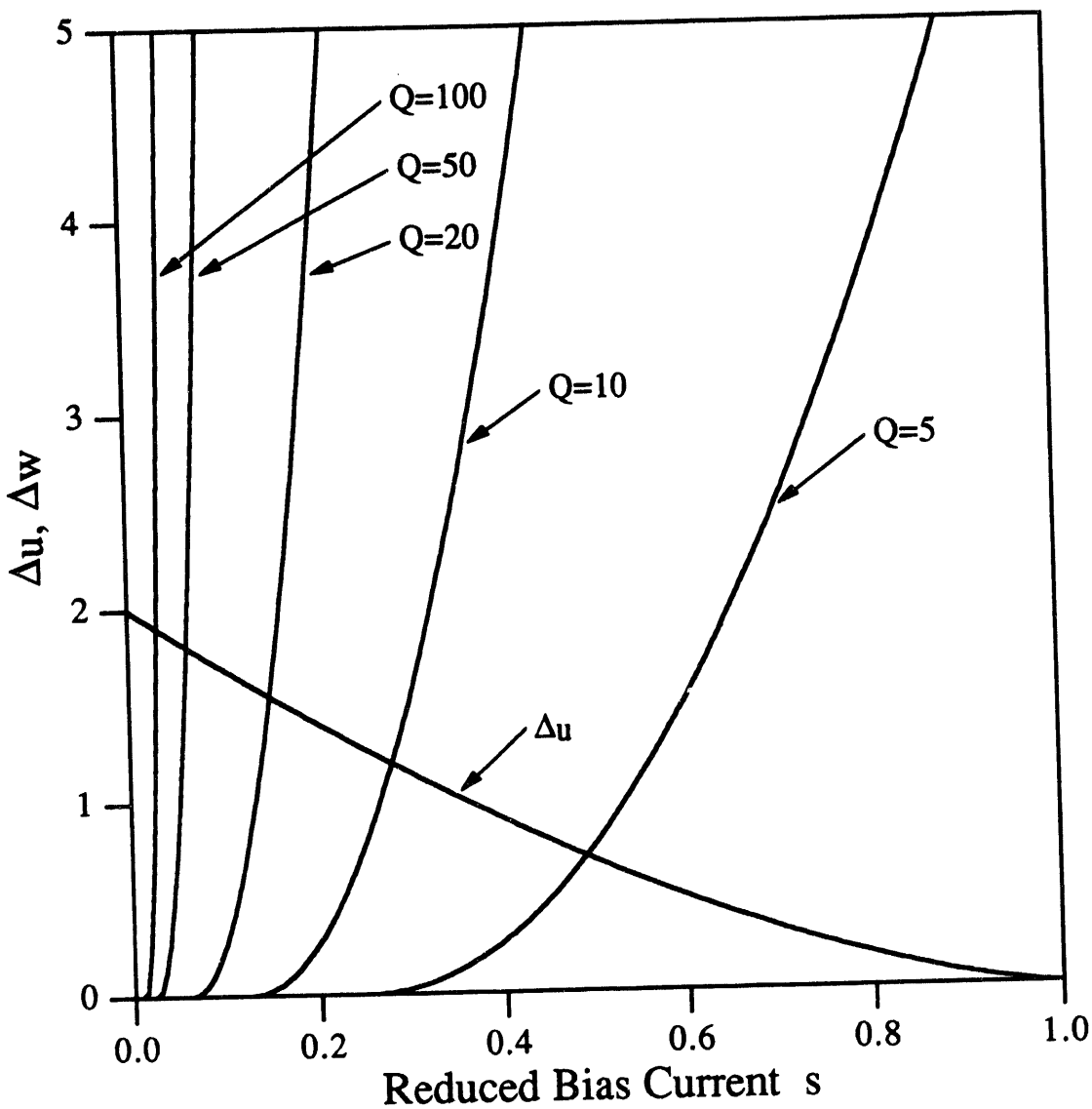

FIGURE 3-1. Reduced activation energies Δu and Δw plotted as a function of reduced bias current s. The activation energy Δu for escape from the 0-state is indicated with an arrow. The activation energy Δw for retrapping is shown for five values of Q as indicated in the figure.

Augmenting the RSJ Model with a Frequency-Dependent Shunt Impedance

Experimental tests performed by KM on small capacitance junctions in the parameter regime where resonant tunneling is likely to occur clearly demonstrate that a complete model for the circuit which shunts the ideal Josephson element, including circuit elements external to the device, must be included in a model for the junction. The simple ohmic resistor of the standard RSJ model was found inadequate to explain quantitatively or even qualitatively their measured current-voltage characteristics. For a detailed discussion, I refer the reader to the work of KM directly. Although their experiments were performed on junctions operating at temperatures too great to observe resonant tunneling, their findings have implications for the present subject matter. I will summarize their results which distinguish the observed behavior from that predicted by the RSJ model and which are relevant to the resonant tunneling problem.

The extension of the RSJ model made by KM was to replace the simple ohmic resistor R by a more complex circuit, as shown in Fig. 3-2. As a first step this was simply an additional resistor and capacitor, as shown in Fig. 3-2 (b). While this modification qualitatively reproduced some features found in their experimental results, to represent the data with quantitative accuracy required an accurate model of the shunt impedance, shown as the lumped impedance $Z(\omega)$ in Fig. 3-2 (c). This impedance included the measured quasiparticle current of the junction, which is both temperature and voltage dependent, the on-chip thin film resistors which serve as current and voltage leads (which are a similar feature to my own experimental setup, as I will describe in Chapter 4), and the current bias circuitry.

The primary distinguishing feature of this model over the simple RSJ model is the inclusion of reduced damping at high frequencies, primarily near the plasma frequency. As a result, dynamic processes which occur at different characteristic frequencies are subject to different values of damping. Here I will give an example of this sort of effect which also has ramifications for a resonant tunneling experiment. KM define the

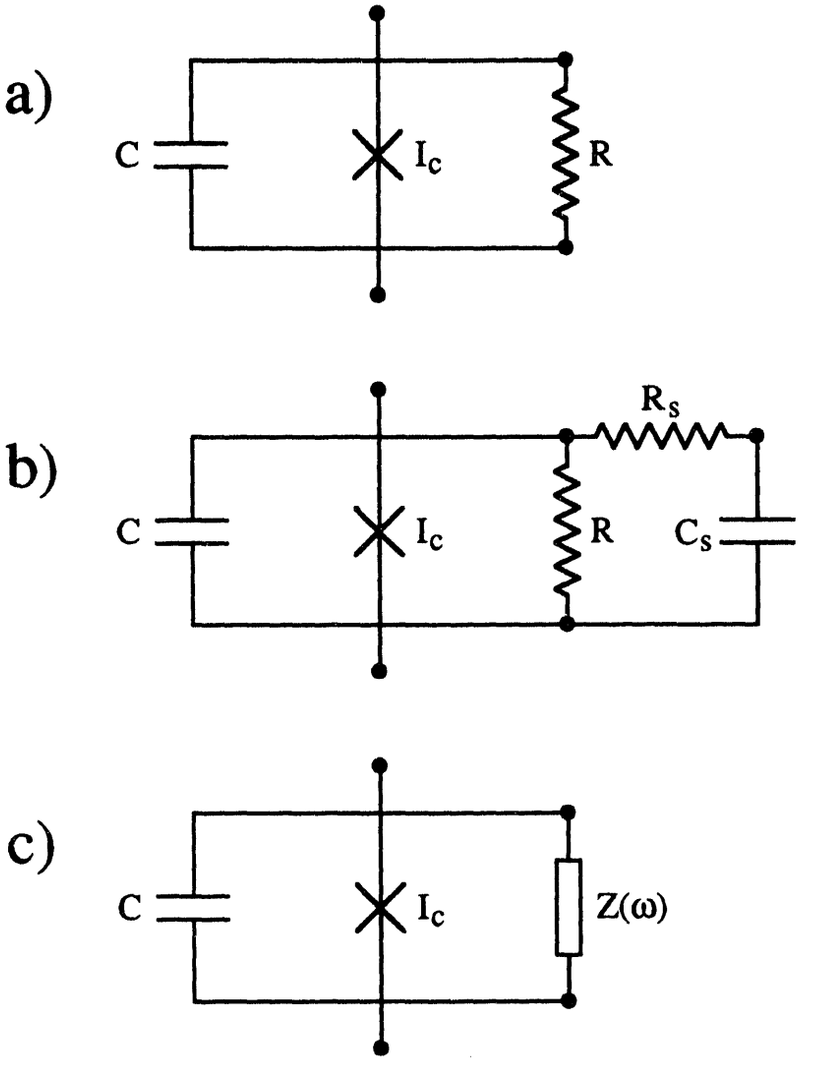

FIGURE 3-2. Shunted junction models studied by Kautz and Martinis [26]. (a) The standard resistively and capacitively shunted junction model (RSJ). (b) Junction with simple frequency dependent shunt composed of the resistor R in parallel with capacitor C_s and resistor R_s in series. (c) Junction with realistic model of the impedance $Z(\omega)$ which shunts the ideal junction elements.

minimum escape current I_m as the bias current such that, when a particle is initiated at a potential maximum with an infinitesimal positive velocity, it will arrive at the next potential maximum, also with an infinitesimal velocity. This is an important cutoff current for the escape process at low temperatures, for at bias currents less than I_m a particle moving near the top of a barrier is unlikely to get the boost of thermal energy necessary to clear the next barrier, while for bias currents greater than I_m, the particle will probably make it over the next barrier and continue to accelerate toward the 1-state. Meanwhile, the zero-temperature retrapping current I_{r0}, whose value for the RSJ model is given by Eq. (3-1), is defined as the minimum bias current which will support the 1-state. In the RSJ model the currents I_m and I_{r0} will be equal because the motion of the particle which defines I_m will be identical to the motion defining I_{r0}, where the particle just skirts the tops of the barriers of the washboard potential. Now consider a model where the damping is dependent on frequency such that the effective quality factor $Q(\omega)$ (which I will define more explicitly later) is equal to $Q(0)$ at low frequencies, and equal to $Q(\omega_p)$ at the plasma frequency. Here, the motion involved in escape is dominated by damping at the plasma frequency because the oscillations in a well which build in amplitude before an escape are essentially plasma oscillations. Thus, one expects the minimum escape current to be given by

$$I_m = I_c \frac{4}{\pi Q(\omega_p)} \quad . \tag{3-11}$$

By contrast, I_{r0} is defined as the limiting case of the 1-state motion, which produces a DC voltage component. This implies the damping at zero frequency is important to the retrapping process, and thus

$$I_{r0} = I_c \frac{4}{\pi Q(0)} \quad . \tag{3-12}$$

Although this analysis is an oversimplification of the problem, it illustrates how two processes, in this case escape and retrapment, can sample the damping at different characteristic frequencies. Its importance with regards to resonant tunneling is to help answer the question: If a resonant tunneling event leads to the transmission of the particle through a barrier, will the particle continue to move toward the free-running state, or will it simply become trapped in a nearby well shortly thereafter? I expect from the preceding argument that I_m as defined above is the relevant parameter here, that is to say the damping at the plasma frequency must be sufficiently small that I_m as given by Eq. (3-11) must satisfy $I_m < I_m^{res}$ in order to observe the mth tunneling resonance manifested as an escape event.

Another feature which distinguishes a frequency-dependent shunt impedance from a simple ohmic shunt is that it can store energy which may come into play in the dynamics. For example, performing Monte Carlo simulations based on the model shown in Fig. 3-2 (b), KM found that the bias current for which the junction switched to the 1-state was affected by the value of the average voltage on the additional shunt capacitor C_S. In this case the energy stored in this capacitor gave the extra boost needed for an escape.

The conclusion drawn from these results is that the exact form of the shunt impedance has an important, even dominant, effect on the junction. While it facilitates an accurate simulation of the observed junction behavior, the drawback of a model such as that given by KM is that it is cumbersome to the point where many of the results of interest cannot be extracted without performing detailed numerical analysis or Monte Carlo simulations. The unfortunate implication is that any quantum-mechanical treatment of this model will most certainly be even more involved.

3.2 The Quantum Mechanical Treatment of Dissipation

The General Approach to Quantum Dissipation

Whereas replacing the resistance R in the RSJ model with a frequency dependent shunt greatly increased the complexity of the classical model, merely including the resistive shunt R itself, makes conventional quantum treatment of the problem impossible because a Hamiltonian for the system does not exist. However, a method has been developed to circumvent this difficulty which is readily generalized to arbitrary shunt impedances. While I am particularly interested in its application to the RSJ model, the problem of adding damping to a quantum system is quite general and was pioneered by Caldeira and Leggett (CL) [28, 29]. In this section I will present the Hamiltonian used by CL which represents a macroscopic system with dissipation, and review the results of a perturbative treatment of the terms in this Hamiltonian which represent the damping, as obtained by Esteve, Devoret, and Martinis (EDM) [32]. I will then give the results of this treatment for the case of a harmonic oscillator, from which comes the rate of decay Γ_d which I used in Chapter 2.

Consider a macroscopic classical system, or particle (with unit mass), with one degree of freedom described by the coordinate X which obeys the equation of motion

$$\ddot{X} + \hat{K}\{X(t)\} = -\frac{d}{dx}V(X) \ , \tag{3-13}$$

where $\hat{K}$ is a linear operator and V(X) is a potential. The dynamics of this system can be treated using the Hamiltonian formulation with the Hamiltonian $H_{macro} + H_{CL}$, where

$$H_{macro} = \frac{1}{2}P^2 + V(X) \tag{3-14}$$

and

$$H_{CL} = \sum_j \frac{1}{2}\left[p_j^2 + \omega_j^2 \left(x_j - \frac{c_j}{\omega_j^2} X \right)^2 \right] . \tag{3-15}$$

The term H_{macro} represents the macroscopic system without damping, while the term H_{CL} represents the environment and its coupling to the macroscopic system. The effects of dissipation are included in H_{CL}, which represents a set of harmonic oscillators with the jth oscillator coordinate, momentum, and frequency denoted by x_j, p_j, and ω_j, respectively. These oscillators are each coupled with strength c_j to the coordinate X, in analogy to attaching springs with masses to the particle. These oscillators and their couplings are chosen so that together they reproduce the action of the operator $\hat{K}$. This is accomplished when the spectral density of the oscillators

$$J(\omega) = \frac{\pi}{2} \sum_j \frac{c_j^2}{\omega_j} \delta(\omega - \omega_j) \tag{3-16}$$

satisfies

$$K(z) = -\frac{2z^2}{\pi} \int_0^\infty \frac{J(\omega')d\omega'}{\omega'[(\omega'^2 - z^2]} \tag{3-17}$$

such that

$$K(\omega) = \lim_{\mathrm{Im}\, z \to 0-} K(z) \tag{3-18}$$

where $K(\omega)$ is the Fourier transform of $\hat{K}$. As an example, in the case where the damping is proportional to velocity, $\hat{K} = \lambda d/dt$ and $K(\omega) = i\lambda\omega$. The damping provided by the resistor R in the RSJ model falls under this category, which is known as viscous or ohmic damping.

CL have argued the equivalence of these two classical representations. The advantage of the Hamiltonian representation is that it can be quantized, while its disadvantage is its infinite number of additional degrees of freedom. The original study

by CL determined the effects of damping on quantum tunneling, but since then this Hamiltonian has been used to study the motion of a quantum particle in a double well [40], a periodic potential [41-43], and a flat potential [44].

While one approach is to treat this full Hamiltonian immediately, EDM have started with the states $|n\rangle$ with energies E_n of the Hamiltonian H_{macro}, and treated the coupling between the set of oscillators and the macroscopic system as a perturbation to these systems. Using standard time-independent perturbation theory, they obtained energy level shifts ΔE_n, which in the limit of an infinite number of oscillators may be complex. The real part of the energy shift of a state is the actual change in energy of the level, whereas the imaginary part corresponds to the decay rate associated with the finite lifetime imparted to the state through its coupling to the dissipative environment. EDM found the real and imaginary parts of ΔE_n are given by

$$\mathrm{Re}(\Delta E_n) = \mathrm{Re}(L_n) + G_n \ , \tag{3-19}$$

and

$$\mathrm{Im}(\Delta E_n) = \mathrm{Im}(L_n) \ , \tag{3-20}$$

where

$$L_n = \hbar \sum_{m<n} M_{nm} K^*(\omega_{nm}) \tag{3-21}$$

and

$$G_n = \hbar \sum_{m} M_{nm} \frac{\omega_{nm}}{\pi} \int_0^\infty \frac{\mathrm{Im}(K(\omega))d\omega}{\omega(|\omega_{nm}|+\omega)} \ , \tag{3-22}$$

with

$$M_{nm} = |\langle n|X|m\rangle|^2 \tag{3-23}$$

and $\omega_{nm} = (E_n - E_m)/\hbar$. Note that L_n, whose imaginary part is proportional to the decay rate of the nth state, depends only on the states below the nth state through matrix elements M_{nm} of X and the damping at the Bohr angular frequencies ω_{nm}. The physical

interpretation of this is that the finite lifetime of the nth state results from damping-induced decay of the nth state to states lower in energy.

The Damped Harmonic Oscillator

As an example of the use of these expressions, I will find the decay rate of the states of a harmonic oscillator which is subject to ohmic damping of viscosity λ, that is, $K(\omega) = i\lambda\omega$. Let the potential of the oscillator be $V(X) = \omega_0^2 X^2/2$. The square of the matrix element between the states n and m is

$$\begin{aligned} M_{nm} &= 0, && |n-m| \neq 1 \\ M_{n,n-1} &= M_{n-1,n} = \frac{n}{2\omega_0}, && |n-m| = 1 \end{aligned} \quad , \tag{3-24}$$

and thus only the state immediately below $|n\rangle$ contributes to the sum L_n, giving

$$\mathrm{Im}(\Delta E_n) = \mathrm{Im}(L_n) = -n\hbar\frac{\lambda}{2} \quad . \tag{3-25}$$

The real part of the energy level shift is given by G_n because L_n is purely imaginary and does not contribute. Evaluating Eq. (3-22) yields

$$G_n = \frac{\hbar}{2\pi}\int_0^\infty \frac{\lambda d\omega}{\omega_0 + \omega} \quad . \tag{3-26}$$

Since this expression diverges, one could replace the upper limit of the integral of infinity with a cutoff frequency. A physical choice for the cutoff is unimportant, because G_n does not depend on n and the energy shift will be the same for all levels. Thus there will be no change in the energy level differences, which are the physical observables.

Decay Rates in the RSJ Model

By applying the above results to the RSJ model, I can obtain the decay rates I used in Chapter 2. The equation of motion given by Eq. (2-4) can be cast in the form of Eq. (3-13) be setting $X = C(\hbar/2e)^2\phi$. Then $\lambda = 1/RC$ and

$$V(X) = -C\left(\frac{\hbar}{2e}\right)^3\left[I_c \cos\left(\frac{X}{C(\hbar/2e)^2}\right) + I_{Bias}\left(\frac{X}{C(\hbar/2e)^2}\right)\right] . \qquad (3\text{-}27)$$

When $I_{Bias} = 0$, the harmonic potential given above approximates a well of the washboard potential, with $\omega_0 = \omega_p$. Thus, the imaginary part of the energy level shift is given by $Im(\Delta E_n) = -n\hbar/2RC$. The relationship between the imaginary energy shift and the rate of decay is $\tilde{\Gamma}_d = -2\,Im(\Delta E_n)/\hbar$, so the decay rate from the nth energy level to the (n-1)th level is given by

$$\tilde{\Gamma}_d = \frac{n}{RC} , \qquad (3\text{-}28)$$

which is the expression for the decay rate I used in the model theory presented in Chapter 2. This result is obtained using the harmonic oscillator approximation, and although the tilted washboard well is anharmonic, the corrections arising from the anharmonicity are well within the expected validity range of the RSJ model itself.

Correspondence of Quantum and Classical Behavior

While I have used quantum mechanical analysis for the dynamics occurring within the wells, I used classical analysis of the RSJ model in Section 3.1 to try to understand the motion of the particle after escape. One might wonder how the quantum theory of damping presented above carries over into the classical limit, and vice versa.

To help answer this question, I present two examples of the correspondence between quantum and classical treatments of damped macroscopic systems.

First, in the harmonic oscillator approximation for the RSJ model given above, I can estimate the rate of energy loss by multiplying the rate of decay of state $|n\rangle$ given by Eq. (3-28) by the amount of energy lost $\hbar\omega_p$ in a decay event to state $|n-1\rangle$ (the only transition allowed by the selection rule $\Delta n = 1$). Multiplying this rate of energy loss, $n\hbar\omega_p/RC$, by $2\pi/\omega_p$ gives the expected energy lost during a plasma oscillation. The resulting energy loss is equal to the energy of the nth state times $2\pi/Q$. This corresponds to the behavior of a classical underdamped oscillator with an energy E, which will lose an amount of energy $2\pi E/Q$ over one period of oscillation.

Second, Hakim and Ambegaokar [44] have used the CL Hamiltonian to solve the problem of a quantum free particle subject to ohmic damping. They found that the center of a Gaussian wave packet follows the classical trajectory, and the mean value of the momentum also follows the corresponding classical equation. Their results lend support to the CL treatment of dissipation. These results also support the use of classical equations of motion as an estimate of the actual behavior of a nearly free particle in the quantum limit, such as is the case for the free-running state of the quantized RSJ model.

CHAPTER 4

Experimental Strategy

The preceding chapters give some indication of the complexities involved in theoretically modeling the dynamics of Josephson junctions operated in the limit where resonant tunneling is likely to occur. Clearly, the subject is by no means a completed topic. However, the theory as I have developed it so far is at the point where I have enough of a framework to design an experiment to search for a signature of resonant tunneling, the hope being that preliminary experimental results could then be used to guide further theoretical work on the phenomenon. The conclusion drawn from the model theory was that the effect which lends itself most readily to observation is resonance-enhanced escape from the 0-state. The goal of this chapter is to develop an experimental strategy to measure the escape rate and to choose a design of a device such that the resonant enhancement of the escape rate should be clear and convincing.

First I will describe the current-ramping approach one uses to measure the escape rate as a function of bias current. Next I will show how a DC SQUID with a small self-inductance can be used as a substitute for a single Josephson junction because the dynamic behavior of these two devices should be identical under the appropriate conditions. The advantage of the DC SQUID over the single junction is that it provides a

critical current which is adjustable *in situ* by the application of a magnetic field, allowing tuning of the coupling between states in resonance and consequently the tuning of the overall escape rate. Finally, I will show how I derived practical design parameters for a SQUID and a measuring circuit which minimizes the electromagnetic loading of the device.

4.1 Measuring the Escape Rate

In Chapter 2 I obtained the rate of escape $\Gamma_{Esc}(I_{Bias})$ from a state of steady motion down the washboard potential to the 1-state. This escape rate was determined as a function of DC bias current I_{Bias}, assuming the system is prepared in the steady motion state while the junction is biased at that particular current. This condition is difficult to achieve in practice, for one cannot start with zero bias current and then quickly (on the scale of the characteristic time for escape) apply a non-zero bias current. In addition to the practical difficulties, this method would introduce an impulse to the system which cannot be described by a model which assumes a quasi-static bias current.

Rather than measure the rate $\Gamma_{Esc}(I_{Bias})$ directly, the standard approach [45] is to use the following technique: The bias current is ramped up from zero current and one records the value of current at which the junction switches. Repeating this many (typically 10^3 to 10^4) times, one builds up a histogram which approaches the statistical distribution $P(I_{Bias})$ for the probability that the junction will switch at the current I_{Bias}. The distribution $P(I_{Bias})$ will in general depend on both the rate of the current ramp and its functional form. For ease of both application and analysis, I will assume the ramping is linear in time with constant rate $dI_{Bias}/dt = \dot{I}_{Bias}$. Expressions describing how the quantities $P(I_{Bias})$ and $\Gamma_{Esc}(I_{Bias})$ depend on each other can be derived as follows: Suppose one performs a single current ramp starting with $I_{Bias} = 0$ and the junction definitely in the 0-state. Let $R(I_{Bias})$ be defined as the probability that at the current I_{Bias} the junction has not yet switched to the 1-state. In a small increment of bias current ΔI_{Bias} which occurs over a time $\Delta t = \Delta I_{Bias}/\dot{I}_{Bias}$, the change in R is given by $R(I_{Bias}+\Delta I_{Bias}) - R(I_{Bias}) = -R(I_{Bias})\Gamma_{Esc}(I_{Bias})\Delta t$, assuming the rate of retrapping is negligible. This may be expressed in differential form as

$$\frac{dR}{dI_{Bias}} = -\frac{R\Gamma_{Esc}}{\dot{I}_{Bias}} , \qquad (4\text{-}1)$$

which has the solution

$$R(I_{Bias}) = \exp\left[-\int_0^{I_{Bias}} \frac{\Gamma_{Esc}(I')dI'}{\dot{I}_{Bias}}\right] \tag{4-2}$$

where I have used the boundary condition $R(0) = 1$. The probability P is given by $P = -dR/dI_{Bias}$, so I obtain the result

$$P(I_{Bias}) = \frac{\Gamma_{Esc}(I_{Bias})}{\dot{I}_{Bias}} \exp\left[-\int_0^{I_{Bias}} \frac{\Gamma_{Esc}(I')dI'}{\dot{I}_{Bias}}\right]. \tag{4-3}$$

The inverse of Eq. (4-3) is obtained by substituting the identity $R(I_{Bias}) = \int_{I_{Bias}}^{\infty} P(I')dI'$ into Eq. (4-2), taking the natural logarithm of both sides and differentiating with respect to I_{Bias}. The result is

$$\Gamma_{Esc}(I_{Bias}) = \dot{I}_{Bias} \frac{P(I_{Bias})}{\int_{I_{Bias}}^{\infty} P(I')dI'}. \tag{4-4}$$

As noted above, the distribution P of the continuous variable I_{Bias} is not obtained directly in practice. Rather, a histogram is obtained by assigning the recorded switching events to bins along the current scale which are of equal width. Let $N(I_k)$ be the number of switching events observed in the current range of width ΔI centered at the bias current I_k, where k is an index. In the limit $\Delta I \rightarrow 0$, and as the total number of events approaches infinity, the histogram, normalized by the number of events, approaches $P(I_{Bias})$. Thus Eq. (4-4) has the discrete approximation

$$\Gamma_{Esc}(I_k) = \frac{\dot{I}_{Bias}}{\Delta I} \frac{N(I_k)}{\sum_{j \geq k} N(I_j)} \quad . \tag{4-5}$$

Let us now turn our attention to the inverse expression, Eq. (4-3). It can be seen that, for a particular escape rate function, the ramping rate $\dot{I}_{Bias}$ determines both the width and center of the $P(I_{Bias})$ distribution, with P broadening and shifting to larger currents as $\dot{I}_{Bias}$ is increased. A histogram composed of a finite number of switching events will have a minimum and maximum observed switching current. This determines the current range over which the measurement probes the escape rate function. Because of limitations resulting from both noise minimization and other practical considerations (these I will address in Section 5-4), the ramp rate can be varied over values covering only about two orders of magnitude. This implies that the range of escape rate values probed is fixed for all practical purposes. In fact, the relationship between P and Γ_{Esc} is such that if the escape rate is changed, the range of escape rate values probed remains relatively unchanged, while the current range shifts accordingly. This fixed range of probed escape rate values has the following implication for an experiment designed to observe peaks in the escape rate caused by resonant tunneling: The overall magnitude of the escape rate depends strongly on the amount of coupling between the states in resonance, which varies exponentially with the barrier height determined by the critical current of the junction. If the resonant tunneling peak has a magnitude which is greater than or less than the probed range of escape rate values, the junction will tend to switch before or after the resonance, respectively, and the peak shape will not be observed. This is illustrated schematically in Fig. 4-1. This presents a difficulty for the experimenter, who is then challenged to produce a junction with a critical current which falls within a narrow range of acceptable values.

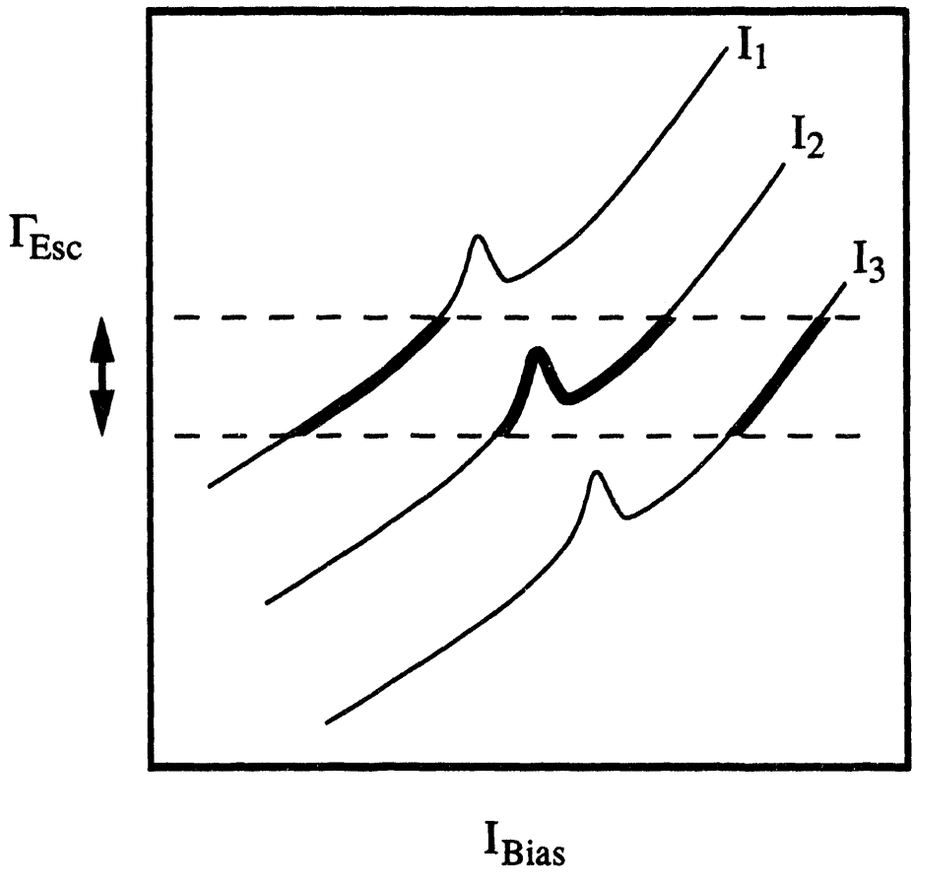

FIGURE 4-1. Schematic representation of the results of measuring the escape rates of three devices with critical currents $I_1 < I_2 < I_3$. The escape rate functions are shown by the fine lines with peaks indicative of resonant tunneling. The values of escape rate actually measured in a typical experiment fall within the fixed range indicated by the arrow, and are shown as bold lines.

4.2 The "Tunable" Josephson Junction

Producing a junction with the correct critical current would be a challenging task involving a great amount of trial and error. Fortunately, an alternative approach can be taken by substituting a current-biased DC SQUID with a small self-inductance for the single current-biased Josephson junction studied in the theory. For the purposes of observing resonant tunneling an appropriately designed SQUID behaves in a manner identical to its single junction counterpart, with the important advantage that it has a critical current that can be varied by the application of a static magnetic field. This allows the tuning of the critical current *in situ*, and thus the adjustment of the escape rate so that a peak in the escape rate can be made to fall within the range of values probed by a measurement of the escape rate. This technique, brought to my attention by Andrew Cleland, has been applied in other studies of superconducting devices both in the classical and quantum limits [46, 47]. In this section I will study the DC SQUID and argue how both in classical and quantum limits it can substitute for a single junction.

In order to facilitate a detailed understanding of the connection between the DC SQUID and the single junction, I will derive the equations of motion governing the dynamics of the SQUID, which has two degrees of freedom arising from the two Josephson junctions. In this analysis I will assume the device is symmetric, which is both adequate for the purposes of discussion and representative of the actual experiment. Analogous results for an asymmetric SQUID can be found elsewhere [48, 49]. A lumped circuit element model of the DC SQUID is shown in Fig. 4-2. Currents I_1 and I_2 flow in the left and right arms, respectively, and sum to the steady bias current $I_{Bias} = I_1 + I_2$. The symmetry of the device implies that the total self-inductance L can be divided in half such that I_2 couples a flux $LI_2/2$ through the SQUID loop, and similarly I_1 couples a flux $-LI_1/2$. Each junction is described by the RSJ model and has resistance R, capacitance C,

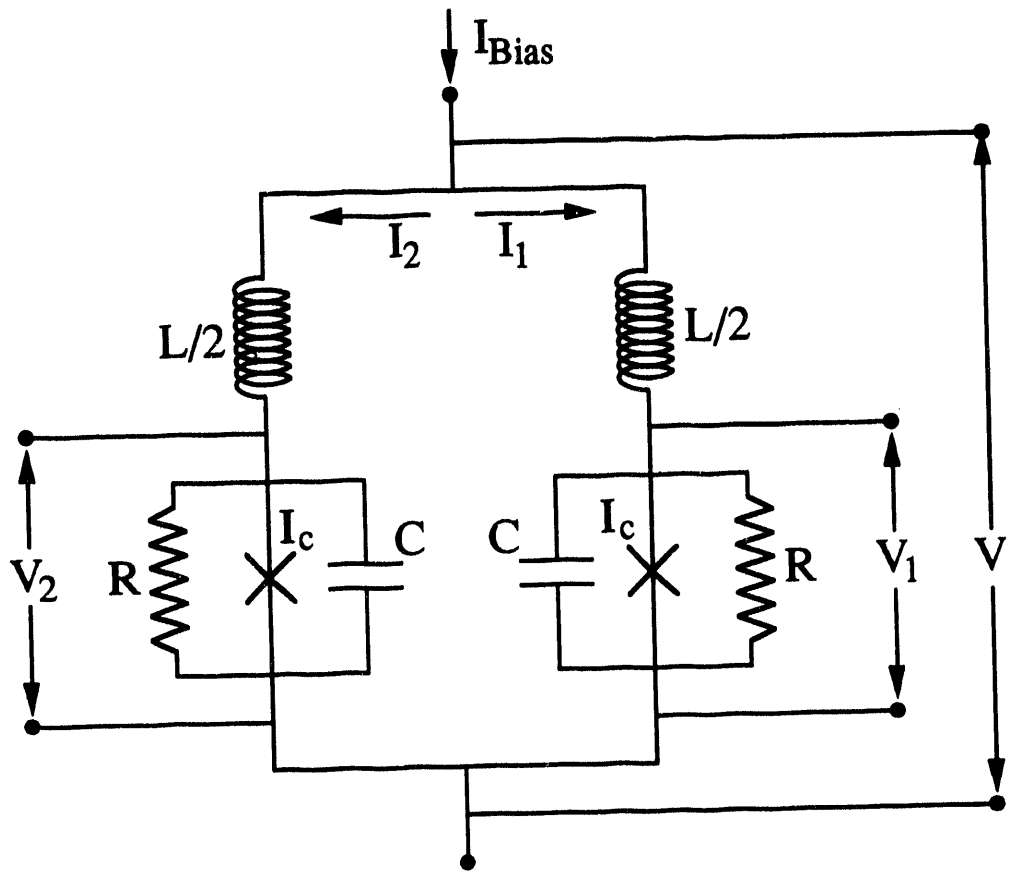

FIGURE 4-2. Lumped circuit element model of a symmetric DC SQUID.

and ideal critical current I_c. The current I_i through arm i is given in terms of the junction's phase variable ϕ_i by

$$I_i = I_c \sin\phi_i + \frac{\hbar}{2e}\left(\frac{1}{R}\right)\dot{\phi}_i + \frac{\hbar}{2e}C\ddot{\phi}_i \ , \tag{4-6}$$

and the voltage V_i across junction i is

$$V_i = \frac{\hbar}{2e}\dot{\phi}_i \ . \tag{4-7}$$

Because the bias current is held constant, the inductance divides the voltages V_1 and V_2 so that the voltage V across the entire device is

$$V = \frac{V_1 + V_2}{2} \ . \tag{4-8}$$

Defining the average phase difference ϕ as

$$\phi = \frac{\phi_1 + \phi_2}{2} \ , \tag{4-9}$$

I obtain the Josephson relation in its single junction form

$$V = \frac{\hbar}{2e}\dot{\phi} \ . \tag{4-10}$$

The total flux Φ linking the SQUID is given by

$$\Phi = \Phi_a + LJ \tag{4-11}$$

which is the sum of the applied flux Φ_a and the flux due to the circulating current J defined by

$$J = \frac{I_2 - I_1}{2} \quad . \tag{4-12}$$

Because the SQUID obeys fluxoid quantization the total flux Φ linking the SQUID is related to the phases of the junctions by

$$\phi_1 - \phi_2 = 2\pi\frac{\Phi}{\Phi_0} = 2\theta \tag{4-13}$$

where I have defined $\theta = \pi\Phi/\Phi_0$. The relations given by Eq. (4-9) and Eq. (4-13) are equivalent to changing coordinates from ϕ_1 and ϕ_2 to ϕ and θ, which are the coordinates of choice for relating SQUID dynamics to single junction dynamics. I can obtain the bias current I_{Bias} by adding I_1 and I_2. Written in terms of the variables ϕ and θ, the result is the first equation of motion for the system, which is

$$\frac{\hbar}{2e}(2C)\ddot{\phi} + \frac{\hbar}{2e}\left(\frac{2}{R}\right)\dot{\phi} + 2I_c\cos\theta\sin\phi - I_{Bias} = 0 \quad . \tag{4-14}$$

Note that this expression is formally identical to the equation of motion for a single junction with resistance R/2 and capacitance 2C, which are the equivalent parallel elements of the SQUID. The significant distinction is that the critical current is replaced by $2I_c\cos\theta$: Instead of a constant critical current, the effective critical current depends on the variable θ. The second equation of motion is obtained by combining Eqs. (4-6), (4-11), and (4-12). The result is

$$\frac{\hbar}{2e}(2C)\ddot{\theta} + \frac{\hbar}{2e}\left(\frac{2}{R}\right)\dot{\theta} - 2I_c\cos\theta\sin\phi - \frac{2\Phi}{L} + \frac{2\Phi_a}{L} = 0 \quad . \tag{4-15}$$

The two equations of motion given by Eqs. (4-14) and (4-15) can be viewed as describing the motion of a particle of mass proportional to 2C moving in a potential $U(\phi,\theta)$ with damping parameter proportional to 2/R, where the potential is given (in actual energy units) by

$$U(\phi,\theta) = \frac{2E_J}{\pi\beta}\left(\theta + \pi\frac{\Phi_a}{\Phi_0}\right)^2 - E_J\frac{I_{Bias}}{I_c}\phi - 2E_J\cos\theta\cos\phi \quad . \tag{4-16}$$

Here the parameter $\beta = 2LI_c/\Phi_0$ is the reduced inductance, and $E_J = \Phi_0 I_c/2\pi$ is the Josephson energy for one of the SQUID junctions. The potential, which is identical to the washboard potential for motion strictly in the ϕ direction (also called the longitudinal direction), has a strong parabolic dependence in the θ direction (also called the transverse direction) when $\beta << 1$. Thus it becomes clear how a small β device behaves classically as a single junction with critical current $2I_c\cos\theta$: Transverse motion is restricted because it is energetically unfavorable, so the particle moves along the washboard-shaped floor of a valley with very steep walls.

The effective critical current $2I_c\cos\theta$ of this quasi-one-dimensional device is controlled by applying the external flux Φ_a. The local minima of the potential given by Eq. (4-16) to a very good approximation fall on the line $\theta \equiv \pi\frac{\Phi_a}{\Phi_0}$ in the limit $\beta << 1$. Thus the applied flux is almost exactly equal to the total flux through the SQUID. Defining the maximum value of the SQUID critical current $I_c^{max} = 2I_c$ and the parameter $\eta = 2\frac{\Phi_a}{\Phi_0}$, I have the simple relation for the modulation of the critical current I_c^{device} of the "tunable" Josephson junction in the limit $\beta \to 0$:

$$I_c^{device} = I_c^{max}\left|\cos\left(\frac{\pi}{2}\eta\right)\right| \quad . \tag{4-17}$$

Note the parameter η varies linearly with applied magnetic field and takes on values from 0 to 1 as the device modulates from maximum to minimum critical current.

As a specific, more rigorous example of this quasi-one dimensional behavior in the classical regime, consider a particle which is in thermal equilibrium with a heat bath at temperature T as it moves in the two dimensional SQUID potential. This is shown schematically in Fig. 4-3. The transition from the local minimum A to the adjacent local minimum B via the saddle point S is made by thermal activation over the barrier ΔU_{AS}, which is the energy difference between the saddle S and the minimum A. The transition rate is given in the moderate to low damping limit by [46, 49, 50]

$$\Gamma_{2D} = \frac{\omega_{\|A}\omega_{\perp A}}{2\pi\omega_{\perp S}}\left[\left(1+\frac{1}{4Q_{2D}^2}\right)^{1/2} - \frac{1}{2Q_{2D}^2}\right]\exp\left(-\frac{\Delta U_{AS}}{k_B T}\right). \qquad (4\text{-}18)$$

Here the frequencies $\omega_{\|A}$ and $\omega_{\perp A}$ are the small oscillation frequencies at the minimum A for motion parallel and perpendicular to the direction of motion from A to S, and similarly $\omega_{\|S}$ and $\omega_{\perp S}$ are the small oscillation frequencies at the saddle S. The parameter Q_{2D} is defined as $Q_{2D} = \omega_{\|A}RC$, which is the quality factor for small oscillations in the bottom of the well A in the parallel direction. As $\beta \rightarrow 0$, the parallel and perpendicular directions approach the ϕ and θ directions, respectively, and $\omega_{\|A}$ approaches the plasma frequency of a single junction with capacitance 2C and critical current $2I_c\cos(\pi\eta/2)$. The ratio $\omega_{\perp A}/\omega_{\perp S}$ approaches unity approximately as $1+\pi\beta/2$. Thus, in the very low β limit, the escape rate Γ_{2D} for the two dimensional potential approaches the escape rate for a single junction, given by Eq. (3-7).

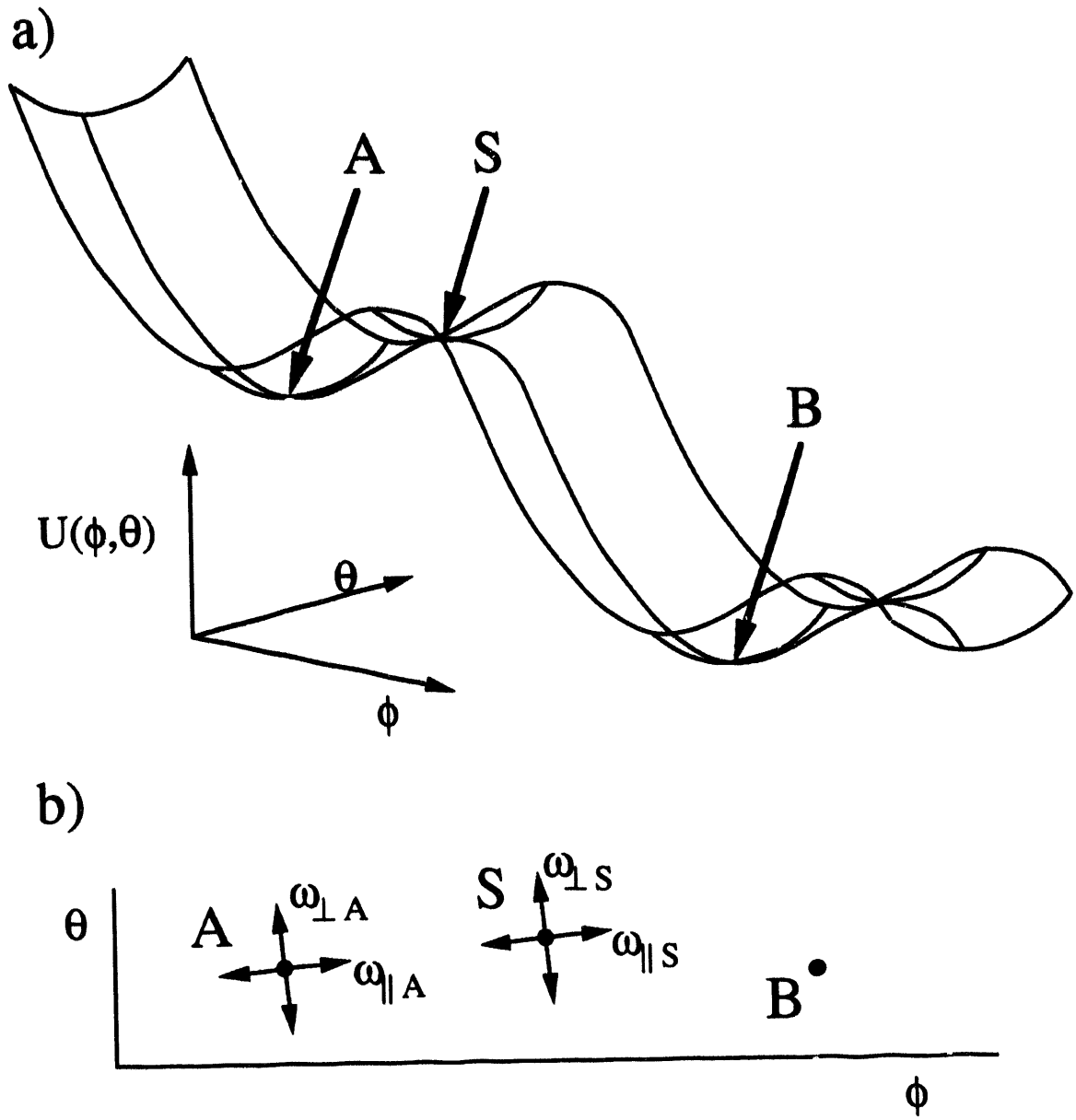

FIGURE 4-3. (a) Schematic representation of the two-dimensional SQUID potential $U(\phi,\theta)$. Points A and B are local minima, and S is a saddle point. Thermal transitions from A to B are made via the saddle at S. (b) The points A, S, and B in the ϕ-θ plane. Symbols and directions for small oscillation frequencies about the points A and S are shown (see text).

Does this classical quasi-one-dimensional behavior carry over into the quantum limit? I expect that to a good approximation the solutions to the Schrödinger equation will separate into transverse and longitudinal modes, and the transverse modes will have such large energy spacing that excitations of transverse modes will rarely occur. Unfortunately, because of the term $2I_c\cos\theta\cos\phi$ the Schrödinger equation is unseparable and the above assertion cannot be explicitly proven in a straightforward manner. However, because this term is small compared to the parabolic term which dominates motion in the θ direction, I may drop it as a first approximation and write down the transverse portion of the now separable Schrödinger equation:

$$\left[-2E_C\frac{d^2}{d\theta^2}+\frac{2E_J}{\pi\beta}\left(\theta+\pi\frac{\Phi_a}{\Phi_0}\right)^2\right]\Psi_n(\theta)=E_n^\theta\Psi_n(\theta)\,, \tag{4-19}$$

where $E_C = e^2/2C$ is charging energy of one of the SQUID junction capacitors. The solutions $\Psi_n(\theta)$ of Eq. (4-19) are harmonic oscillator wavefunctions with energy eigenvalues E_n^θ with spacing

$$E_{n+1}^\theta - E_n^\theta = \frac{\sqrt{8E_CE_J}}{\sqrt{\pi\beta}} = \frac{\hbar\omega_p}{\sqrt{\pi\beta}}\,, \tag{4-20}$$

where ω_p is the plasma frequency of one of the SQUID junctions. It is clear that for $\beta << 1$, this energy spacing is much greater than the level spacing associated with the longitudinal ϕ direction, which is of order $\hbar\omega_p$. Replacing the Josephson coupling term as a perturbation to the separable system, I can view the motion in the ϕ direction as an effective time dependent perturbation to the transverse problem. The characteristic frequency of this perturbation will be the plasma frequency which, according to Eq. (4-20), is much less than the Bohr angular frequency connecting transverse states.

Thus I can expect that system will remain in its transverse ground state, and it will behave quasi-one-dimensionally in the quantum limit.

4.3 Choice of Parameters for a SQUID

The next step in developing an experimental strategy is to choose target parameters for a SQUID. The starting point is to choose values for the number of levels in the well and the time scale for the dynamics, characterized by ν and ω_p respectively. These can be varied experimentally through the capacitance C and the critical current I_c, as the parameter ν is proportional to $\sqrt{I_c C}$, while ω_p is proportional to $\sqrt{I_c/C}$. (Unless explicitly noted, my notation henceforth will refer to the effective junction, so that I_c will denote twice the critical current of each SQUID junction times the modulation factor given by Eq. (4-17), and C will denote twice the capacitance of each SQUID junction.) The general strategy is to pick ν and ω_p so that the device switches to the 1-state for bias currents larger than the resonance value when $\eta = 0$, but the resonance subsequently "turns on" when the critical current is reduced by increasing η. The onset of the resonance peak would be the signature of resonant tunneling. This strategy has the additional advantage over measuring a set of single junctions which cover a range of critical current values in that it rules out the possibility of any peculiarities of a particular device causing the peak, and eliminates the variation of other parameters from device to device.

Of course, there are experimental constraints in making the choice of I_c and C. The material of choice for making submicron (I'm giving away part of the answer here unavoidably) tunnel junctions is aluminum because of fabrication issues which I will discuss in Chapter 5. For a particular oxide barrier thickness d, the specific capacitance of the tunnel junction is proportional to 1/d, while the tunneling resistance decreases exponentially as d increases [14]. This means that for a large range of tunneling resistances, the specific capacitance will be relatively constant. Although there is some disagreement as to its value [51], there is some consensus that the specific capacitance is about 45 fF/μm^2 for native grown Al_2O_x barriers [52], which is the value I will adopt.

Typical specific resistances obtained via thermal oxidation range from 10^2 to 10^4 Ω-μm^2. Assuming a superconducting gap of 370 to 400 μV, this implies critical current densities ranging from 3×10^3 to 3×10^6 A/m^2.

I will present the parameters I obtained in the last device I fabricated and tested during the course of this research, which I refer to as device A. The parameters are given in Table 4-1. Parameters that vary with η through the modulation of the critical current have their corresponding values listed for the values of $\eta = 0$, 0.8, and 0.95. Although this set of parameters is by no means optimized, it is in the range of appropriate values and will serve me for the purposes of discussion. Following the analysis of the results of measurements performed on this device, presented in Chapter 6, it will also serve as a starting point for a discussion in Chapter 7 concerning possible improvements on the experiment.

Several of the items listed in Table 4-1 warrant discussion. Note that the energy level spacing in temperature units are larger than temperatures that can be readily obtained by dilution refrigeration, which is nominally 20 mK. This ordinarily implies that the low temperature limit can be experimentally achieved, that is, the $T = 0$ approximation should be accurate. I will argue in Chapter 6 that for unforeseen reasons this condition was not actually realized in the experiment. For the present, however, I will proceed with the assumption of a 20 mK bath temperature, for it will serve to illustrate my intended design of the experiment. The lowest order ($m = 1$) resonance is listed as I_1^{res} and is calculated using Eq. (2-15), which assumes even level spacing in each well. Note that in this approximation, good to order $1/v$, the resonances will occur at currents which are integer multiples of I_1^{res}.

In order to observe the resonant tunneling effect, the escape rate must be dominated by resonant tunneling. Other mechanisms, such as "conventional" MQT (tunneling through a single barrier directly to the 1-state) and escape by thermal activation, must be negligible. Because the escape rates associated with each of these two

Parameter	Symbol	$\eta = 0$	$\eta = 0.8$	$\eta = 0.95$
Critical Current	I_c	226 nA	69.8 nA	17.7 nA
Capacitance	C	37 fF	"	"
Normal Resistance	R_N	1.39 kΩ	"	"
Total Junction Area	A_{Tot}	0.82 μm^2	"	"
Plasma Frequency	ω_p	1.4×10^{11} rad/s	7.5×10^{10} rad/s	3.8×10^{10} rad/s
Quantum Levels Parameter	ν	10.4	5.8	2.9
Energy level spacing (Temperature units)	$\hbar\omega_p/k_B$	1.0 K	0.57 K	0.29 K
Resonance Current	I_1^{res}	6.9 nA	3.8 nA	1.9 nA
Thermal Activation Switch Current	I_{switch}^{TA}	225.9 nA	69.5 nA	16.6 nA
Conventional MQT Switch Current	I_{switch}^{MQT}	219 nA	62.6 nA	10.6 nA
Minimum Allowable Quality Factor	Q_{min}	41	23	12
Minimum Allowable Shunt Impedance	R_{min}	11 kΩ	13 kΩ	17 kΩ

TABLE 4-1. Parameters of device A, for three values of η. Critical current under $\eta = 0$, total junction area, and normal resistance are measured quantities; other quantities are obtained from theoretical models by using these values, as described in the text.

mechanisms increase exponentially as the bias current is increased, quantitative estimates of whether these mechanisms are negligible can be obtained by estimating the bias currents at which each mechanism, acting alone, would cause the junction to switch to the 1-state while operating with a nominal bath temperature of 20 mK. If these switching currents are much greater than the resonance current I_1^{res}, the resonant tunneling, which depends sensitively on Q in contrast to the other mechanisms, can be made to dominate at the resonance current by choosing a sufficiently large Q. These two switching currents, which I define as the currents at which the escape rates are equal to $10^2\ s^{-1}$, I denote by I_{switch}^{MQT} and I_{switch}^{TA} for MQT and thermal activation, respectively. I choose the rate $10^2\ s^{-1}$ because it is a rate which typically falls in the middle of the values probed by an escape rate measurement experiment. Values of I_{switch}^{MQT} and I_{switch}^{TA} for device A determined using Eqs. (2-42) and (3-7) respectively are listed in Table 4-1. They are not only well above the resonance current values, but in fact fall within the single energy barrier regime in which these escape rate formulas are valid.

The resonant tunneling escape rate requirements for Q could be determined at this point, but it turns out that a greater constraint on the minimum acceptable Q is imposed by retrapping effects, as discussed in Chapter 3. Following the lead of Kautz and Martinis (KM) [26], I will generalize the constant quality factor $Q = \omega_p RC$ of the RSJ model to a frequency-dependent quality factor defined by $Q(\omega) = \omega_p R(\omega) C$, where $R(\omega)$ is taken to be the inverse of the the real part of the admittance shunting the ideal junction element and the junction capacitance. In order for the effect to be observable in a current-ramping experiment, I must ensure that the quality factor at the plasma frequency, $Q(\omega_p)$, is large enough so that retrapping occurs for a current less than I_1^{res}, thus allowing the particle to complete the transition to the 1-state and remain in that state long enough for this state to be detected as a non-zero voltage across the device. According to the analysis given in Chapter 3, and in analogy with the definitions for I_{switch}^{MQT} and I_{switch}^{TA}, I define the current I_{retrap}^{TA} as the current at which the retrapping rate given by Eq. (3-10)

with $Q = Q(\omega_p)$ is equal to 10^2 s^{-1} at 20 mK. Using $Q = Q(\omega_p)$ effectively replaces the RSJ parameter I_{r0} of Eq. (3-1) by the appropriate parameter I_m of the frequency-dependent damping model, given by Eq. (3-11). Although it was derived for the RSJ model, the retrapping rate of Eq. (3-10), when evaluated using $Q(\omega_p)$ gives a more strict upper bound on the damping since $Q(\omega_p)$ is usually bounded from above by Q(0). The minimum allowable values of $Q(\omega_p)$ for device A, determined by setting I_{retrap}^{TA} equal to I_1^{res}, are listed in Table 4-1 as Q_{min}. Note that in a practical experiment the value of $Q(\omega_p)$ should be chosen much greater than Q_{min} to ensure that I_{retrap}^{TA} is actually well below I_1^{res}. The minimum shunt impedances R_{min} corresponding to the values of Q_{min} are also given in Table 4-1.

Finally, the value of the self-inductance of the SQUID must be chosen. A SQUID loop with an inner diameter of a few micrometers is quite readily fabricated using the techniques described in Chapter 5. The area A_{SQUID} of the loop of device A was $A_{SQUID} = 120\ \mu m^2$. Estimating the inductance L by using the formula

$$L = 1.25\mu_0\sqrt{A_{SQUID}} \tag{4-21}$$

gives L = 17 pH. For the critical current of device A, this gives a reduced inductance of $\beta = 1.9 \times 10^{-3}$. This value is small enough to ensure quasi-one-dimensional behavior. According to Eq. (4-20), the transverse mode has level spacing about 13 times greater than the level spacing associated with the wells of the longitudinal washboard potential.

4.4 Designing a High Impedance Shunt

The minimum requirements for the isolation of the device from its electromagnetic environment were determined in the previous section. The experimental challenge is to come up with a tractable scheme for accomplishing this goal. The primary difficulty arises when one connects conventional leads to the device for the purposes of supplying the current bias and measuring the voltage. Typical stray capacitances of conventional leads are hundreds of picofarads, which would present unacceptably low impedances at high frequencies. To avoid the inevitable capacitive loading from using lengthy (lengthy here may mean only millimeters!) pieces of wire, highly resistive thin-film leads can be fabricated on the Si chip as close to the device as is practical. Resistances per unit length of about 20 kΩ can be fabricated by using a metallic SiCr alloy formed into a strip with a cross section which is nominally 100 nm in width and 5 nm in thickness. I will model the impedance $Z_{lead}(\omega)$ presented by one of these thin film leads in order to obtain a quantitative estimate of the quality factor $Q(\omega) = \omega_p C/\mathrm{Re}(1/Z_{lead}(\omega))$ at all frequencies from zero frequency to just beyond the plasma frequency. Details of the actual fabrication of these leads will be given in Chapter 5.

The lead is modeled as a metal strip of width w, thickness t, and length Λ lying on a Si substrate. For the nominal cross section of w = 100 nm and t = 5 nm, the total self-capacitance C_L of the strip is estimated [26] to be $C_L = (2.8 \times 10^{-17}\ \mathrm{F/\mu m})\Lambda$, and the total inductance L_L is given by [53] $L_L = (1 \times 10^{-12}\ \mathrm{H/\mu m})\Lambda$. The total resistance of the lead R_L depends on the resistivity of the material and the exact geometry of the lead. For device A, which had Λ = 27 μm, it was R_L = 770 kΩ = (28 kΩ/μm)Λ. The distributed elements of resistance, capacitance, and inductance form a transmission line of finite length. A detailed analysis of this system may be found in Andrew Cleland's thesis [54]. The most important results, however, can be understood by the following relatively

simple analysis: A short length $d\Lambda$ of the transmission line can be modeled by the lumped circuit elements dR_L, dL_L, and dC_L, as shown in Fig. 4-4 (a). The entire line is then represented by a large number of these segments. I can ignore the inductive elements because their impedance is much smaller than that of the resistive elements for frequencies below 10^{16} Hz, which is much greater than the plasma frequency. At low frequencies, the resistive elements dominate, and the impedance of the line is simply $Z_{line} = R_L$. As the frequency increases, the capacitors begin to short the line to ground, and only a length of the line less than Λ contributes to the impedance. The frequency ω_{cross} at which this crossover occurs is $\omega_{cross} = (R_L C_L)^{-1}$. Above ω_{cross}, the line can be represented as an infinite ladder of circuit elements as depicted in Fig. 4-4 (b). The impedance Z_{ladder} of this network can be found by first noting that an additional rung added to the ladder will not change this impedance. Writing the equivalent impedance of this circuit, shown in Fig. 4-4 (c), I can solve for Z_{ladder}, and by taking the limit as dR_L, $dC_L \rightarrow 0$ while holding the ratio $R_L,/C_L$ constant, I recover the result of the full transmission line analysis in the high frequency limit. The real part of the admittance $1/Z_{line}$ is

$$R(\omega) = \sqrt{\frac{2R_L}{\omega C_L}} \quad . \tag{4-22}$$

Thus I have the important result that at frequencies above ω_{cross}, the quality factor $Q(\omega)$ drops off as $\omega^{-1/2}$.

I can now use these results to estimate the quality factor for device A. First of all, note that attaching four identical leads, two at each terminal of the SQUID, presents the same shunt impedance as one lead. The crossover frequency for this lead was $\omega_{cross} = 1.7 \times 10^9$ rad/s, meaning that for frequencies below this value the impedance was 770 kΩ and the quality factor for $\eta = 0$ was 8.6×10^6. However, at the plasma frequency,

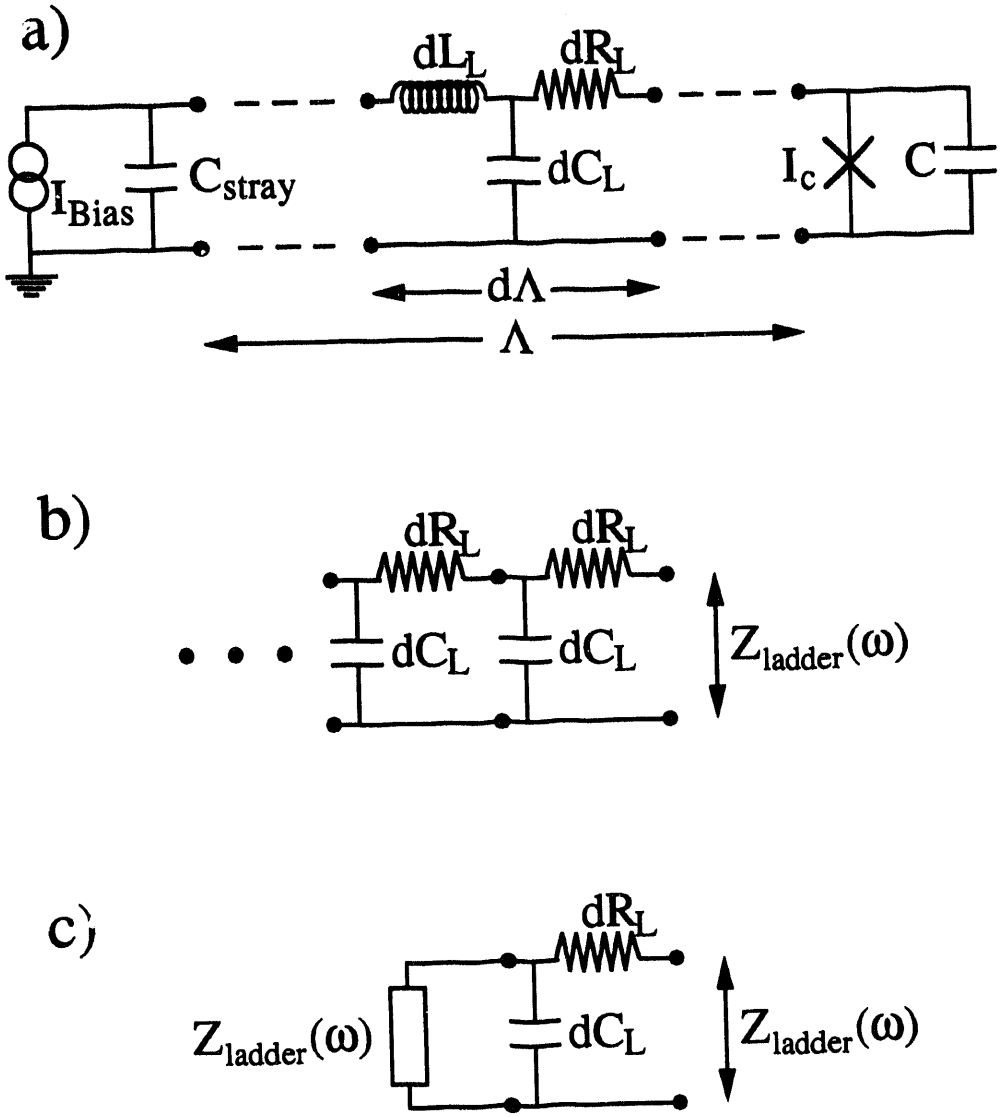

FIGURE 4-4. (a) Circuit model of junction, bias circuitry, and on-chip thin film resistive leads. The junction with critical current I_c and capacitance C is shown at the right of the figure, and the bias circuitry consisting of an ideal current source I_{Bias} with stray capacitance C_{stray} is shown at the left of the figure. The thin film lead of length Λ is shown in the middle, modeled as segments of length $d\Lambda$, with each segment containing the lumped circuit elements dR_L, dL_L, and dC_L. (b) The high frequency model of the lead, which is a semi-infinite ladder of segments with elements dR_L and dC_L and equivalent impedance $Z_{ladder}(\omega)$. (c) An equivalent circuit to (b) which aids in solving for $Z_{ladder}(\omega)$.

$R(\omega_p) = 120\ k\Omega$, and the quality factor was $Q(\omega_p) = 620$. Similarly, for $\eta = 0.95$, $R(\omega_p) = 230\ k\Omega$, and $Q(\omega_p) = 320$. Thus, within the RSJ model augmented by frequency-dependent damping, these values are large enough to ensure that retrapping should not occur immediately following an escape event at the resonance current when operating at a bath temperature of 20 mK.

CHAPTER 5

Experimental Technique

In this chapter I describe the process I used to fabricate devices representative of the parameters I outlined in Chapter 4, and the experimental setup and measurement techniques I used in obtaining data, with a discussion of the noise effects which are involved in measuring the switching current.

5.1 Fabrication of the SQUIDs

Shadow Evaporation Lithography Technique

From a lithography viewpoint, the device parameters outlined in Chapter 4 call for generally small features. The junction size should be submicron (~0.5 μm^2 each), the SQUID loop must be smaller than about 10 μm in diameter, and to obtain sufficient resistance per unit length using manageable materials and deposition techniques, the on-chip resistors need to be about 0.1 μm in width and about 30 μm long. Although these are generally not state-of-the art with regard to minimum attainable dimensions, they call for techniques beyond standard optical lithography.

The "industry standard" technique for producing submicron tunnel junctions is to use electron-beam lithography with a bi-layer resist to create a bridge of suspended resist which then can be used as a shadow mask for thermal evaporations at oblique angles. This technique, called the shadow evaporation lithography technique, was developed primarily at Bell laboratories [55, 56]. The basic concept of how this technique is used to form a submicron junction is illustrated in Fig. 5-1 and described below. A substrate (shown in Fig. 5-1 (a)) is covered with two layers of resist, where the layer closest to the substrate is a resist chosen to be more sensitive to the exposure/development process than the upper layer. A beam of electrons, accelerated by a voltage between 5 and 30 kV and focused to a spot size of about 20 nm, is used to write a straight line on the resist, except for a short interruption. In this exposure process, the energetic electrons break bonds in the long chain of the resist polymer. A solvent for the polymer is used to develop the resist by dissolving away the shorter segments of the polymer. The developed pattern is shown in Fig. 5-1 (b). The upper layer develops in such a way that it forms an open channel except where the line exposure was interrupted. The more sensitive lower layer develops into a wide channel, undercutting the upper layer including underneath the unexposed segment of the line. This creates a bridge composed of the upper resist which

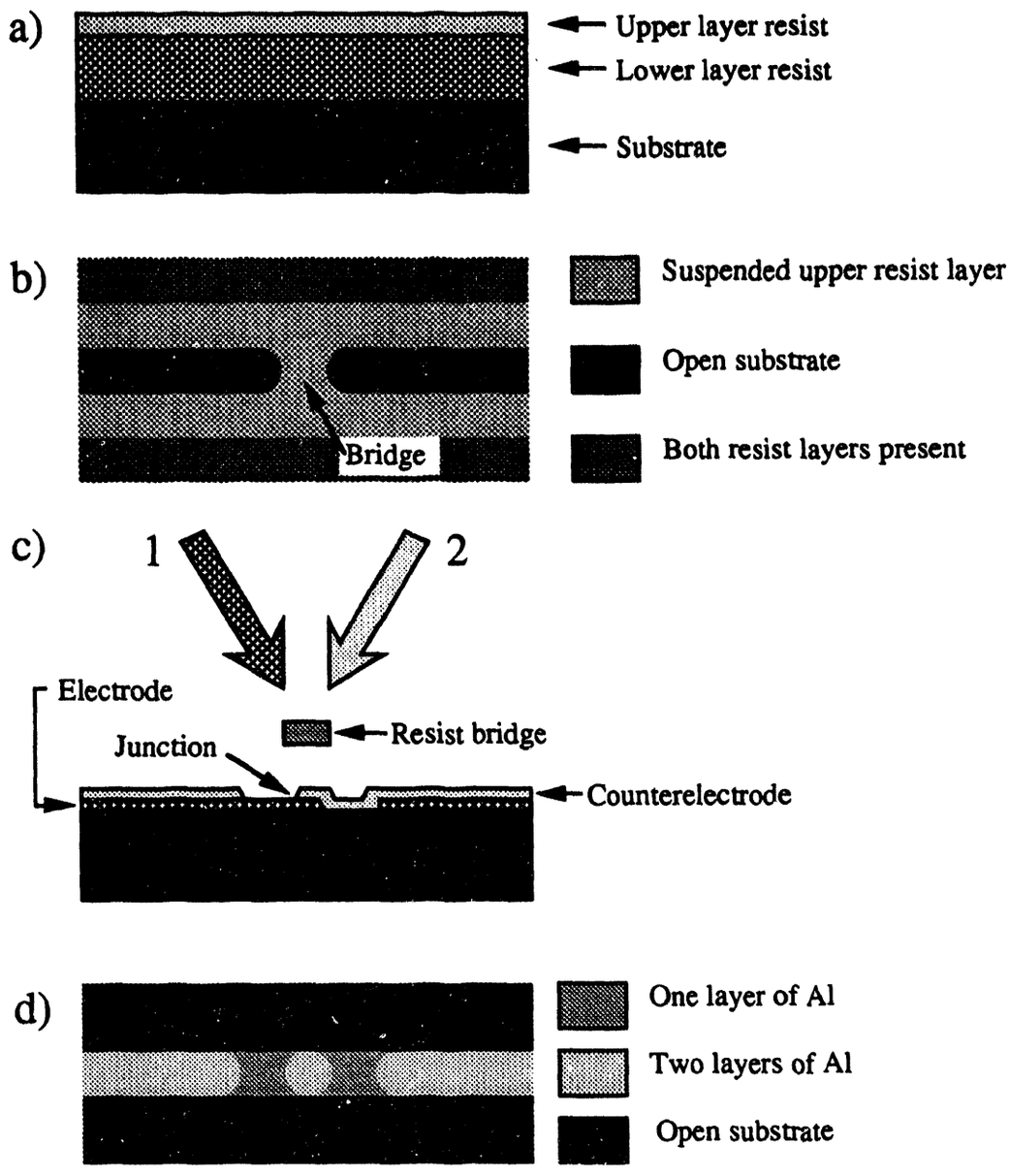

FIGURE 5-1. The shadow evaporation lithography technique. (a) Side view of the bilayer of two resists on a substrate. (b) Top view of the exposed and developed resist. The top resist layer forms an open channel interrupted by a suspended bridge, and the bottom resist layer forms a wide channel. (c) Side view. Evaporations from the directions indicated, labeled 1 and 2, form the electrode and counterelectrode, respectively, of the junction as indicated in the figure. (d) Top view of the completed device after lift-off. The junction lies where the two "fingers" overlap.

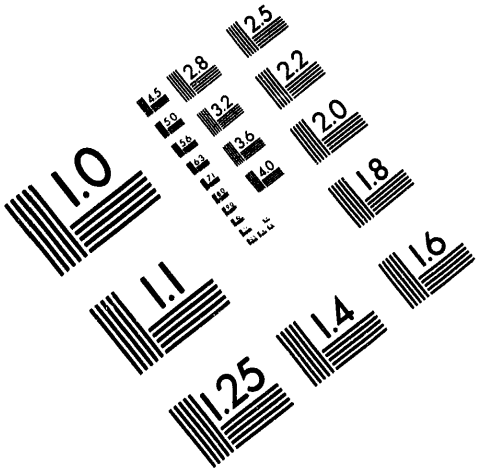

Association for Information and Image Management
1100 Wayne Avenue, Suite 1100
Silver Spring, Maryland 20910
301/587-8202

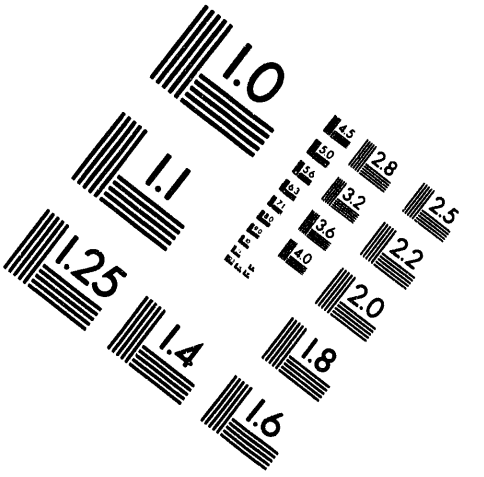

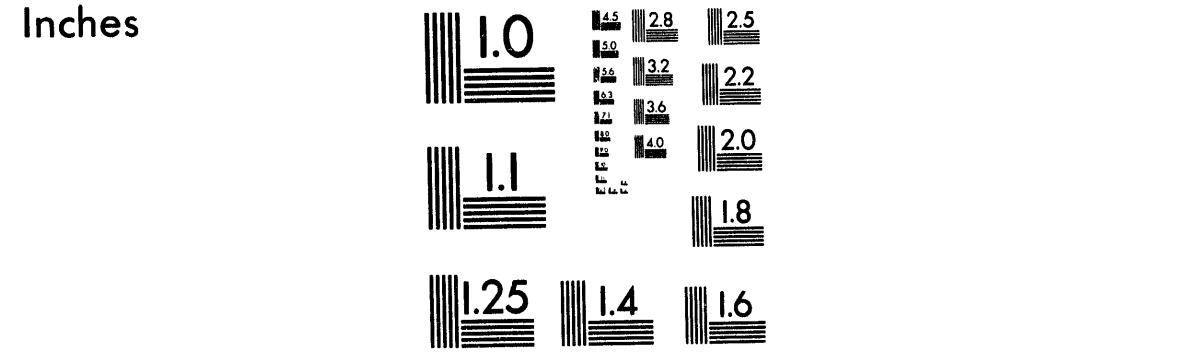

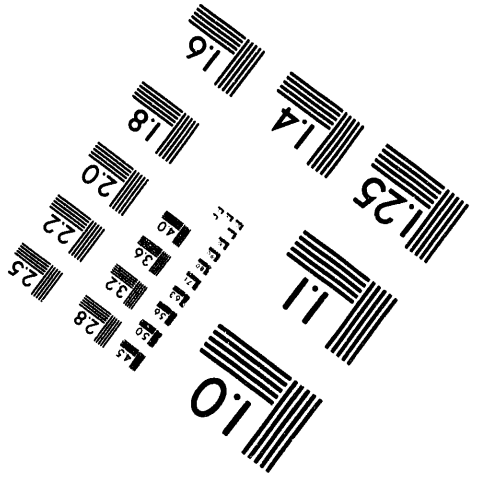

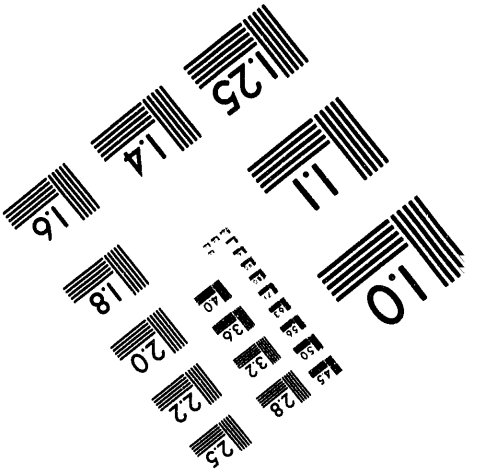

2 of 2

spans the lower channel, suspended above the bare substrate. The first electrode material is deposited by thermal evaporation in a direction which is in the plane of the exposed line, but at an angle from the normal to the substrate (typically between 0 and 45 degrees, depending on the application). This forms a metal line on the substrate surface except for an interruption where the bridge has cast a shadow. An oxide layer is formed on the surface of the first electrode by bleeding oxygen into the vacuum deposition chamber. The second electrode material is then deposited by thermal evaporation in a direction which is also in the plane of the exposed line, but at an angle opposite the angle used for the first evaporation and chosen so that the second electrode pattern overlaps the first electrode pattern and forms the junction. The evaporation steps, which have the advantage that they can be carried out without breaking vacuum, are illustrated in Fig. 5-1 (c). A subsequent liftoff of the remaining resist leaves the pattern illustrated in Fig. 5-1 (d). Linewidths on the order of 0.1 μm are readily attainable with e-beam lithography, and the evaporation angles can be adjusted to give an overlap of 0.1 μm or less. As a result, junctions with areas less than 0.01 μm^2 are readily obtained using this technique, and larger area junctions may be formed by increasing either the linewidth or the overlap length.

Choice of Electrode Material

Typically Al is chosen as the electrode material because it is simple to evaporate and forms a controllable oxide barrier by mere exposure to oxygen. It also forms continuous superconducting films without any extra precautions, in contrast to Sn which was used in early submicron junction research [12]. Junctions made of Al in this manner have also been found to have remarkably stable tunnel resistance through multiple thermal cycling and long (weeks to months) exposure to air. The disadvantage of Al is that its critical temperature is only 1.2 K, which is smaller than that of Sn or Pb and is below liquid He temperatures. This is not a problem for my application, which already

calls for millikelvin temperatures. In addition, the critical temperature of the material will only enter into the resonant tunneling dynamics as a parameter via its relation to the damping provided by the quasiparticle tunnel current, and this current is negligible at these temperatures.

Scanning Electron Microscope Lithography Apparatus

Lithographic exposures and device inspections were performed on an Etec Autoscan scanning electron microscope (SEM) owned by Prof. Van Duzer of the U. C. Berkeley Electrical Engineering Department and located in room 144 Cory Hall. Historically, this machine was originally designed to be used in standard SEM mode, but was adapted for e-beam lithography in the 1970's by Maurice Bales and others by the inclusion of a computer drive for the beam deflection system and the necessary electronic interface hardware. Further minor modifications of the SEM column and sample stage were made by Andrew Cleland and myself for submicron tunnel junction research carried out prior to this work. The complexities of the exposure pattern required by the present experiment warranted my development of a new pattern generation system, consisting of a Macintosh IIx computer, interface boards from National Instruments, additional hardware to interface this new computer to the existing interface unit, and original software for designing exposure patterns and carrying out exposures.

The resulting e-beam lithography system had the following specifications: Available beam currents ranged from 0.1 pA to 500 pA as measured by a Faraday cup in a custom sample stage. Resolution was about 20 nm, corresponding to the minimum spot size. Exposures could be carried out over a field of view which depended on the magnification setting of the microscope. Typically the fine details of the pattern were exposed at either 200 $\times$ or 400 $\times$ magnification, giving either a 150 μm or 75 μm wide square field of view, respectively. Contact pads were exposed at the lowest (10 $\times$) magnification, which gave a 3 mm field of view. The pattern generator had 12-bit

resolution in the x and y directions, so that the field of view was covered by 4096×4096 pixels. Available pixel exposure times ranged from 10 μs to 32,000 s, although typical exposure times were on the order of 1 ms. Patterns could contain a total number of exposure pixels limited only by the computer memory of 4 MB, and were composed of lines and blocks of pixels where the density of exposed pixels could be varied. No beam blanking was available for the system. However, the computer drive I designed allowed fast (~8 ms) switching between the lithography mode and the SEM mode. For beam currents of use the latter mode would not expose the resist over times of less than several hours, and thus a beam blanking option was effectively supplied by this feature.

Geometry of the Exposure Pattern

The shadow mask evaporation technique described above is readily adaptable to more complex devices containing multiple connections and additional materials. I devised a technique by which one can fabricate a DC SQUID with four thin-film resistive isolation leads complete with contact pads that employs only one lithographic step and three thermal evaporations which are performed in a single pump down. (Compare this to a conventional Clarke group DC SQUID which requires at least five lithography steps!) In order of deposition, the three evaporations are: First, the resistor material, which was a SiCr alloy in the case of device A (Most of the devices I fabricated used a NiCr alloy instead of SiCr for the resistor material, but unless specifically noted I will refer to device A in this section.); second, the Al electrode denoted by Al-1; and third, the Al counterelectrode denoted by Al-2.

The fine exposure pattern used to make device A is shown in Fig. 5-2, and details of one of its junction regions and one of the joints between the SQUID body and a resistor are shown in Fig. 5-3. The coarse pattern used to define large contact pads is not shown. For clarity in discussion, I will refer the pattern and angle evaporations to a Cartesian coordinate system with the origin located on the substrate surface at the center

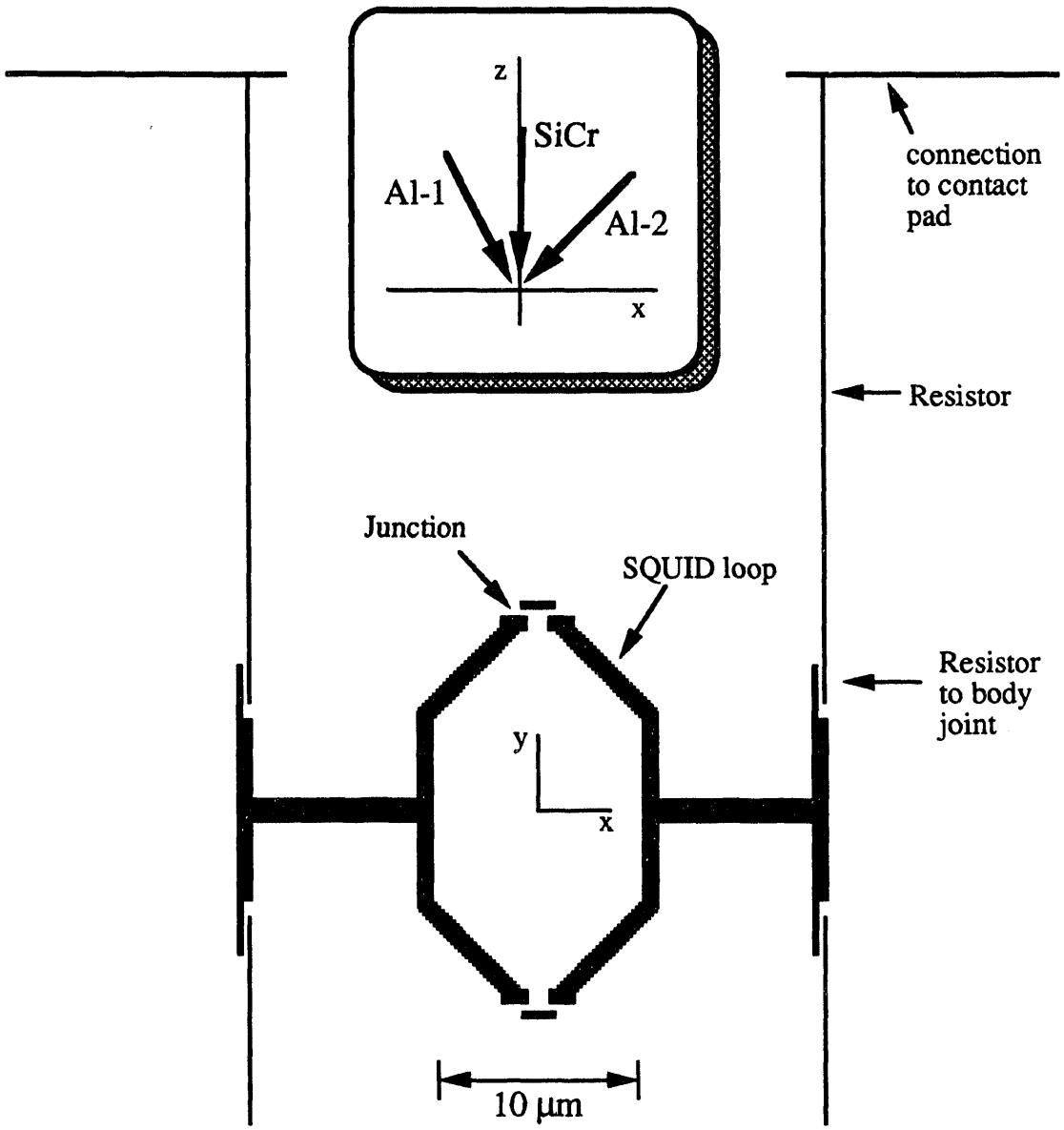

FIGURE 5-2. Exposure pattern used for device A. The scale is shown at the bottom of the figure, and the coordinate system referred to in the text is shown in the center of the SQUID loop. The pattern is symmetric about the x axis, and extends beyond the boundaries of the figure. Inset at top: Angles used for evaporations of SiCr, Al-1, and Al-2.

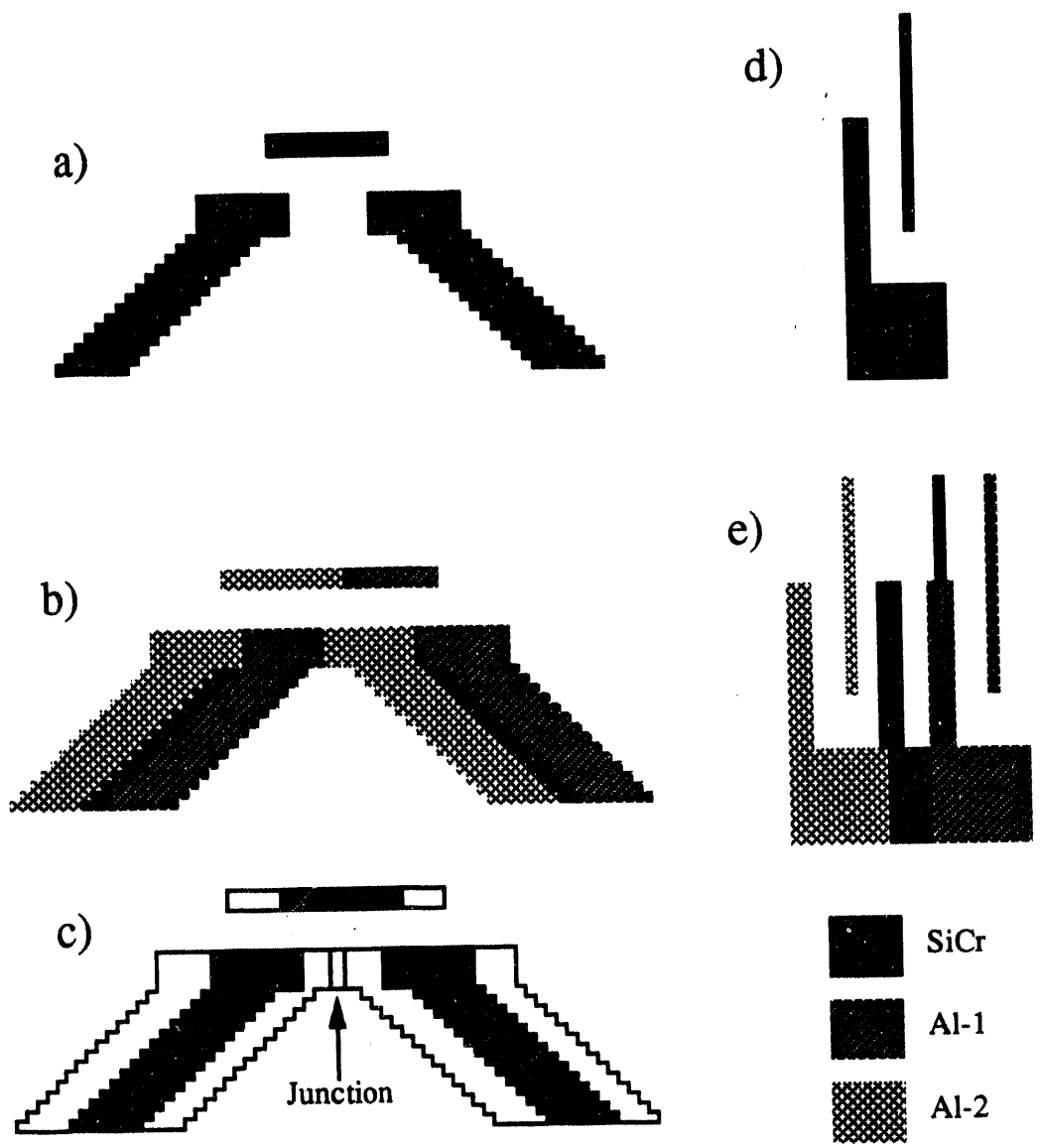

FIGURE 5-3. Details of the exposure pattern and completed device near a junction and a resistor/SQUID body joint. (a) Junction pattern. (b) Completed junction, with the three thin film layers shaded according to the key in the corner of the figure. (c) Completed junction, with the SiCr layer in black, and the Al-1 and Al-2 layers outlined for clarity. The junction is the overlapping region indicated. (d) Joint pattern. (e) Completed joint, with the three thin film layers shaded according to the key.

of the SQUID loop. The directions x and y are in the plane of the substrate as indicated in the figures, and the normal to the substrate is the z direction. As shown in the inset of Fig. 5-2, the angles of the thermal evaporations SiCr, Al-1, and Al-2, which were 0.3, –27.6, and 45.5 degrees from normal, respectively, all lie in the x-z plane.

To understand this pattern and how the junctions and interconnections are formed as a result of the three angled evaporations, it is useful to think in terms of three reproductions of the pattern which are translated the following distances in the x direction: The SiCr pattern is at the center, the Al-1 pattern is translated 0.59 μm in the x direction, and the Al-2 pattern is translated 1.1 μm in the –x direction. These lengths are given by the height of the upper resist layer above the substrate, which is 1.1 μm for my bilayer recipe (given below), multiplied by the tangent of the angle of the evaporation. These superimposed translated patterns are illustrated for the details shown in Fig. 5-3.

Each resist bridge used to form a junction (see Fig. 5-3) was 1.1 μm wide (in the x direction) and 0.75 μm long (in the y direction) for this pattern. The latter dimension determines the width (in the y direction) of the junction overlap, while the junction overlap length (in the x direction) is determined by the former bridge dimension and the translation distances given earlier. The resulting overlap was 0.44 μm. While the junction area could be varied by changing the evaporation angles, I found changing the bridge dimensions was preferable because it allowed me to avoid affecting other parts of the device fabrication which depended on the evaporation angles. The exposed boxes located just outside the SQUID loop near the resist bridges served as aids to the undercutting process beneath the bridges both by giving an additional exposure dose to that region and by creating an additional path for the developer to get in and for the developed resist to rinse away. Note in Fig. 5-3 (c) that the bridge shadowed the resistive material deposited in the first evaporation in such a way that this material was away from the junction overlap, which thus occurred over bare substrate.

The resistors were formed by the SiCr evaporation. Since the resistor channels ran in the y direction, the Al-1 and Al-2 evaporations produced superconducting lines running parallel to and on both sides of each resistive strip. These Al strips were connected to the contact pad. In order that these Al strips would not short out the resistor, I devised a scheme so that only the SiCr connected to the SQUID body, specifically to the layer Al-1. The geometry of one of these resistor/SQUID body joints, which were all identical, is illustrated in Fig. 5-3. The resulting contact was made over an area of approximately 0.1 $\mu m \times 1.8\ \mu m$. The fact that this small area was sufficient to make good contact between the SiCr and the Al-1 illustrates one of the advantages of the shadow mask lithography technique: Because these evaporations were performed in a single pump down and there were no intervening lithography steps, the surfaces remained clean and oxide free. By contrast, getting good contact between different layers was a problem resulting from combined optical and e-beam lithography in my previous research effort [25].

At all four joints, the SiCr resistors connected to the Al-1 layer. On the $x > 0$ side of the device, contact between the Al-1 layer and the Al-2 layer was made over the large area overlap of these layers which constituted the body of the SQUID on the $x > 0$ side of the junctions. Because the Al-1 surface was oxidized before deposition of the Al-2 layer, this contact actually formed a large area Josephson junction in series with the SQUID. Because this junction had an area much greater than the combined areas of the SQUID junctions while its oxide barrier had the same thickness, its critical current was much greater than the maximum critical current of the SQUID.

Finally, note in the geometry of the pattern that the SQUID loop was defined by arms which were at angles about 45 degrees from the x direction. This shape of the loop, which I call the "diamond" shaped loop, was an important feature of the design. Many devices which I fabricated employed NiCr for the resistor material and had a loop which was rectangular in shape with sides parallel to the x and y directions. These devices did

not show the modulation of critical current with applied magnetic field which is characteristic of a DC SQUID. I discovered this was probably the result of the absence of a coherent superconducting path around the loop of the SQUID. In the rectangular loop case, the Al-1 layer laid directly on top of the NiCr layer for distance of about 5 μm on each side of the SQUID loop. I believe the NiCr layer caused the coherence of the superconducting order parameter to be broken along these paths either by magnetic scattering or by proximity effects. By contrast, the geometry of the diamond shaped loop was designed so that a width of at least 0.4 μm of the inner edge of the loop was composed of Al on top of bare substrate. This was sufficient to provide a coherent superconducting path around the loop to give fluxoid quantization. Additional evidence in support of this hypothesis is provided by two test devices I made with rectangular loops, one with Al substituted for the NiCr, the other with a CuAu alloy (which has no magnetic component) substituted. Both of these devices showed critical current modulation.

Finally, as a general strategy for pattern design, the order in which the various parts of the pattern were exposed was chosen so that adverse effects of defocusing, lateral (x or y directional) beam drift, and beam current variations would be minimized. For example, the resistors were exposed first, since they were the features most sensitive to defocusing and dosage variation, and the exposures defining the junction resist bridges were performed in immediate succession because their positioning was critical.

Device Processing Techniques and Recipes

Because lithography in general, and e-beam lithography in particular, is something of an art as well as a science (some may even call it black magic), I will try to describe in some explicit detail the complete process I developed for fabricating a device. While all the parameters are not necessarily optimized, the recipe presented reflects a great deal of development and improvement over the techniques reported previously [54]

which I used for previous research projects. Following the recipe, I will present additional discussion about some of the discoveries I made during the course of my research concerning the exposure/development process.

The devices were fabricated on individual 11 mm × 11 mm Si chips, cut from 2" diameter (100) orientation wafers with resistivities of 1 to 10 Ω-cm and with 1000 nm of oxide grown on their surface as an insulating layer. Resists were spun on chips individually to avoid bilayer resist thickness variations resulting from the spin-coating process, which tends to produce a thinner coating at the edge of a large wafer than in the middle. The preparation of the substrates with bilayer resist was carried out in the U. C. Berkeley Microfabrication Facility. Before dicing, the wafer was coated with Shipley 1400-31 photoresist spun at 6000 rpm for 30 seconds and baked on a 70 C hotplate for 2 minutes to give a clean protective covering in anticipation of the relatively dirty dicing process. The wafer was diced using the Disco diamond saw, and rinsed with water. The photoresist was removed with acetone, then the chips were left in clean acetone for 5 more minutes. The chips were placed in an ultrasonic bath of concentrated RBS-35 detergent (Pierce Chemical Co.) for 5-10 minutes, then rinsed with deionized water and blown dry.

The e-beam resists were obtained from OCG Microelectronics. The lower layer of resist was the copolymer Poly(methylmethacrylate/methacrylic acid) (P(MMA/MAA)), type I, 9% in cellosolve. The upper resist was the polymer Polymethylmethacrylate (PMMA), 950K weight, 4% in chlorobenzene, which I thinned to 2% with chlorobenzene. The P(MMA/MAA) was spun on each chip at 2000 RPM for 30 seconds, and then the chips were placed on a glass slide and baked in a hotplate oven for 15 minutes at 150 C. A second layer of P(MMA/MAA) was spun on, also at 2000 RPM for 30 seconds, and baked in the same manner for 45 minutes. This layer was added to give additional thickness to the copolymer layer. The PMMA was spun at 3000 RPM for 30 seconds and baked at 150 C for 60 minutes. During this procedure I allowed

sufficient time to ensure that the chips were at room temperature before applying each additional layer of resist. Measurements of the thickness of PMMA resist applied in the manner described above, performed by Cleland, indicate that the upper layer resist thickness was about 100 nm. From angle evaporation tests I inferred that the upper resist layer was at a height of 1.1 μm above the substrate. Chips prepared by this procedure were found to give good results even after months of storage.

The exposure depended critically on sharp focusing of the e-beam. To facilitate this, I placed a small (~1/2 mm) patch of submicron sized Ag particles which were rough in shape at a point near the center of the chip using a sharpened wooden applicator which had been dipped in a mixture of the Ag particles and methanol. This provided an excellent subject at the surface of the resist on which to focus. The chip was then placed in the SEM chamber on the sample mount. The accelerating voltage was set to 18 kV. After allowing the beam a minimum warm-up time of 10 minutes, the condenser current was adjusted to give a beam current of 1.0 pA. The beam current was found to be stable to within about five percent over the time required for a typical exposure (a few minutes). The beam was then focused on a Ag particle near the edge of the patch to the best possible resolution, at least to about 50 nm (the focusing was performed at 40,000 × or greater magnification). The magnification was then set to 400 ×, and the stage was moved a distance of about 50 μm away from the Ag patch, which placed the entire patch outside the field of view to ensure that the pattern would not coincide with any of the particles. I found it was important not to move the stage too far, however, for a small tilt of the stage away from normal to the beam would result in the chip surface falling outside the focal plane. (I found the depth of field was about ± 2 μm, so a tilt of up to 1 degree would be acceptable for a translation of 50 μm.) The fine pattern described above was then exposed using pixel dosages which I will discuss later. Upon completion of the fine pattern exposure, the magnification was set to 10 ×, the condenser was set to give

maximum beam current (about 300-500 pA), and the coarse pattern was exposed to define contact pads.

The exposed chip was blown with dry N_2 to remove the bulk of the Ag particles. The remainder were removed by spraying the chip with distilled water, and in difficult cases, by an ultrasonic distilled water bath. I discovered this step was important for increasing yield, for on several occasions during the wet development process a single Ag particle lodged in a newly developed resistor channel and could not be cleared. (Using an ultrasonic bath at that point was found to destroy the delicate bridges and overhangs.)

The chip was developed in a 1:1 mixture of cellosolve (CS) and methanol (MeOH), and rinsed in a stop bath of isopropyl alcohol (IPA). The cellosolve I used is also known as 2-ethoxyethanol, ethyl cellosolve, or ethylene glycol monoethyl ether (The Saclay group is rumored to have experienced difficulties for a few weeks by unknowingly using a different type of cellosolve, so I have taken care to be very specific here!). The development procedure, which I will discuss later in greater detail, was a repeating sequence of dipping the chip in CS/MeOH, then IPA, then blowing it dry with N_2, performed as follows:

1. CS/MeOH, 4 seconds;
2. IPA, 15 seconds;
3. Blow dry;
4. CS/MeOH, 4 seconds;
5. IPA, 15 seconds;
6. Blow dry;
7. CS/MeOH, 3 seconds;
8. IPA, 15 seconds;
9. Blow dry.

The chemicals were held at a temperature of 21 ± 0.05 C by placing their containers in a water bath.

Thin-film deposition was performed in an evaporator for which I had constructed an apparatus which allowed tilting of the substrate without breaking vacuum. This allowed thermal evaporation at angles up to 50 degrees from the normal to the substrate. The evaporator was diffusion-pumped with a liquid nitrogen cold trap, and had a base pressure of about 2 x 10^{-6} Torr. Material thicknesses were monitored using a quartz oscillator. Although the calibration for this monitor was not known to better than a factor of about 1.5 for most materials evaporated, this system provided excellent reproducibility in thickness measurement, which was much more important for this experiment than exact knowledge of film thicknesses.

The thin films were deposited in the following procedure: The resistive film (of either SiCr or NiCr) was deposited first. Then the evaporation angle was adjusted, and the electrode Al-1 was evaporated. The oxidation procedure was performed, during which the evaporation angle was again adjusted. Finally, the counterelectrode Al-2 was evaporated.

The NiCr films were made by placing three to four 100 mm pieces of #20 gauge Nichrome wire (of exact composition which remains a mystery, for it was obtained from a poorly labeled spool in the electronics shop, and the so-called Nichrome alloy comes in a myriad of compositions) wrapped into tight balls, into a conical-shaped 3-stranded-wire W basket (from the R. D. Mathis Co.). Thicknesses of 5 to 30 nm were obtained at deposition rates of 0.05 to 0.2 nm/s. These films had resistivities of about 120 $\mu\Omega$-cm.

The SiCr films were obtained by placing three small pieces (about 1 mm in diameter each) of a SiO-Cr sinter into a W evaporation boat. This sinter, which was 65% Cr by weight, was prepared by Andrew Cleland, who mixed Cr powder and SiO powder together and had the mixture pressed and fired in an oven at LBL. The boat was heated to just below the evaporation point, then quickly heated using highest power. In this manner, an effective "flash" evaporation took place, which was done to avoid an inhomogeneous film resulting from the differing evaporation rates of Si and Cr. The total

volume of sinter evaporated was consistent with the thickness of the films obtained (~6 nm). The resistivity of this material was about 2600 μΩ-cm, more than twenty times the resistivity of the NiCr.

The Al films were deposited by placing a 150 mm length of 1/16" diameter 0.9999 purity Al wire into the same style 3-stranded-wire W basket used in the NiCr evaporations. Fast deposition rates of 5 to 15 nm/s were used to avoid oxidation during deposition caused by residual gas in the chamber. Film thicknesses were usually 25 to 35 nm.

The electrode was oxidized by introducing 3 Torr of 30% O_2/Ar into the chamber for 5 minutes. By varying the pressure by a few Torr or the oxidation time by a few minutes, junction resistances could be varied in a reasonably controlled manner.

Liftoff of the resist and films was accomplished by placing the chip in a boiling acetone bath for about 15 minutes. (A liftoff in room temperature acetone usually requires several hours). The chip was rinsed in clean acetone and blown dry. This step completed the device fabrication.

Details of the Exposure/Development Process

The exposure and development processes are of course central to electron beam lithography. These two processes are very sensitive to an endless number of parameters, and recipes for these must be developed concurrently, for each is intricately related to the other. Although a great deal of research has been done in this area, applications and equipment vary so widely and the process is sufficiently complex that in practice each researcher must develop his own particular recipe. I have listed some of the references which I have found most useful in developing my recipe: These are refs. [57-64].

The classic challenge of e-beam lithography is to achieve minimal linewidth. This was of course the case in my experiment, specifically because I needed to achieve as large a resistance per unit length as possible for the lead resistors. A constraint added

when performing shadow mask lithography is that one also has certain minimal requirements for undercut, and the upper and lower layers of resist are exposed and developed in the same process. Finally, the height of the upper resist above the substrate needs to be of a similar length scale as the pattern translations. In my particular application most of the device features were relatively large from an electron beam lithography viewpoint, so the thickness of the lower layer had to be scaled up accordingly. This meant a large amount of the copolymer had to be removed in the exposure/development process, which was difficult to achieve while keeping the linewidth defined in the upper resist small.

The actual cross-sectional profile of the developed region depends in a complicated manner on the spatial dependence of the energy deposition and the rate of solubility of the exposed resist. A number of simulations of this process have been carried out [61-64]. Greeneich has given the relationship for the amount of energy a given number of electrons accelerated by a particular voltage will deposit in the resist as a function of depth [61]. Where this function peaks, the development rate will be greatest, and this peak moves to greater depth as the energy is increased. I performed a series of exposures using different accelerating voltages, adjusting each dose for minimal upper resist linewidth. The effect of varying the accelerating voltage on bilayer development is schematically illustrated in Fig. 5-4. Using a smaller accelerating voltage results in resist removal near the top of the lower layer, as shown in Fig. 5-4 (a), while using a larger accelerating voltage results in a more columnar profile, as shown in Fig. 5-4 (b). Neither of these profiles is acceptable for they do not have an appropriate undercut. The ideal profile is illustrated in Fig. 5-4 (c): Using an appropriately chosen accelerating voltage results in most of the electron beam energy being deposited near the middle of the lower resist layer. In my experiment, I found that profiles similar to the cases shown in Fig. 5-4 (a) and (b) resulted when I used accelerating voltages of 16 kV and 20 kV,

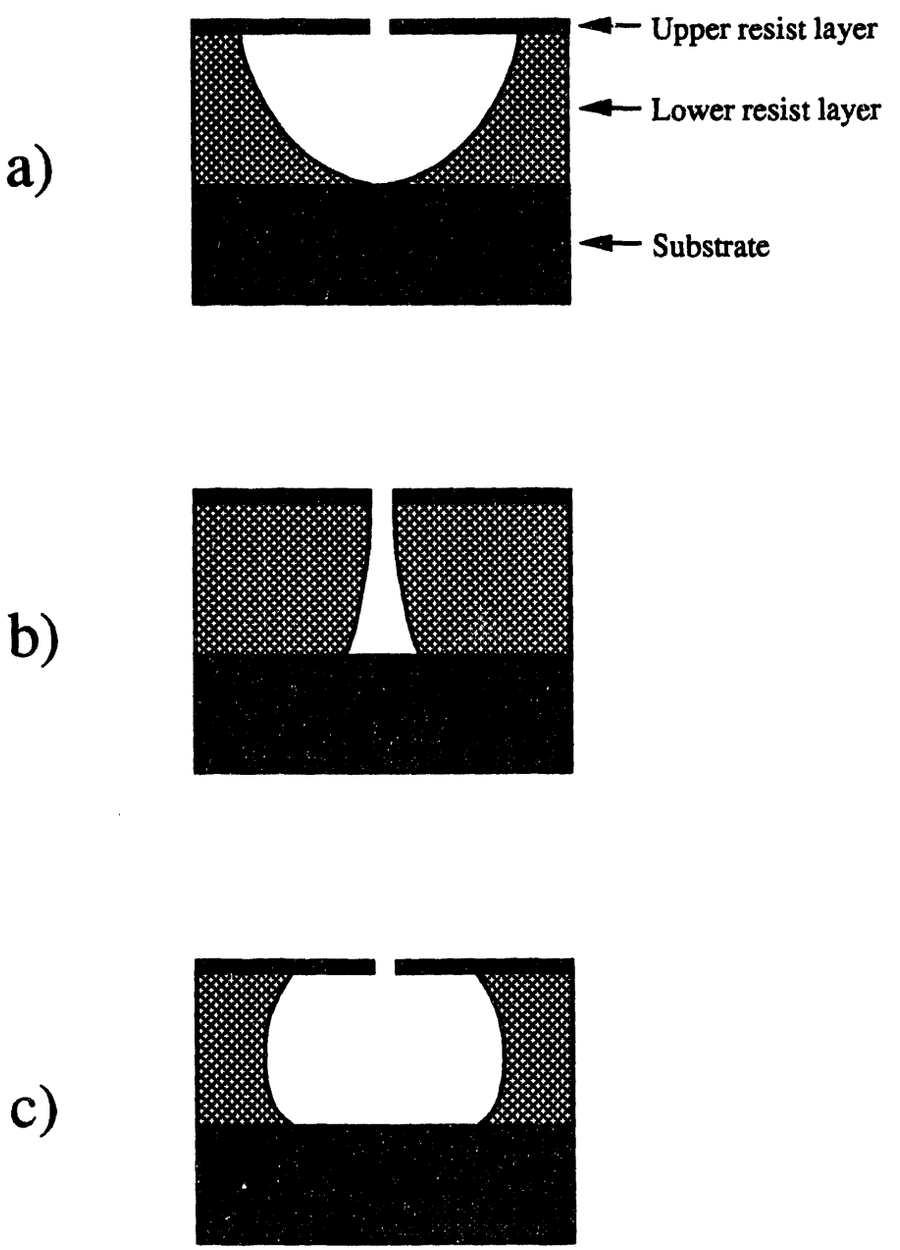

FIGURE 5-4. Side view of bilayer, schematically illustrating the result of exposure with three different accelerating voltages. (a) Low voltage (~16 kV). (b) High voltage (~20 kV). (c) Optimal voltage choice (~18 kV).

respectively, while the optimal behavior illustrated in Fig. 5-4 (c) was achieved using 18 kV.

I obtained the best results by using a beam current of 1.0 pA and operating at 400 × magnification, which gave a pixel spacing of 0.018 μm. For large regions such as the body of the SQUID I used a pixel density such that every pixel in the region was exposed for a time of 0.56 ms (corresponding to an average area dosage of about 1.7 Coulombs/m^2). The resistors were exposed as a strip two pixels wide, with each pixel exposed for 1.1 ms.

I experimented with several developing processes before settling on the process described above. In addition to mixtures of CS and MeOH, I tried combinations using Methylisobutylketone (MIBK), also a commonly used developer. I found that MIBK, while having the advantage of acting on a much longer time scale, did not in general give the extent of undercut I required, although others have obtained good results using MIBK with thinner bilayer systems. In my earlier work [25] I had used a 1:2 ratio of CS/MeOH as a developer with MeOH as a stop rinse. However, I found that MeOH by itself acts as a developer (although weaker than pure CS) and was creating some of the undercut during the "stop" process. For this reason I switched to IPA, which seemed to behave effectively as a true stop rinse. Also, I found pure CS did not give sufficient undercut, and I concluded that CS and MeOH must be used together to obtain the best results for my application. This behavior is not unusual; the improvement of developers by mixing different types has been studied previously in similar processes [60]. My development process also takes advantage of my discovery that more undercut was obtained by using several develop/rinse/dry steps than by using a single step having the same total development time. I attribute this effect to the saturation of the developer chemicals near the developing regions when the single step approach is used. Multiple steps allow the developer to "refresh". Finally, I found that good temperature control of the developer chemicals was paramount to a reproducible process. While I did not search for an

optimal temperature, I found that even a few degrees of temperature variation would change development times quite a bit and in extreme cases of elevated temperature would ruin the process altogether.

5.2 Sample Mount and Measurement Environment

Dilution Refrigerator Setup

The low temperature measurements were carried out using the Oxford Model 75 dilution unit and cryostat (built in-house) that was used for the MQT experiments [5]. The $^3He/^4He$ circulation system used with this refrigerator was designed by myself and constructed with the help of Mark Ferrari.

Since the time that the MQT experiments were completed, I performed a great deal of rewiring of the cryostat's experiment leads and replaced several of the heat sinks included with this wiring.

In total, I provided the refrigerator with sixteen wires dedicated for experimental measurements. These wires are arranged as four sets of wires, where each set of four wires was intended for a four point measurement of a sample. Each set of four wires, shielded from the other sets, was twisted together whenever possible, and kept as closely together as possible otherwise, to reduce interference. In the He bath shielded 4 conductor cable was used because I found it generated the least amount of microphonic current noise, which was an important consideration because of the high impedance (~1 MΩ) of my devices. Removable low-pass RC filters were installed just above the vacuum can top in the He bath. These filters, potted in Stycast 2850 FT mixed with stainless steel powder to attenuate microwave frequency transmission around the filters, have their 3 dB point at 16 kHz. Inside the vacuum can, the wiring consists of 0.003" diameter manganin wires, and each set of four wires is shielded from the other sets. The wires are heat sunk at the heat exchanger plate (which is at a temperature of about 120 mK) as described below. More 0.003" manganin wire was used to make the final connection to the sample mount at the mixing chamber. In total each lead has a capacitance of about 1 nF, which is dominated by the capacitance of the filter . Without the RC filter installed, the capacitance is about 300 pF.

My heat sinks were made by making a laminate of 0.002" BeCu sheet (chosen primarily because it is a resistive alloy), a Kim-wipe tissue, and a 1/8" Cu plate (to be clamped to the sinking point) bonded together with Stycast 2850 FT epoxy. The BeCu was then patterned into 1 mm × 20 mm strips using standard printed circuit board lithography techniques. The porous Kim-wipe aided in avoiding electrical shorting between the BeCu strips and the Cu plate while providing no effective additional material interfaces presenting Kapitza thermal resistance. A simple model by Andrew Cleland shows that this system forms an effective heat sink when used at the heat exchanger plate or the mixing chamber.

A carbon resistor, made by the Matsushita Corp., was used for the mixing chamber thermometry. Its resistance was measured using a Rochlin [65] bridge which also had a feedback system to provide temperature regulation of the mixing chamber by heating a metal film resistor also mounted on the mixing chamber. Unfortunately, the calibration of a carbon resistance thermometer tends to drift in time, and this particular thermometer has not been calibrated in five years. For this reason, the temperatures noted in this work are probably at best nominal temperatures.

The refrigerator can (but not necessarily on demand!) attain temperatures below 20 mK. Typical cooling power is about 1 μW at 25 mK.

The dilution refrigerator is suspended by bungee cords to reduce vibration, and is housed within a Cu screen room to shield radio frequency interference. Mu metal shields can be placed around the cryostat to reduce magnetic field noise. The gas manipulation system is located outside of the screened room, and care was taken to avoid mechanically coupling vibrations produced by the pumps to the refrigerator.

Sample Mount

Leads made of 0.003" manganin wire were attached to the Al contact pads with pressed-on pieces of In. The chip was mounted with silicone grease to a chip carrier

consisting of another piece of Si which was epoxied to a Cu plate with Stycast 2850 FT. Also epoxied to the chip carrier was a metal film resistor for current sensing which had a resistance of 1.00 MΩ at room temperature. Three of the wires attached to the device contact pads directly connected to the wires which ran up the cryostat as described above. The other pad was connected to the current-sensing resistor, which had wires connected to its ends which also ran up the cryostat. (See section 5-3 for the full circuit description.) The chip carrier was clamped to a Cu body which attached to the mixing chamber with a tapered Cu thread joint. This setup ensured good thermal contact between the chip and the mixing chamber. An estimate of the current noise induced in the SQUID by the Johnson noise produced by normal metal in close proximity to the device [66] indicated this noise would not be a problem, primarily because of the very small loop size of my SQUID and the very low temperature of the normal metal found in the device mount. The SQUID was enclosed in superconducting shield made of an aluminum tube of square cross section. This tube, which was open at both ends, was sufficiently long to attenuate external magnetic fields [67] by a factor of greater than 10^4. To modulate the critical current of the SQUID, a 30-turn persistent current magnet was placed inside the shield near the sample. This magnet was operated in persistent current mode while data was taken to ensure no current noise would be coupled into the SQUID. Because the heat switch for this magnet dissipated too much power for it to be mounted on the mixing chamber, it was instead mounted on the 1 K pot. The superconducting leads of the magnet were run up to the heat switch inside CuNi tubing tinned with Pb/Sn solder to make a superconducting shield, and the switch itself was located inside a Pb shield. This was to ensure that these leads would not act as the pickup loop of a flux transformer and inject noise into the shielded sample mount.

5.3 Measurement Setup

The bulk of the measurements performed were either of current-voltage characteristics or of switching current distributions to determine the escape rate. The circuit used to obtain the current voltage characteristics is schematically illustrated in Fig. 5-5, and the circuit used to obtain the switching current distributions is shown in Fig. 5-6.

Each circuit contains several common features. A linear voltage sweep was provided by a Hewlett-Packard 3325A function generator, located outside the screened room. To check for the effects of noise generated by this source, I often substituted either a simple battery and potentiometer voltage drive or an analog battery-powered linear voltage ramp generator for the digital function generator, placing them within the screened room. I found no difference in the data obtained by these methods and the data obtained using the function generator. The voltage drive was fed into a voltage splitter, which consisted of an op-amp follower ((+) output) and an op-amp inverter with adjustable amplitude ((–) output). The splitter was necessary to avoid problems caused by limited common mode rejection of the voltage sensing amplifier employed to measure differential signals which were very small compared to the voltages developed across the high resistance (~750 kΩ) current lead resistors. The amplitude of the (–) output was adjusted so that the voltages of the junction voltage sensing leads remained as close to ground as possible during the voltage sweep. The wires leading out of the cryostat were double shielded and connected to the inputs of EG&G PARC model 113 low-noise amplifiers, which were powered by batteries and could be placed inside a mu-metal shield.

The current sensing resistor for the current-voltage characteristic measurements was typically a room temperature 1.00 MΩ metal film resistor. By contrast, the current sensing resistor for the switching current measurements was the metal film resistor

located on the chip carrier as described in the previous section. At low temperatures this resistor both increased in resistance by a factor of about 1.3 and also developed minor nonlinear behavior. This nonlinearity was taken into account in the analysis of the escape rate data. Although burdensome, this arrangement was necessary to increase current measurement sensitivity by reducing stray capacitance and the Johnson noise produced by the resistor, as I will discuss in further detail in the next section.

Current-voltage characteristics were digitally recorded on a Hewlett-Packard 7090A x-y measurement system, and data were transferred to a Macintosh IIfx computer using a IEEE-488 interface bus driven by a National Instruments NB-GPIB board. No change in the data was observed when an analog oscilloscope was substituted for the digital x-y recorder.

To obtain switching current distributions, a sawtooth voltage ramp at frequencies between 5 and 50 Hz was applied so that the device was certain to switch to the 1-state on the positive-going portion of the cycle and retrap in the 0-state on the return. The current output was connected to a battery-powered A/D converter located within the screened room which was triggered by the voltage output signal when the device switched from the zero voltage 0-state to the 1-state, with the trigger level adjusted to as small a value as possible such that the noise in the voltage signal would not trip the circuit. The digitized signal was sent via fiber optic cables to the computer to ensure that the computer was electrically isolated from the circuit. These electronics were the same as those used for previous MQT experiments, except for some minor modifications I made which were necessary to interface the existing electronics to the Macintosh computer which replaced the antiquated original PDP-LSI-11 computer.

In addition to the 4K RC filters described above, in several instances I tried other filters to test for noise effects. These included microwave frequency filters at the mixing chamber constructed in a similar manner to those used in the MQT experiments [5], and

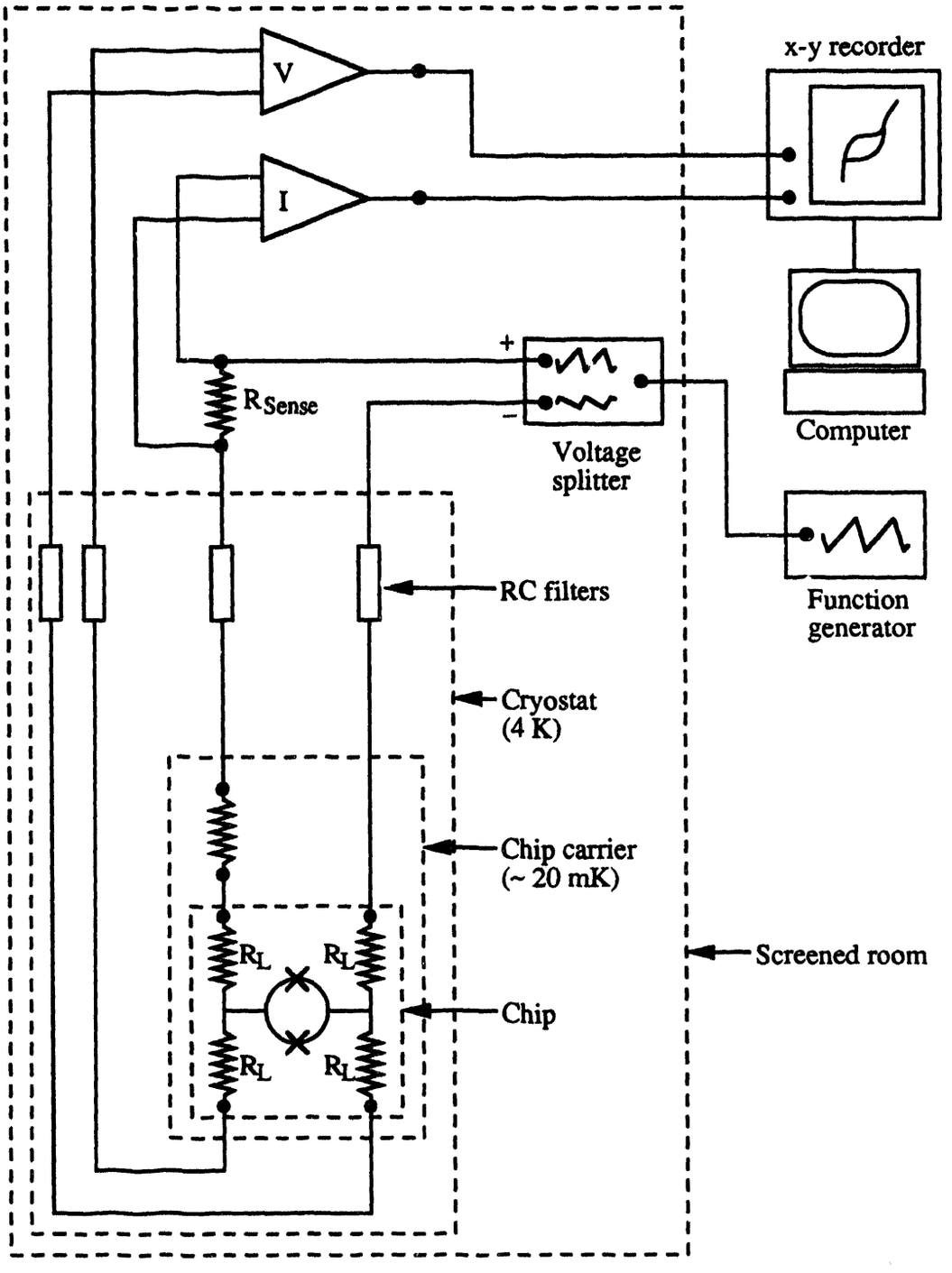

FIGURE 5-5. Schematic diagram of circuit for performing measurements of current-voltage characteristics.

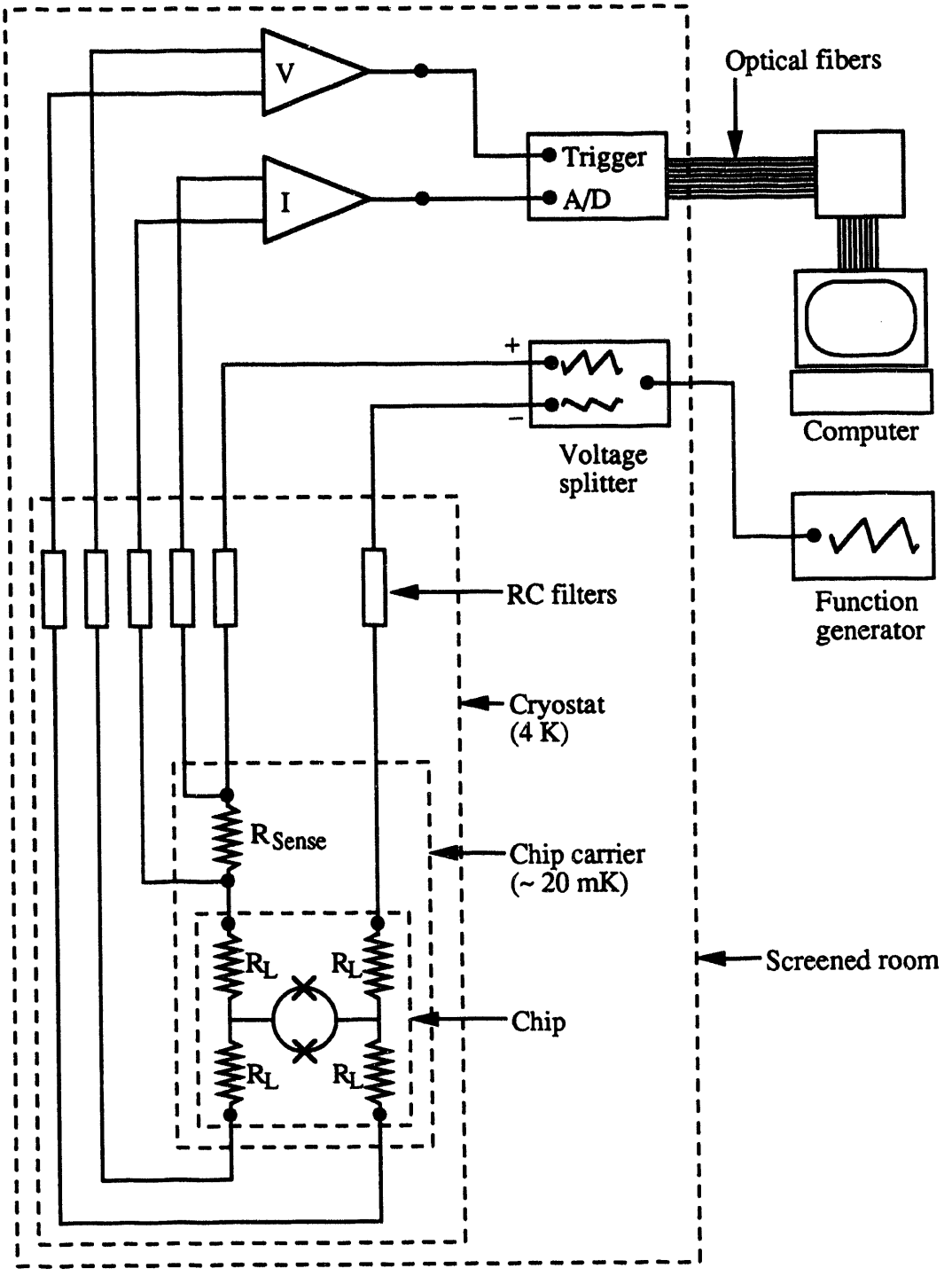

FIGURE 5-6. Schematic diagram of circuit for performing measurements of the switching current.

RF filters used at room temperature at the top of the cryostat. No change in device behavior was ever noted in these tests.

5.4 Noise Considerations for an Escape Rate Measurement

Measuring the escape rate as a function of current is a process which is sensitive to noise over a wide range of time scales, from the time it takes to accumulate a histogram (which is on the order of one hour), to times up to the lifetime of the zero-voltage state. In this section I will explore some of the sources of the noise associated with this measurement, and estimate the current resolution I obtained with my setup.

Ideally, the measurement is performed by increasing the bias current linearly in time. As the voltage V across the device switches in value from zero to the gap voltage V_{gap}, the amplified output voltage GV (G is the gain of the amplifier) is compared to an external reference voltage V_{trig}. The measurement of the current by the A/D circuit is triggered when GV reaches the value V_{trig}. This ideal situation is shown schematically in Fig. 5-7 (a). A more realistic description is shown in Fig. 5-7 (b) which illustrates the following points: Not only is the bias current noisy, the current measured by the resistor R_{sense} may differ from the current which actually passes through the device because of the capacitive loading from the line connected between the current sense resistor and the device. The voltage actually observed is rolled off at the characteristic frequency $1/R_L C_W$, where R_L is the thin-film lead resistance, and C_W is the cryostat lead capacitance. This voltage signal is also noisy, containing both high frequency noise and low frequency drift. The trigger reference voltage itself is also noisy. Because of the finite $R_L C_W$ charging time, there is a time delay Δt between the time the junction switches and the time the output voltage reaches the value V_{trig}. In this time, the current bias continues to increase and fluctuates, so the current measured when the A/D converter circuit is triggered is different from the value of bias current at the time the device actually switched. Some of these effects produce constant offsets which can be taken into account through additional calibration procedures. However, some act to reduce the current resolution of the measurement.

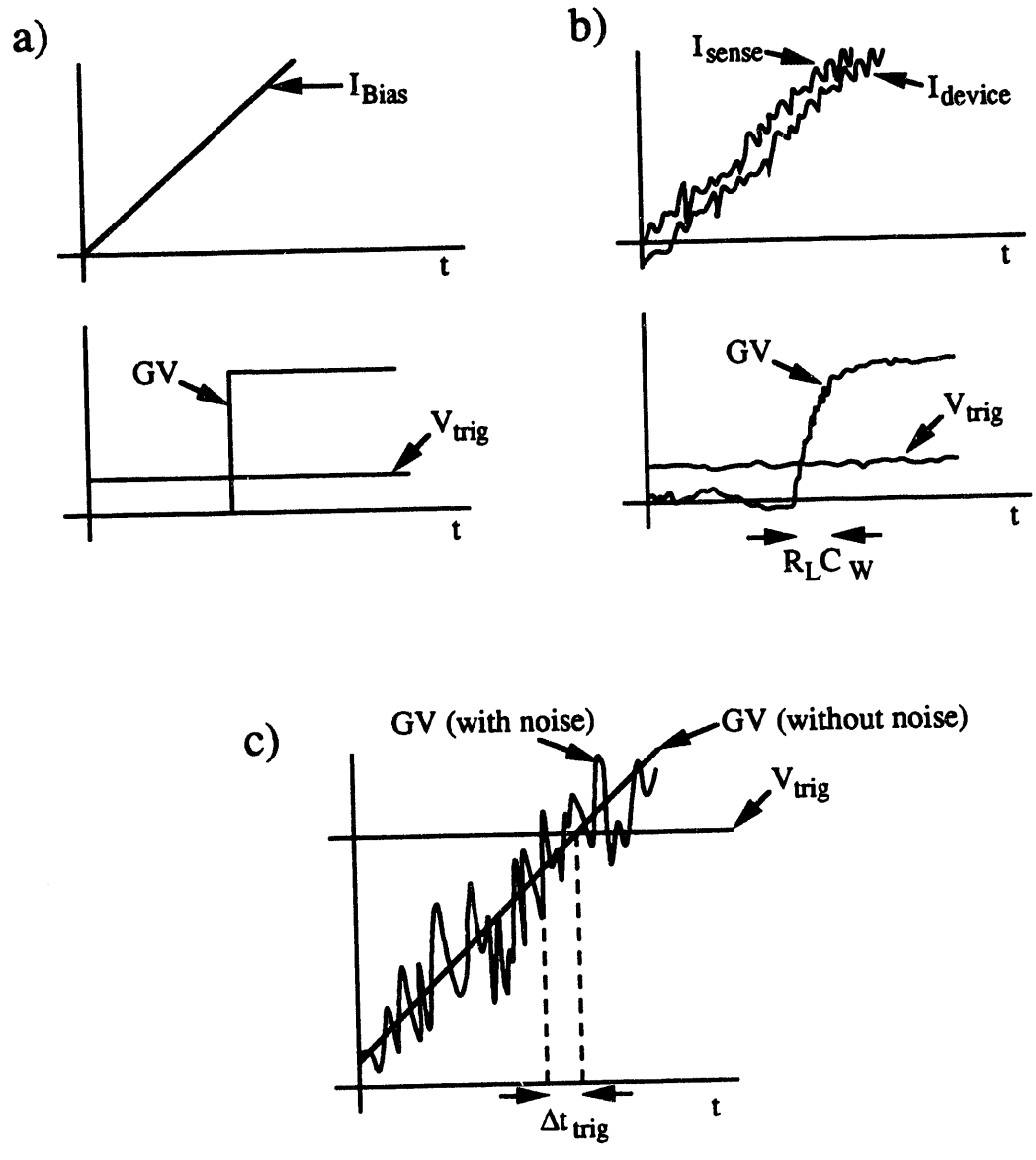

FIGURE 5-7. Schematic diagram of current and voltage signals involved in a switching current measurement. (a) Ideal, noise-free signals. Top, current bias I_{Bias} is a linear ramp. Bottom, output voltage GV switches instantaneously, crossing the trigger reference voltage V_{trig}. (b) Realistic signals. Top, currents through sensing resistor (I_{sense}) and through device (I_{device}) are noisy and may differ. Bottom, output voltage GV is noisy and has the characteristic charging time $R_L C_W$. The trigger reference voltage V_{trig} is also noisy. (c) Zero crossing problem. The noisy voltage output signal tends to trigger a time Δt_{trig} before the noise-free signal would.

The $R_L C_W$ product for my setup was about 8×10^{-4} s. Although a large time constant contributes to error in the current measurement, this rolloff was unavoidable since the thin film lead resistances of about 750 kΩ were required, and it would be difficult to substantially reduce the approximately 1 nF capacitance of each cryostat wire. (The capacitance C_W might be reduced by the use of JFET amplifiers located as near the device as possible (probably at the 1 K pot) and by using guarded lead wires which are kept as short as possible. These steps could reduce the capacitance of each lead to 10 to 30 pF. However, I did not undertake these steps.)

I chose the current-sensing resistance R_{sense} to be 1 MΩ because it is nearly the optimal value based on the noise characteristics of the PAR 113 amplifier. When this resistor is cooled to 20 mK, the RMS voltage fluctuation of this resistor has a spectral density of about 1 $nV/Hz^{-1/2}$, about an order of magnitude smaller than the input noise spectral density of the PAR 113 which is about 10 $nV/Hz^{-1/2}$. I minimized the contribution of the amplifier noise by choosing a 3 kHz bandwidth, which was only slightly wider than the bandwidth of the measuring circuit. The resulting amplifier noise fluctuations corresponded to about 0.5 pA RMS. I found the low frequency drift of the PAR 113 to be about 40 μV (referred to the input) over a time period of an hour, which translates to 4 pA of drift. In order to minimize the difference between the current passing through the sensing resistor and the current passing through the SQUID, I placed the sensing resistor on the chip carrier close to the device. In this configuration, external current noise such as that produced by microphonics in the cryostat leads should also be rolled off at $1/R_L C_W$. If the trigger delay Δt is chosen so that $\Delta t << R_L C_W$, then these currents should be correlated. In this limit the trigger delay is given approximately by $\Delta t = R_L C_W V_{trig}/G V_{gap}$. The delay Δt can be minimized by choosing V_{trig} as close to zero voltage as possible without allowing the fluctuations of the amplified voltage output to trigger the A/D converter, and this noise of the voltage output can be reduced by choosing the voltage amplifier bandwidth as near as $1/R_L C_W$ as possible without

contributing further to the existing rolloff. I chose 3 kHz, which resulted in RMS voltage fluctuations of about 0.5 μV, referred to the amplifier input. With this choice of bandwidth, the output voltage was dominated by low frequency noise and drift, which was about 40 μV over an hour, also referred to the input. I used the maximum gain of $G = 10^4$ to minimize the effects of a noisy trigger reference voltage and additional interference picked up by the circuit after amplification. The minimum trigger voltages I was able to use typically ranged from 50 mV to 100 mV, giving a trigger delay Δt on the order of 10 μs. This was much less than the characteristic $R_L C_W$ time.

One should note that drift in the voltage output signal not only increases Δt, but also directly causes uncertainty in the switching current measurement. A drift of 40 μV over an hour corresponds to a variation δt in Δt of about $\delta t = 10$ μs. Assuming a typical ramp rate of 2 μA/s (which corresponds to a 100 nA sweep at 20 Hz), this drift of the voltage amplifier creates a loss in resolution of about 20 pA. This is an order of magnitude larger than the contributions of the other sources to the uncertainty in the current. To avoid this drift, one might consider filtering the voltage signal with a simple high-pass filter having a low frequency rolloff. While this approach removes the drift, it actually creates an additional error stemming from the retrapping event which occurred in the previous cycle. Because the retrapping is stochastic it precedes the escape event by a length of time which varies from cycle to cycle. Because this is the time period over which the filter capacitance discharges following the retrapping event (with a characteristic time equal to the inverse of the rolloff frequency of the filter), this results in the variation of the value of the voltage signal at the time of the escape event, and thus in the time between the escape event and the triggering of the A/D converter. A more complex scheme for removing the drift of the voltage signal involving active elements could be used, but I did not pursue this.

One additional source of error in the switching current measurement arises because the high frequency noise of the voltage signal causes a triggering error. This

type of situation is studied in the literature and is sometimes called the "zero-crossing problem" [68]. As the amplified output voltage GV, which has noise fluctuations of root mean square amplitude δV_{RMS}, increases toward the trigger threshold, positive fluctuations on the average will trigger the current measurement at a time $\Delta t_{pretrig}$ before the equivalent noise-free signal would. These fluctuations also create an uncertainty $\delta t_{pretrig}$ in the time at which the triggering occurred. This is illustrated in Fig. 5-7 (c). The values of $\Delta t_{pretrig}$ and $\delta t_{pretrig}$ are roughly equal for the case of Gaussian noise and have the value $\Delta t_{pretrig} = \delta t_{pretrig} = \delta V_{RMS} R_L C_W/(G V_{gap})$. This time was about 1 μs in my setup. Again assuming a 2 μA/s current ramping rate, this created an approximately 2 pA loss in resolution.

Note that in each of the cases where noise was associated with the voltage signal an uncertainty in trigger time produced an uncertainty in the current which was proportional to the current ramp rate. Errors of this nature thus will tend to scale with the critical current of the device because the ramping rate scales with the critical current, because typically the repetition rate is kept roughly the same order of magnitude.

In conclusion, the drift of the voltage amplifier caused the greatest loss of current resolution in the switching current measurements I performed. The resolution I obtained was approximately 20 pA. Because the recorded switching currents for device A ranged over values of about 10 to 20 nA, this corresponded to a resolution of about one part in 10^3. This was about one-fourth the resolution of the 12-bit A/D converter, but I typically combined channels of the A/D converter in groups, or bins, of 16 channels in order to provide enough events in each bin for good statistics, that is, to reduce scatter in the resulting escape rate distributions. Thus, this setup provided adequate resolution for my purposes.

CHAPTER 6

Results, Analysis, and Discussion

During the course of this research, about two dozen devices of the hundreds started as e-beam exposures were actually run on the dilution refrigerator. Of these, I will report on various measurements performed on three different devices as they are relevant to this chapter's analysis. Parameters for these devices are given in Table 6-1. Many were preliminary or diagnostic and for this reason the devices cover a range of parameters and are not necessarily of the ideal design described in the previous chapters. The benefit of this is, of course, the resulting wide variety of behavior in current-voltage characteristics and switching dynamics. This afforded a great deal of insight into understanding the processes which are important in determining the behavior of devices in this parameter range.

In this chapter I show that in spite of this variety in the devices measured, the most important common thread is that their behavior can be described by a general model in which the effective temperature of the device is not determined by the mixing chamber temperature, but rather by the power being dissipated in the thin-film leads of the device. I will present evidence that this temperature is much greater than the typical mixing chamber temperature of 20mK, and is in fact several hundreds of millikelvin for bias

Device	A	B	C
R_N	1.39 kΩ	987 Ω	1.80 kΩ
$2\Delta/e$	400 μV	375 μV	379 μV
I_c^{max}	226 nA	298 nA	165 nA
C	37 fF	15 fF	20 fF
Lead Material	SiCr	NiCr	NiCr
Lead Resistance	770 kΩ	8 kΩ	13.3 kΩ
Lead length	27 μm	30 μm	62 μm
Lead width	150 nm	220 nm	220 nm
Lead thickness	6.1 nm	21 nm	20 nm

TABLE 6-1. Parameters of devices A through C.

currents where switching events typically occur. I believe that only the electron gas is at this high temperature, while the phonons remain at a temperature near that of the mixing chamber. This happens because of an energy flow bottleneck which occurs at the interaction between the electrons and phonons at low temperatures. This effect, which was studied by Fred Wellstood in connection with heating in the normal metal shunts of a DC SQUID operated at low temperatures [69, 70], is referred to as the "hot electron effect", and was previously sudied in thin film systems by Roukes et al. [71]. During the preparation of this thesis , I became aware of the recent results of Kautz et al. [72], who found self-heating in a Coulomb-blockade electrometer and successfully explained their data using the same model. All these results indicate a fact of universal importance: One must be keenly aware of hot-electron effects when operating thin-film devices at millikelvin temperatures.

6.1 General Features Observed in the Devices

In order to be specific, I will focus on device A in this section, although many of the features noted were common to all devices tested. A current-voltage characteristic of device A is shown in Fig. 6-1, which illustrates some of the typical features of all the devices measured. Here the temperature of the mixing chamber, denoted by T_{mix}, was $T_{mix} = 40$ mK and the applied magnetic field was such that the critical current was at a maximum, which corresponds to $\eta = 0$ in Eq. (4-17). The quasiparticle branch of the current-voltage characteristic was well pronounced, and had a gap voltage $2\Delta/e$ of about 400 μV. Gap voltages typically ranged from 370 μV to 400 μV in the devices measured. These values are consistent with gap voltages of Al-Al_2O_3-Al tunnel junctions reported in the literature [73]. The normal resistance R_N of this particular device was 1.39 kΩ as measured by the slope of the I-V at voltages approximately 3 to 5 times the gap voltage. Unfortunately this resistance included in series the normal resistance of the parasitic junction formed during the fabrication of the device. However, because of the large ratio of this junction's area to the total area of the SQUID junctions, this resistance is assumed to be small. A small "glitch" can be seen in the quasiparticle branch which I attribute to the switching of the parasitic junction. This fortunately occured at values of bias current higher than those of interest in the experiment, again because of the relative difference in junction areas. Using the measured gap voltage and normal resistance, I found the predicted maximum thermodynamic critical current $I_c^{max} = \pi\Delta/2eR_N$ for this device was 226 nA. However, the value of bias current for which switching events typically occurred during a current-ramp was about 13 nA, which corresponded to a reduced current of $s = 0.06$. Although device A in particular demonstrated switching at very low values of s, all devices investigated switched at values of $s << 1$, with the greatest demonstrated by device B with $s \approx 0.35$.

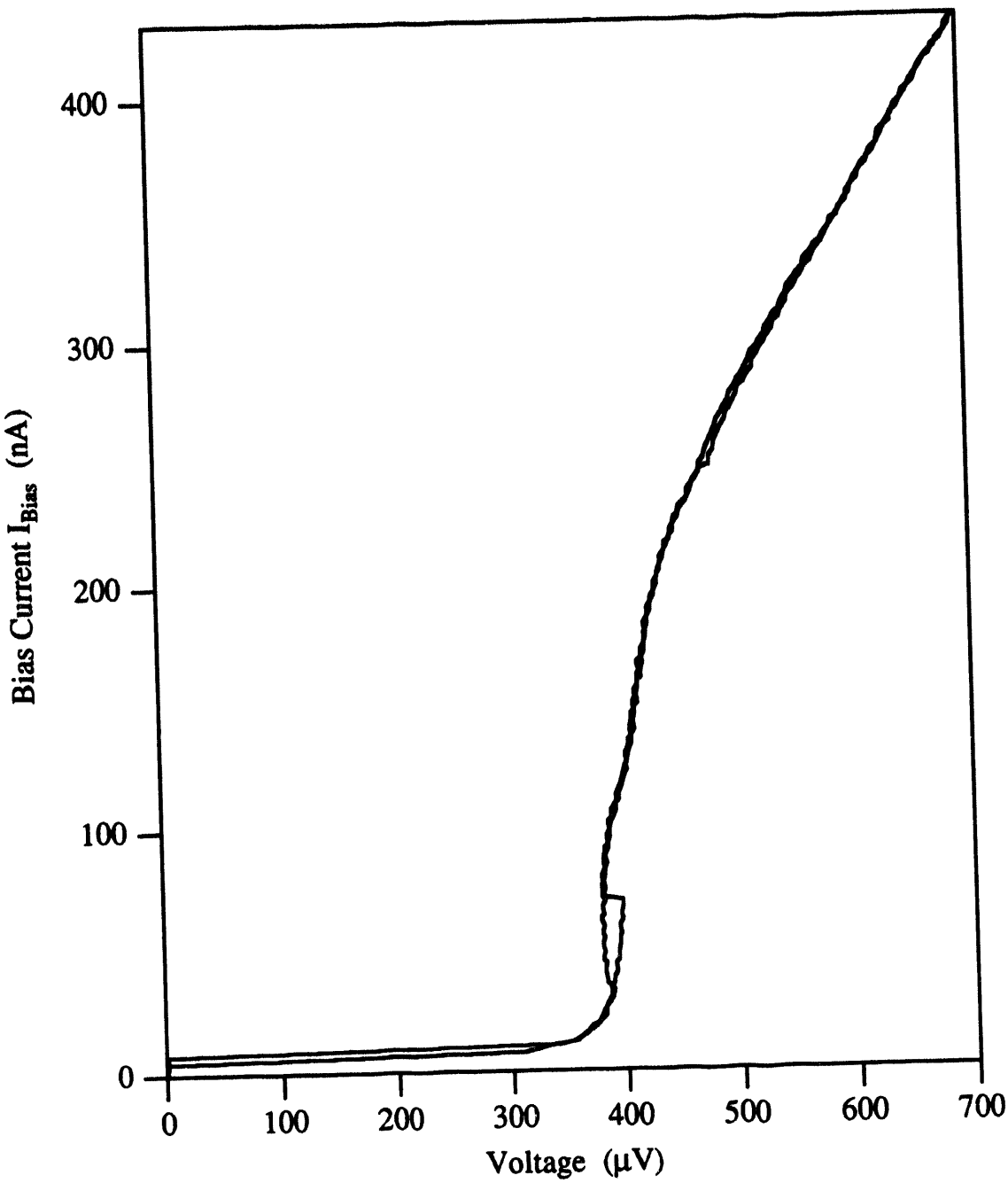

FIGURE 6-1. Current-voltage characteristic of device A taken at $T_{mix} = 40$ mK. The critical current was at a modulation maximum ($\eta = 0$), and the current ramping rate for this sweep was about ± 60 nA/s.

Device A showed a modulation of the switching current which was periodic as a function of the applied magnetic field. This modulation, characteristic of a DC SQUID, was seen in all devices reported here. Because the switching to the 1-state occured over a wide range of bias current values when modulated to the maximum critical current ($\eta = 0$), the period was best measured by finding the modulation minima ($\eta = 1$), where the switching occurred over a narrow range. The values of η could then be determined by assuming a linear variation with the magnet current. The period of modulation for all devices was found to be consistent with the estimated area of the SQUID loop. The symmetry of the two junctions of SQUID A was tested by taking time-averaged current-voltage characteristics at applied fields of $B_1 \pm 0.18\Delta B$, where B_1 was the field corresponding to a modulation minimum and ΔB was the period of modulation. These current-voltage characteristics were found to be identical to within limits set by the uncertainty in finding B_1, which was approximately $\pm 0.004\ \Delta B$. The value 0.18 was chosen because it was near the point where the switching currents varied the most as the applied magnetic field was varied, and thus gave this test the greatest possible sensitivity. Another indication of both the symmetry of the junctions and the low inductance of device A was the fact that the switching currents at $\eta = 1$ were found to be less than 0.6 % of those measured at $\eta = 0$. This degree of modulation was typical of all the devices measured and it implies that the model described in Section 4.2 is reasonably accurate for these devices.

The resistances of the NiCr thin film leads used on devices B through E showed virtually no change as the temperature was varied from room temperature to millikevin temperatures. The SiCr leads used on device A showed only a small increase in resistance upon cooling to millikelvin temperatures. In fact, the temperature dependence of the SiCr was very consistent from lead to lead. Although room temperature resistances of the four leads ranged from 480.3 kΩ to 572.2 kΩ, the resistance ratios upon cooling from room temperature to 77 K were all equal to 1.125 to within a tenth of a percent.

Similarly, the resistance ratios for the leads upon cooling from room temperature to 42 mK were all equal to 1.275 to within three tenths of a percent. I interpret this uniform fractional increase in the resistances as an indication that the SiCr alloy deposited was very homogeneous, and the variation in resistance among leads was caused by differences in dimensions only. Note also that this behavior indicates the alloy behaves as a metal and not a semiconductor.

6.2 Evidence for Joule Heating of the Leads

Current-voltage characteristics for device A taken with several values of applied magnetic field are shown with the current axis expanded in Fig. 6-2. The mixing chamber temperature was 19 mK. Each sweep shown in Fig. 6-2 (a) was taken with a current ramp of 2.5 nA/s. Here one can see that as the bias current was increased, the device did not make a single switch to the 1-state, but rather made several jumps back and forth between the 0 and 1-state. Similarly, when the bias current was decreased, several voltage jumps were made in the same range of bias currents before the device stabilized in the 0-state. The number of jumps observed during a sweep depended on the time period over which the sweep was taken, with a longer sweep time resulting in more jumps. In fact, I found that for each value of critical current there was a range of values of DC bias current for which the device would switch between the 0 and 1-state, indicating that the system was in a bi-stable configuration. As the critical current was reduced, the number of jumps in a given time period increased, indicating that the characteristic time of switching was decreasing.

This bi-stable behavior was at first perplexing. As discussed in earlier chapters, this device was designed to have a very high shunt impedance to reduce the damping. In a high-Q device such as this, a range of bias currents exists for which both the 0 and 1 states are stable at low temperatures because the energy barriers Δu and Δw for transitions between these states, defined in Section 3-1, are both large. This results in a hysteretic current-voltage characteristic. However, if there is enough thermal energy available, these barriers may be surmounted, and the states become unstable. In the RSJ model, this thermal energy is included in the dynamics of the model as Nyquist current noise from the shunt, as was discussed in Chapter 3. At temperatures of 19 mK, however, this device should definitely be in the limit where it should have a hysteretic current-voltage characteristic, as discussed in Section 4-3.

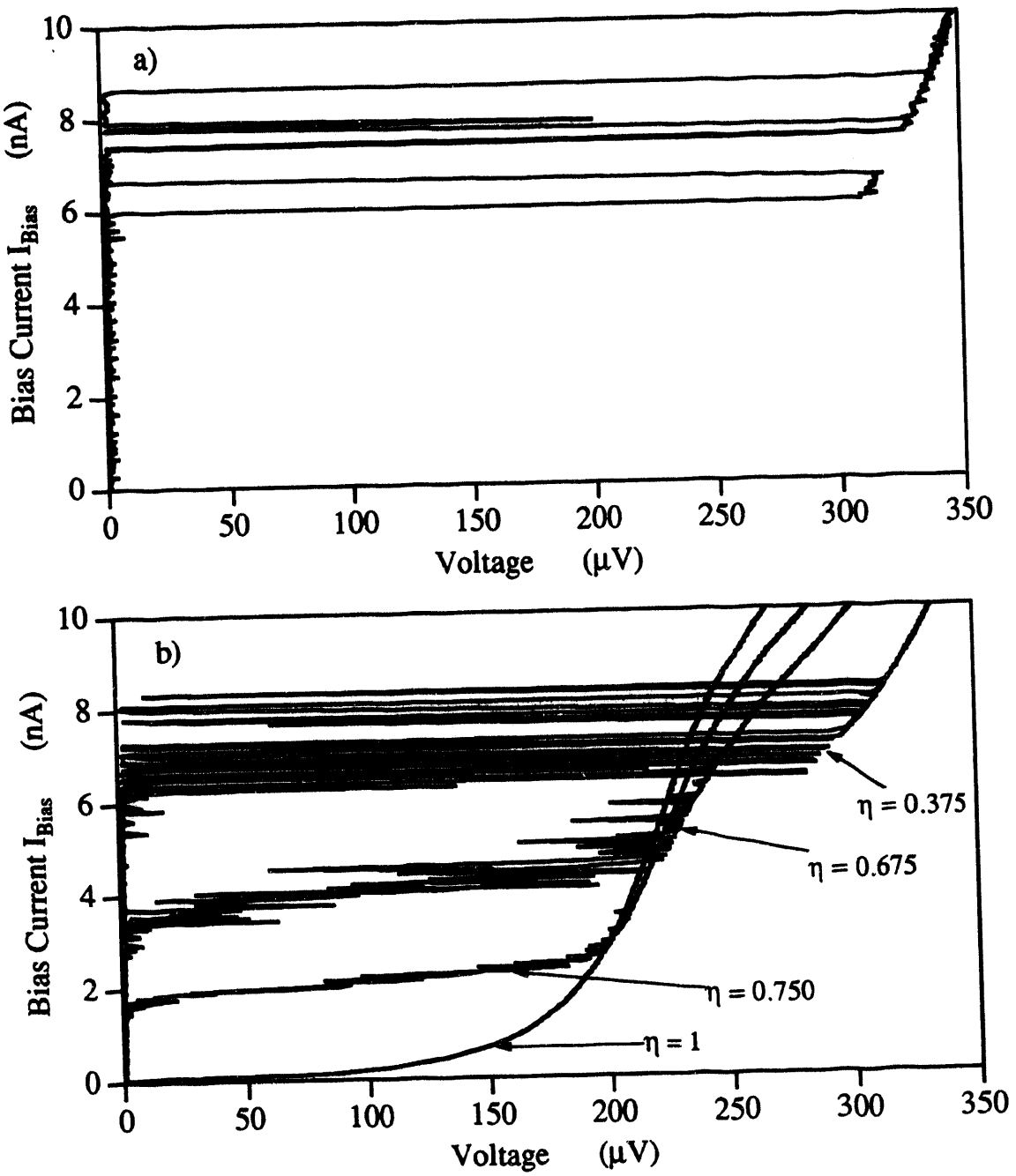

FIGURE 6-2. Current-voltage characteristics of device A taken at T_{mix} = 19 mK for several values of applied magnetic field. (a) $\eta = 0$. (b) $\eta = 0.375$, 0.675, 0.750, and 1.00.

Because external noise sources could mimic the thermal noise in supplying the extra energy required to surmount the barriers, I took steps to eliminate as many of the potential external noise sources as possible. All computers and 60 Hz line-powered electronics except for an analog oscilloscope were shut off, and all power to the screened room was disconnected and the door was shut. Thermometry and heating wires were disconnected at the top of the cryostat. Refrigerator pumps were stopped to eliminate any vibration they might cause. The measuring circuit, containing one battery-powered amplifier for sensing voltage, was driven by a simple battery and resistor source, and RF filters were inserted into the lead lines at the top of the cryostat. Both the refrigerator and the amplifier were shielded with mu metal. After all these precautions had been taken, no change in the switching behavior was observed. Thus I was led to conclude that the switching behavior was intrinsic to the device.

These results lead me to examine the transition from a hysteretic behavior to a bi-stable switching behavior using the RSJ model. By examining Eqs. (3-4) and (3-8), which give the characteristic times t_+ and t_1 for the thermally activated escape and retrap processes, I note that the arguments of the dominant exponential term in each of these expressions are of the same form, namely, a reduced energy barrier (Δu or Δw) of magnitude which depends on the bias current divided by the reduced temperature $\Gamma = 2ek_BT/hI_c$. Although these times might be extremely long for low temperatures or high critical currents, there is a bias current for which the characteristic times t_+ and t_1 are equal. Following previous authors [26, 74] I define this reduced current as s_e, which is found by setting Δu and Δw equal. Referring back to Fig. 3-1, the current s_e is at the intersection of the curve $\Delta u(s)$ and the curve $\Delta w(s)$, which depends on Q. An approximate expression for s_e is given by [26]

$$s_e = (2\pi + 4)/Q + (2 + \pi)/Q^2 \ . \qquad (6\text{-}1)$$

Now imagine a junction biased at s_e. As the reduced temperature Γ is then increased, either by an increase in the actual temperature T or a decrease in critical current I_c, both characteristic times t_+ and t_1 decrease until a point is reached where the 0 and 1 states both become unstable because of thermal activation. This is roughly where hysteretic behavior crosses over to the bi-stable behavior with a characteristic switch time t_{switch} defined by $t_+ = t_1 = t_{switch}$. A further increase in Γ results in further reduction in t_{switch}. Since device A shows just such a reduction in switching time as I_c is reduced by the application of a magnetic field, I want to get a rough estimate of how I might expect t_{switch} to vary with I_c. I found that the bi-stable switching behavior observed in device A would occur with a duty cycle of 50% (that is, the total time spent in the 0-state was equal to the total time spent in the 1-state) when the device was biased at a reduced current of about $s = 0.035$. I will take this to be the value of s_e. Noting that $\Delta u(s)$ can be approximated by $\Delta u = 2 - \pi s$ to better than 0.1% for $s = 0.035$ and that in Eqn. (6-1) for s_e, Q varies weakly with I_c (as discussed in Section 4-4, Q varies as $I_c^{1/2}$ in the ohmic shunt limit and $I_c^{1/4}$ in the transmission line limit), I will approximate $\Delta u(s)$ by the constant $\Delta u(s_e) = 1.89$. Finally, assuming the variation of I_c with the application of a magnetic field follows the expression given in Eq. (4-17), I expect to find that the natural logarithm of t_{switch} varies roughly linearly with $\cos(\pi\eta/2)$ with slope $1.89\,\hbar I_c^{max}/2ek_BT$.

In order to test this model, detailed measurements of the bi-stable switching were carried out. The device was biased with a DC current chosen so that the duty cycle was nearly 50%. A time trace for the voltage across the junction taken under the condition $\eta = 0$ is shown in Fig. 6-3 (a). It had the appearance of a random telegraph signal (RTS), that is to say, jumps of magnitude ΔV (here ΔV corresponds to the gap voltage) were made randomly at characteristic times t_+ and t_1 between the 1-state and 0-state. The noise power spectrum of such a signal is Lorentzian, given by

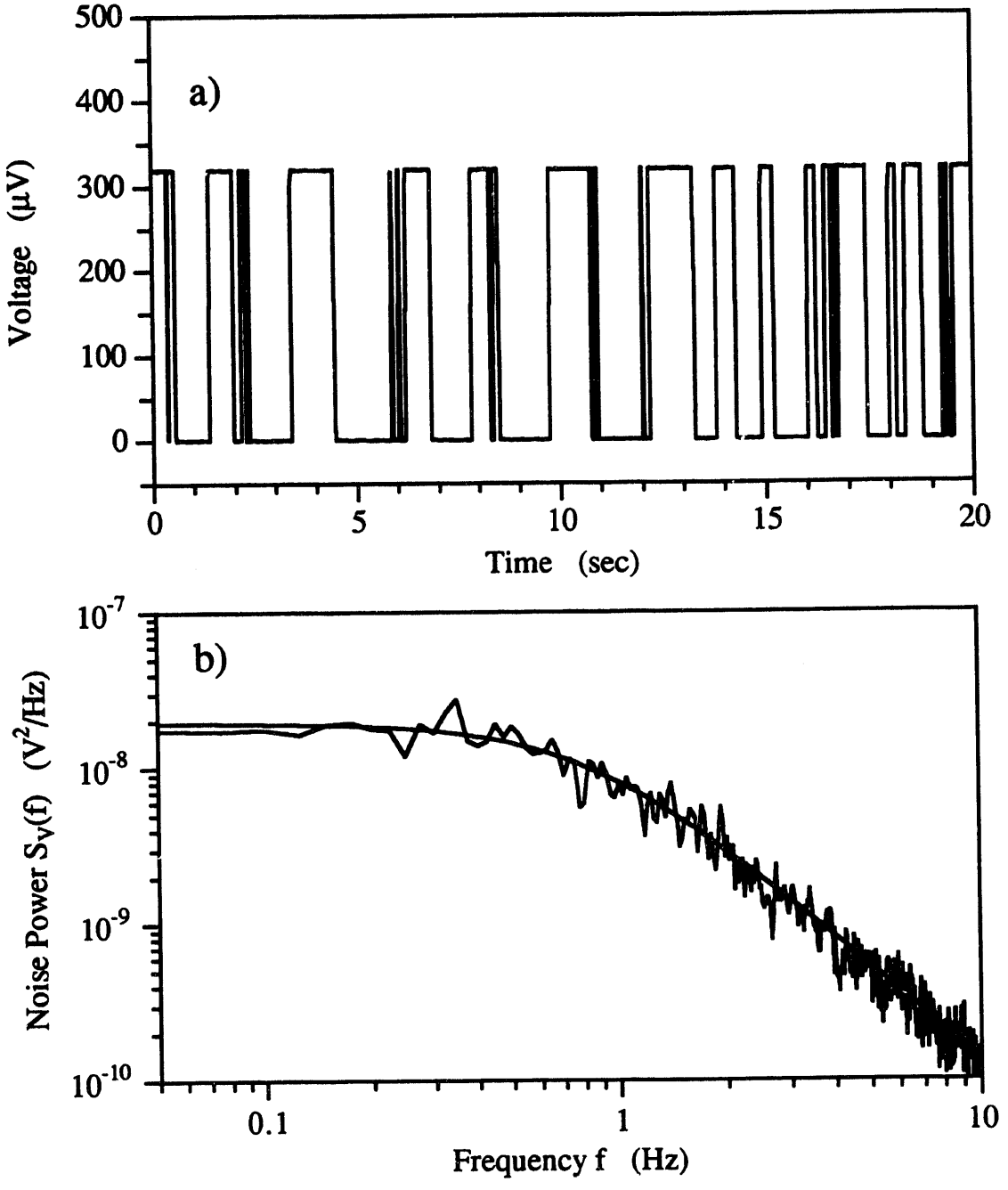

FIGURE 6-3. (a) Voltage across device A measured as a function of time with a DC current bias of 7.2 nA, at the critical current maximum $\eta = 0$. (b) Noise power spectrum for the signal described in (a). The smooth line is a fit to this spectrum using Eq. (6-2) for a Lorentzian with $\Delta V = 319\ \mu V$ and $t_+ = t_1 = 0.382$ s.

$$S_V(f) = \frac{4(\Delta V)^2}{(t_+ + t_1)\left[\left(t_+^{-1} + t_1^{-1}\right)^2 + (2\pi f)^2\right]} \quad . \qquad (6\text{-}2)$$

Here f is the frequency. A measurement of the noise power spectrum of this signal revealed that it was in fact Lorentzian. By performing a fit of Eq. (6-2) to this power spectrum and assuming that for duty cycles close to 50% (say within 10%) I could use the approximation $t_+ + t_1 = 2t_{switch}$, I was able to obtain t_{switch}. This measured noise power spectrum is shown in Fig. 6-3 (b) along with a fit using Eq. (6-2) with $\Delta V = 319\ \mu V$ and $t_{switch} = 0.382$ s. Continuing in this manner for several values of applied magnetic field, I was able to obtain t_{switch} as a function of η over the range $\eta = 0$ to 0.44. (For $\eta > 0.44$, the frequency $1/t_{switch}$ was approaching the RC rolloff of the device thin-film leads and stray capacitance of the cryostat wires, resulting in a signal that was no longer a RTS.) The measured values of t_{switch} are plotted on a logarithmic scale versus $\cos(\pi\eta/2)$ in Fig. 6-4. Although there is some curvature at the higher values of η, the general trend is linear over almost two decades. A line fitted to the upper six points, also shown in Fig. 6-4, gives a slope indicating a temperature of T = 0.50 K, assuming $I_c^{max} = 226$ nA.

Because this temperature is so much higher than the mixing chamber temperature of 19 mK, I cannot assume that the temperature T = 0.50 K is an actual temperature in the sense of all macroscopic or even microscopic components of the system being in thermal equilibrium at this temperature. For this reason, I will refer to a temperature inferred from the junction behavior as an "effective temperature" and denote it by T_{eff}. However, I am free to speculate that the high effective temperature is associated with the ohmic heating of the thin film leads connected to the device, and more specifically, to the ohmic heating of the conduction electrons in these leads. I will defer discussion of this topic, and the mechanism by which bias currents of this magnitude might produce temperatures this high, to Section 6-4.

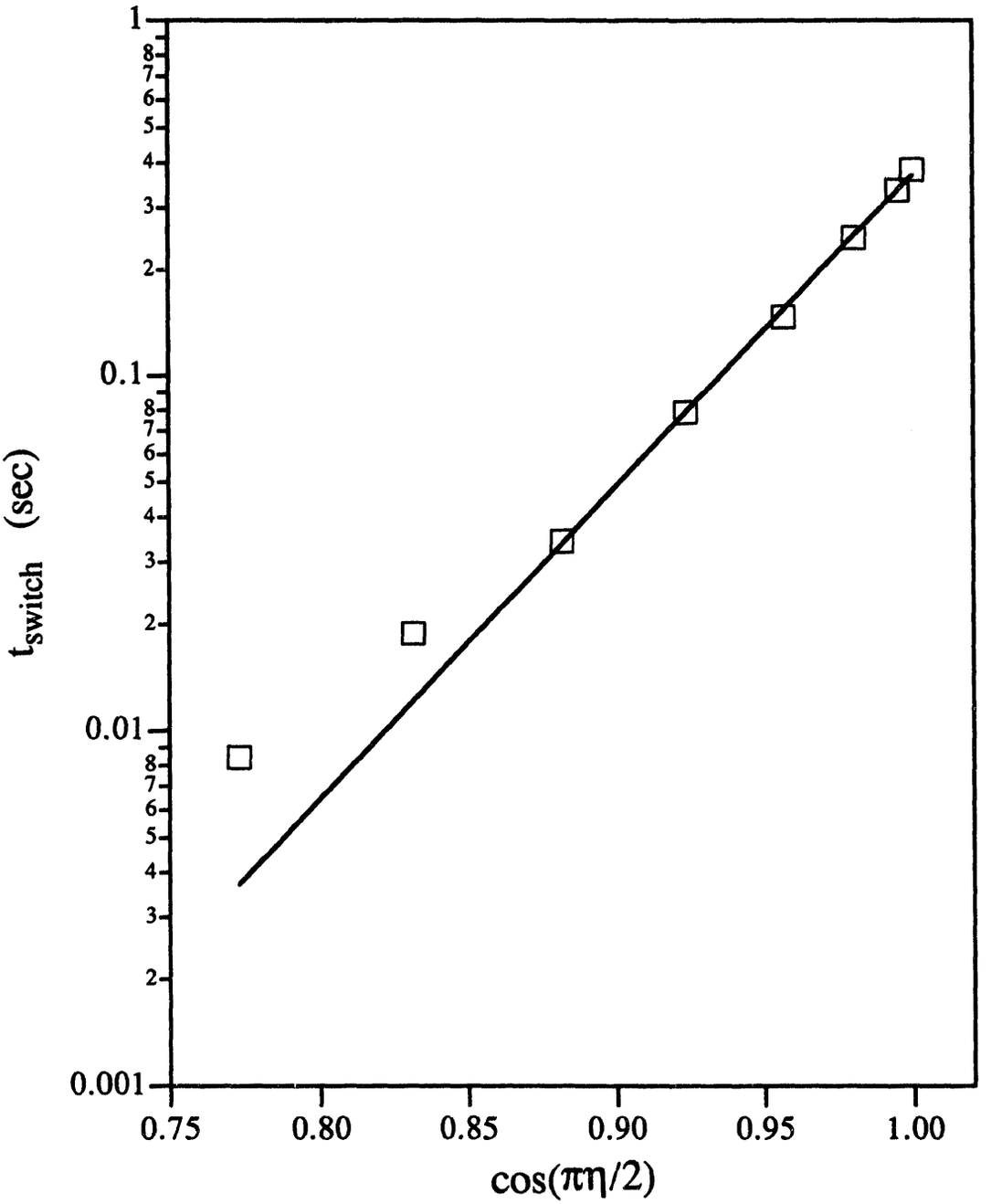

FIGURE 6-4. Characteristic time of switching between the 0 and 1 states observed in device A, plotted versus $\cos(\pi\eta/2)$, the modulation factor for the critical current given by Eq. (4-17). Measured values are shown as symbols. A linear fit to the upper six measured values is shown as a solid line.

In order to make an independent and more direct test of this hypothesis regarding the high temperature of the leads, a measurement technique was attempted based on measuring the Johnson noise produced by the leads of the device. According to the Nyquist theorem, the noise power S_V per unit bandwidth produced by a resistor R at temperature T is given by $S_V = 4k_BTR$. The thin film leads of device A each had a series resistance of about 750 kΩ, so two in series measured about 1.5 MΩ. Thus, at a temperature of T = 0.5 K I expected to the leads to generate RMS voltage fluctuations of spectral density $S_V^{1/2} = 6.4$ nV/Hz$^{1/2}$. By contrast, at T = 20 mK, the noise should only be $S_V^{1/2} = 1.3$ nV/Hz$^{1/2}$. Thus, by measuring the noise both with and without a DC bias current applied, I expected to be able to tell whether the bias current was indeed heating the leads. Unfortunately, because of the limited sensitivity of my amplifier and problems with external noise pickup and microphonics, I was unable to get an accurate measurement of the noise increase. However, the results I obtained were consistent with the hypothesis of lead temperatures of hundreds of millikelvin. A detailed discussion of this particular measurement and this approach in general can be found in Appendix A.

6.3 Further Estimates of the Effective Temperature

In Section 6-2, I showed how the bi-stable switching behavior observed in device A implied a high effective temperature, and obtained an estimate of the temperature using the characteristic rate of switching. Next I would like to study device B, for it allows me to obtain a better quantitative estimate of the effective temperature.

Current-voltage characteristics of device B, taken at T_{mix} = 36 mK for several values of η, are shown in Fig. 6-5. The measured gap voltage was 375 μV, and the normal resistance was R_N = 987 Ω. Device B provides a marked contrast to device A for several reasons. Most notably, the current-voltage characteristics were hysteretic except near critical current minima. This may seem counter-intuitive considering the leads of device B were lower in resistance than the leads of device A by a factor of nearly 100. By presenting greater damping, a lower impedance shunt ordinarily would reduce the amount of hysteresis. In this case, the opposite is true. From an analysis viewpoint, the advantage of having a substantial hysteresis is that it implies the escape and retrapping processes never compete, that is, for a bias current where one process is likely to occur, the reverse process is highly unlikely to occur. A second distinction between devices A and B is their values of reduced switching currents. The measured values of gap voltage and normal resistance imply a critical current of I_c^{max} = 298 nA. When modulated to a critical current maximum, switching events typically occurred at bias current values near 105 nA, corresponding to a reduced current of s = 0.35. This was much greater than the corresponding value s = 0.06 observed in device A.

The escape rate as a function of bias current was measured for several values of applied magnetic field and for temperatures of T_{mix} = 26 mK, 200 mK, and 300 mK. The results for T_{mix} = 26 mK and 300 mK are shown in Fig. 6-6 plotted on a logarithmic scale. Scatter in the data at the ends of an escape rate distribution is caused by poor statistics since these data points represent very few escape events. Several features of the

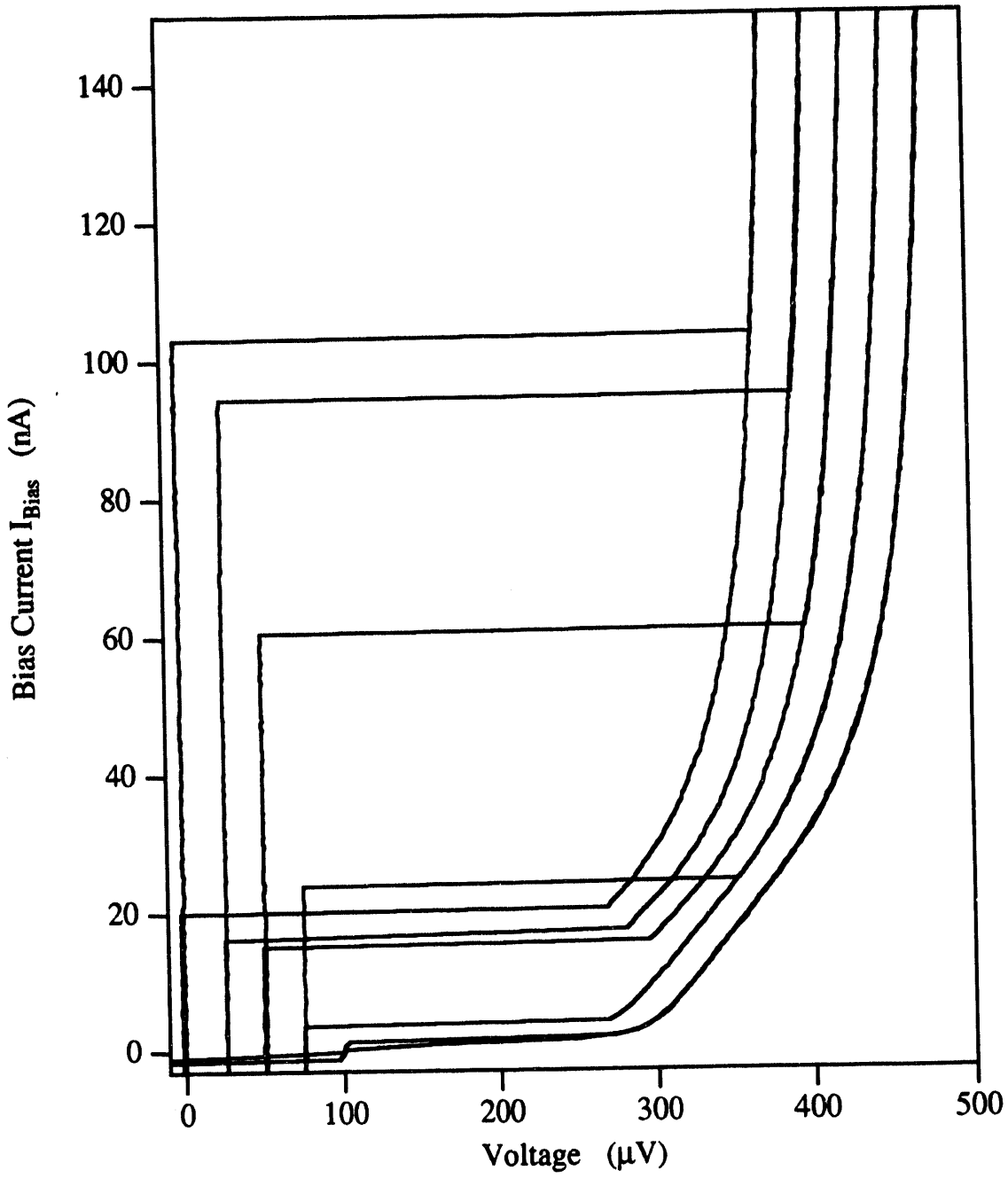

FIGURE 6-5. Current-voltage characteristics of device B taken at T_{mix} = 36 mK for several values of applied magnetic field: η = 0, 0.25, 0.50, 0.75, and 1. For clarity, each characteristic is plotted with an incremental shift of 25 μV as η is increased from 0 to 1.

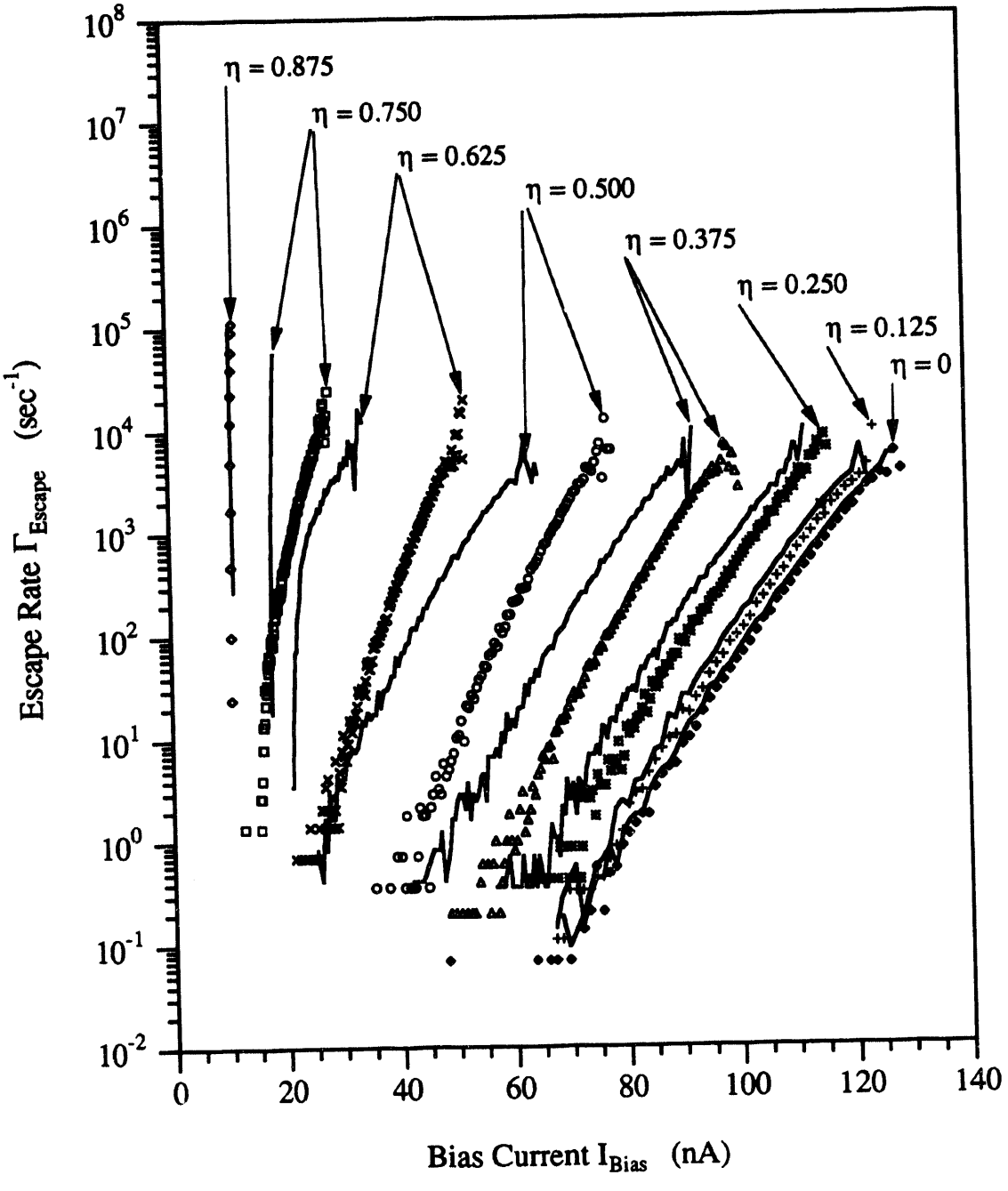

FIGURE 6-6. Device B: Rate of escape to the 1-state as a function of bias current measured for T_{mix} = 26 mK and T_{mix} = 300 mK and eight values of applied magnetic field. T_{mix} = 26 mK data are represented by symbols, while T_{mix} = 300 mK data are shown by solid lines. Each value of η is indicated on the figure with an arrow pointing to the corresponding 26 mK escape rate distribution, and an additional arrow points to the 300 mK distribution when these data are significantly different from the 26 mK data.

data may be noted, and I will focus on the 26 mK data first. The escape rate at any particular value of I_{Bias} increased smoothly as I_c was reduced by the application of a magnetic field. For the case $\eta = 0$, the escape rate curve showed a slight curvature. This curvature tended to increase slightly as η was increased. As η was increased to the value 0.750, a slight downward kink can be seen in the curve at $I_{Bias} = 17$ nA. The curve corresponding to $\eta = 0.875$ was nearly vertical; in this case the kink probably occurred at an escape rate greater than that probed by the measurement. I attribute these kinks in the escape rate curves and the greater slope of the curves to the left of the kinks to retrapping effects. For low values of bias current, the tendency to retrap overwhelms the escape rate, and so full escape events do not occur until the bias current is increased to a point where the retrapping rate drops precipitously, allowing the observed fast onset of switching events. The escape rate curves obtained for $T_{mix} = 200$ mK showed almost no change compared to the 26 mK data. The exception was in the portions of the curves dominated by retrapping, which were found to be translated to slightly higher current values. By contrast, the data taken for $T_{mix} = 300$ mK showed a clear enhancement in escape rate. This increase was small (only a factor of about 1.3) and relatively uniform over the $\eta = 0$ distribution. Overall, the enhancement was increasingly larger for increasingly larger values of η, and for a fixed value of η a larger increase in the escape rate was observed for smaller values of I_{Bias}.

The enhancement of the escape rate for $T_{mix} = 300$ mK is useful because it gives me a chance to test the validity of the Eq. (3-7). Because the escape rate showed a reasonably strong onset of temperature dependence somewhere between 200 mK and 300 mK, it is reasonable for me to assume that the effective temperature was dominated by the refrigerator's temperature of 300 mK. Taking the value $I_c^{max} = 298$ nA obtained from the normal resistance, C = 15 fF from geometrical estimates, and assuming the critical current modulates acording to Eq. (4-17), I obtain the theoretical prediction for the escape rate using Eq. (3-7). I found that, while using $T = T_{mix} = 300$ mK gives

results reasonably within range of the data, a better fit to the data is obtained by using T = 370 mK. This is plotted in Fig. 6-7. It should be noted that the theoretical curves scale remarkably well with the data as η is varied, which supports my assumption for the functional dependance of the critical current on η.

Interpreting this success as an endorsement for the rough validity of Eq. (3-7), I can proceed to attempt to fit the 26 mK data utilizing a single temperature between 26 mK and 370 mK. I find that, not only does using $T = T_{mix} = 26$ mK produce rates well below the measured the escape rate, but in fact no single temperature in that range gives a good qualitative fit to the data. This leads me to hypothesize that the temperature is not constant, but varies with the value of bias current. Thus, I ask conversely, assuming Eq. (3-7) for the escape rate, and scaling I_C with η according to Eq. (4-17) with $I_C^{max} = 298$ nA, what effective temperature $T_{eff}(I_{Bias})$ would produce the data? The result of "working backwards" in this manner, using the escape rate data obtained with device A while the mixing chamber was at the temperatures of 26 mK and 300 mK, is shown in Fig. 6-8. Remarkably, for each mixing chamber temperature, several curves corresponding to a wide range of escape rate values map into roughly a single $T_{eff}(I_{Bias})$ profile. The $T_{eff}(I_{Bias})$ profile corresponding to the 300 mK data is reasonably flat, as I expect because of the dominant constant mixing chamber temperature. Meanwhile, the profile corresponding to the 26 mK data shows a marked increase as the bias current is increased. Note that no fitting parameters were used to obtain this plot. Only the critical current, inferred from direct measurements of the normal resistance, and the capacitance, obtained from geometrical estimates, were used. Although the result is not perfect, it supports the hypothesis that there is an effective temperature which at the lower temperatures depends primarily on the current bias. This analysis also shows why virtually no change in the data was observed when the mixing chamber temperature was raised from 26 mK to 200 mK: the device already was experiencing an effective temperature greater than 200 mK. Finally, one should note that the data originating from

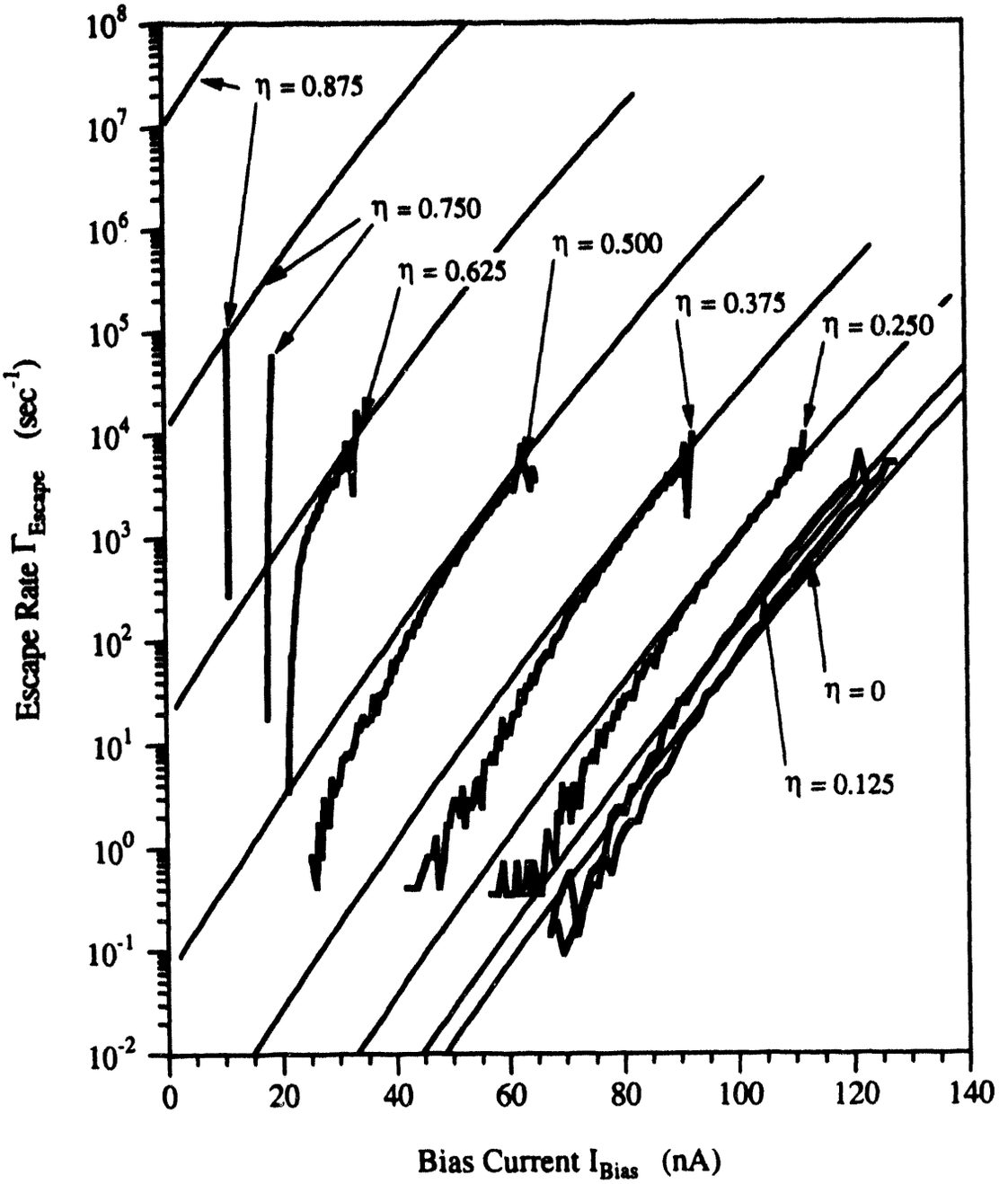

FIGURE 6-7. Escape rate data taken at T_{mix} = 300 mK, identical to those shown in Fig. 6-6, are shown here as heavy lines. Smooth lines are a theoretical prediction using Eq. (3-7) with T = 370 mK.

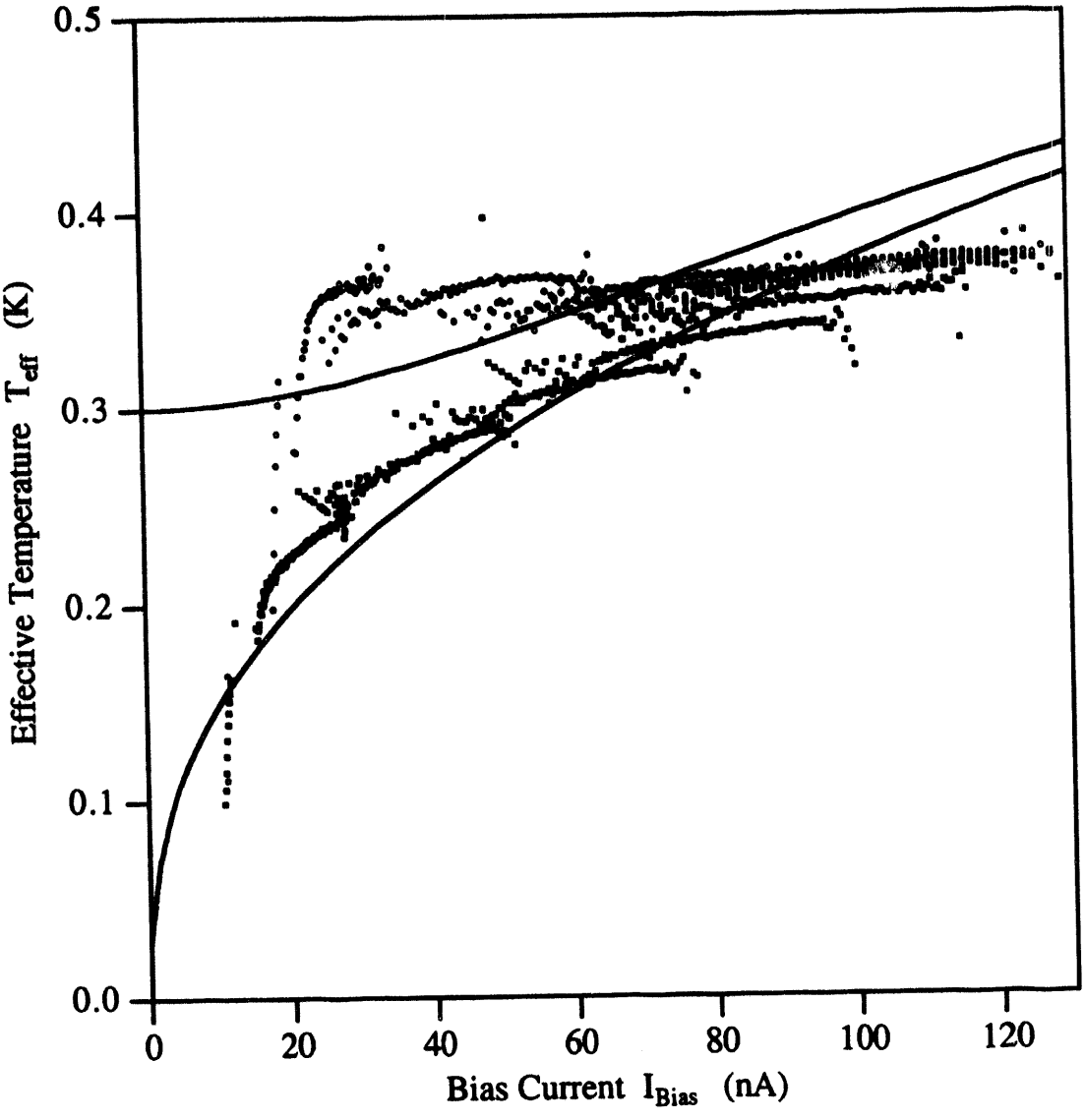

FIGURE 6-8. Effective temperature T_{eff} of device B plotted versus bias current. Data obtained from escape rate measurements are shown as symbols: open circles represent data taken while the mixing chamber was at 300 mK, while solid squares represent data taken while the mixing chamber was at 26 mK. The upper and lower smooth curves are hot electron theory estimates of the effective temperature using phonon temperatures of T_{ph} = 300 mK and T_{ph} = 26 mK, respectively.

portions of the escape rate distributions to the left of the so-called "kinks" deviate strongly from the T_{eff} profile that most of the other data map into. This is consistent with the assumption that these data were dominated by retrapping and should not be governed by Eq. (3-7).

Escape rate measurements were also performed on devices A and C. Although I demonstrated in Section 6-2 that device A showed bistable behavior with a DC or very low frequency current bias, by using sufficiently fast ramp rates and restricting my measurements to low values of η I was able to obtain single-switch type behavior and thus probe the escape rate for bias currents just greater than the bistable region. As with all devices tested, the escape rate distributions were scrutinized for evidence of resonant tunneling. Using I_c = 226 nA and C = 37 fF, I expect to find peaks indicative of resonant tunneling in the current range of 7 nA to 3 nA for η ranging from 0 to 0.875 for the first resonance m = 1. Higher order resonances should occur in a current range which scales with m according to Eq. (2-15). No peaks or unusual features of any sort were observed, in spite of the fact that switching events for this device occurred in a range of bias currents which included the values predicted for resonances.

Effective temperature profiles $T_{eff}(I_{Bias})$ were obtained from the low-temperature escape rate data for devices A and C by applying the same analysis as was applied to device B. These are shown in Fig. 6-9. Excellent results were obtained for device A, with all five escape rate curves for η = 0, 0.125, 0.250, 0.375, and 0.500 falling closely together. The results for device C are not as nice; the curves do not map as neatly into a single $T_{eff}(I_{Bias})$. However, the error is within the uncertainty which arises in determining η. An accurate calibration of η as a function of the magnet current is unavailable as measurements of device C were performed early in the research.

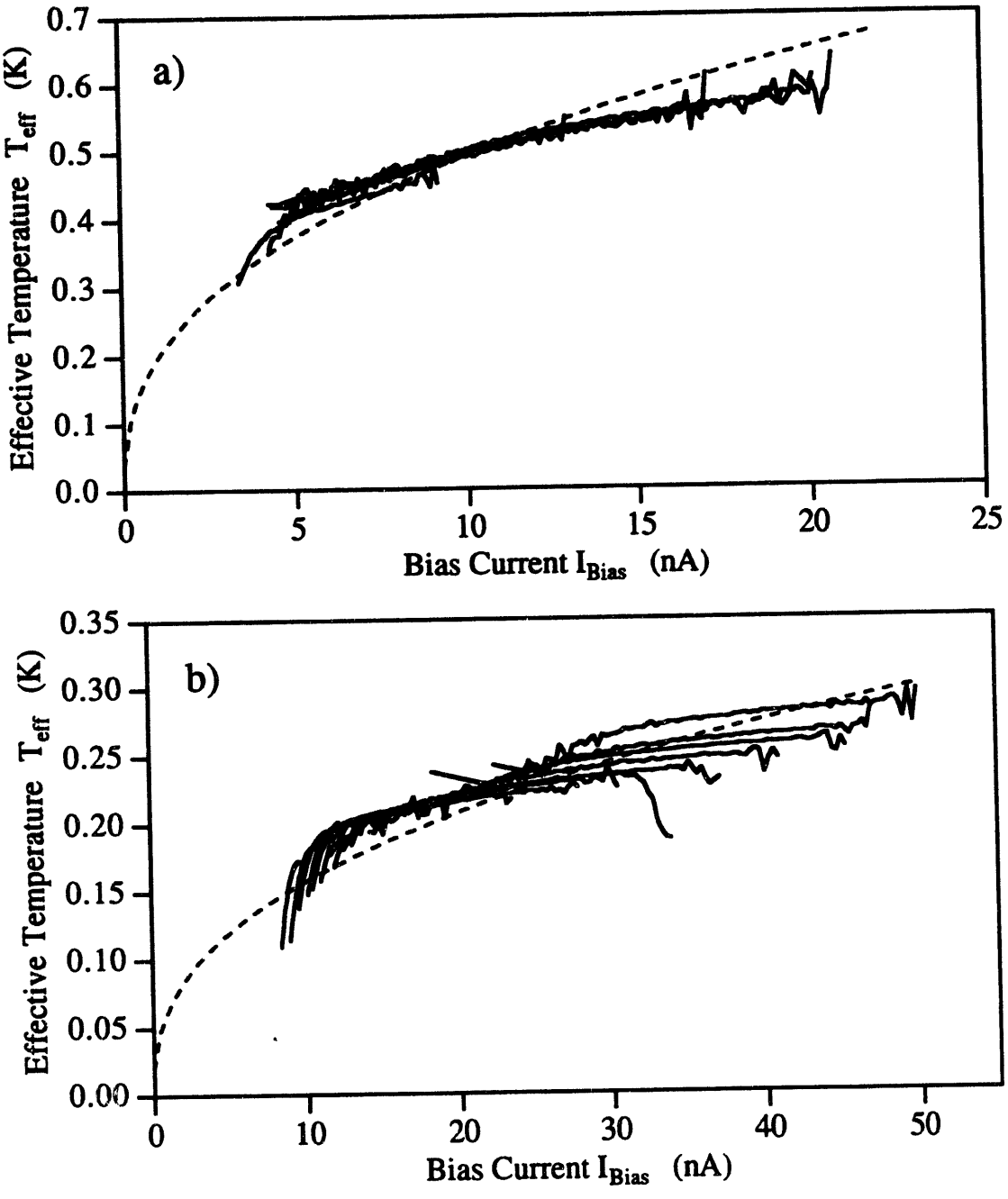

FIGURE 6-9. Effective temperature T_{eff} of devices A and C plotted versus bias current. Data obtained from escape rate measurements are shown as solid lines. (a) Device A, data taken with the mixing chamber at 36 mK. (b) Device C, data taken with the mixing chamber at 19 mK. Smooth dashed curves in (a) and (b) are hot-electron theory estimates of the effective temperature using phonon temperatures equal to the mixing chamber temperatures.

6.4 The Hot Electron Model for Heating

The analysis of the last section revealed that the devices behaved as if they were operating at an effective temperature $T_{eff}(I_{Bias})$ which was dependent on the magnitude of the bias current. The implication is that the devices underwent self-heating. As the current is increased, the observed effective temperature typically rises sharply at first, and then more gradually at higher currents. The type of functional dependence of the temperature on the bias current is somewhat unusual if one considers a simple model for heating: Suppose the power P dissipated by one of the thin film leads carrying the bias current is connected to the mixing chamber of the dilution refigerator, held at temperature T_{mix} = 20 mK, by some constant thermal conductance G. Then I would expect a temperature dependance of $T = T_{mix} + P/G$. The observed effective temperature is certainly not linear in the power, however. One might suggest a particular thermal conductance which is temperature dependent, such as the thermal conductance of the superconducting aluminum. However, by the following argument I can rule out a large class of such models which involve the actual superconducting device getting hot. By examining the results of device A I note that the effective temperature is already 540 mK at a bias current of 20 nA. However, for a bias current of 200 nA which represents an increase in power by a factor of 100, the current-voltage characteristic revealed no apparent reduction in the gap voltage. This implies that in some sense the device remains at a temperature well below aluminum's critical temperature T_c = 1.1 K, and therefore the effective temperature $T_{eff}(I_{Bias})$ does not flatten out because the thermal conductivity "turns on" near T_c.

One might attempt to construct a myriad of scenarios by which $T_{eff}(I_{Bias})$ might be modeled. Instead, I will focus on a particular model which gives a reasonably good and consistent quantitative prediction for the effective temperatures observed in the various devices I measured. This model, the hot electron model for the heating of normal

metals at low temperatures, has been studied theoretically by several authors [71, 75, 76], and its predictions have been experimentally verified in several systems. The first experimental investigation of the effect in thin films was done by Roukes et al [71]. Here at Berkeley it was studied by Wellstood et al. because of its implications for the performance of DC SQUID based amplifiers operating at millikelvin temperatures [69, 70].

The essence of the model is to treat the electron gas and the phonon gas as separate systems, connected by the electron-phonon interaction. The electron and phonon systems each have their own distinct temperatures T_e and T_{ph}, respectively. Consider one of the thin-film resistive leads, which carries a current I. A voltage V develops across the lead, and power P = IV is dissipated in the lead. The energy dissipated through the ohmic resistance enters the electronic system first. Energy is then transferred to the phonon system through the electron-phonon interaction. The phonon system, which is strongly coupled to the mixing chamber [69], acts as a thermal reservoir at temperature $T_{ph} \approx T_{mix}$. For an electron gas at temperature T_e, the rate of energy loss by emission of phonons scales as T_e^5, as can be understood by the following argument: The characteristic frequency ω_{ph} of the emitted phonons is $\omega_{ph} = k_B T_e/\hbar$, and the energy of the phonon is proportional to ω_{ph}. For sufficiently low temperatures (much less than the Debye temperature), the number of available phonon states is proportional to ω_{ph}^3. Finally, in the deformation potential approximation, the electron-phonon coupling constant is proportional to ω_{ph}. Using Fermi's Golden Rule one obtains an emission rate proportional to ω_{ph}^5 and thus to T_e^5. This emission rate becomes sufficiently weak at low temperatures that the electron gas heats up to a temperature $T_e >> T_{ph}$. The expression for the relationship between the applied power P and the temperatures T_e and T_{ph} in a bulk approximation is

$$\frac{P}{\Omega} = \Sigma\left(T_e^5 - T_{ph}^5\right) \qquad (6\text{-}3)$$

where Ω is the volume of the metal, and Σ is a constant which is material dependant. While Eq. (6-3) is valid for all bulk samples at low temperatures, typically the effect becomes significant ($T_e >> T_{ph}$) in thin-film systems where P/Ω is very large. Wellstood [69] found $\Sigma = 2 \times 10^9$ W/m^{3}K^5 for the CuAu alloy commonly used in SQUID shunts, while Kautz et al. [72] obtained the best modeling of their Al (driven normal by a magnetic field) Coulomb-blockade electrometer by using $\Sigma = 2 \times 10^8$ W/m^{3}K^5.

I can apply Eq. (6-3) to obtain T_e as an estimate of the effective temperature of the thin-film normal-metal leads connected to my devices. Using measured lead resistances and measured geometry of the leads (both found in Table 6-1), and using Σ as an adjustable parameter, I obtain $T_{eff}(I_{Bias})$ for devices A, B, and C. Plotted in Fig. 6-8 are $T_e(I_{Bias})$ curves obtained by using $\Sigma = 7.6 \times 10^{10}$ W/m^{3}K^5 with $T_{ph} = 26$ mK and $T_{ph} = 300$ mK, which were the temperatures of the mixing chamber when the corresponding data were taken. I find that the theoretical curves reproduce the general trends of the data but give a temperature which rises too fast as the bias current is increased. Similarly, the $T_{ph} = 300$ mK curve is not as flat as the corresponding data. I obtained similar results for devices A and C, illustrated in Fig. 6-9. The data for device A were best fit using $\Sigma = 1.1 \times 10^{11}$ W/m^{3}K^5, while the data for device C were best fit using $\Sigma = 5 \times 10^{10}$ W/m^{3}K^5. Although the values of Σ used to obtain fits for devices A, B, and C were factors of 38, 55, and 25 larger than the value measured by Wellstood for CuAu, respectively, one should note that these values represent factors of only 1.9 to 2.2 in T_e. The values of Σ also show great consistency with each other considering that, among these three devices, the ratios of resistance of the leads to their volume varies from 5.6×10^{22} Ω/m^3 to 3.1×10^{25} Ω/m^3. Comparison of the values of Σ found experimentally for Al and CuAu show that material variations could easily explain differences in Σ of this magnitude.

What could account for the differences between the hot electron model prediction $T_e(I_{Bias})$ and the measured $T_{eff}(I_{Bias})$? Perhaps it would be best to take a step backward

to try first to understand more precisely what might define a so-called effective temperature. Suppose, according to the hot electron model, that the conduction electrons in the leads are hot, while the phonons are not. Because it is the electron gas which has an associated ohmic resistance, it is the temperature T_e which determines the magnitude of the Johnson current noise produced in the leads. In the RSJ model of a Josephson junction in thermal equilibrium at temperature T, the temperature parameter affects the junction dynamics by the inclusion of a white noise term I_N of magnitude given by the Nyquist theorem which is added to the steady bias current I_{Bias}, as described in Chapter 3. Thus we can see that, even though the body of the device may be physically at a temperature $T_{ph} \approx T_{mix}$ which is quite cold, it may behave dynamically as the RSJ model predicts for a junction at temperature $T = T_e$. This picture is supported by my observation that there was no reduction in the superconducting energy gap at high bias currents.

Given this picture of the effective temperature generation, one realizes that differences between the prediction of the hot electron model and the effective temperature inferred from the data may depend on several complex issues. First of all, one might question how well the bulk model for the hot electron effect approximates the real system from a geometrical point of view. Wellstood [69] has discussed in detail the results of spatial effects in the hot electron model. Although they illustrate much of the physics of the transport of the hot electrons, these models can only be quantitatively applied to systems of simple geometry. Secondly, one must consider how much of the noise produced in the leads is effectively coupled to the junction, and how much is shunted by self-capacitance within the circuit. Finally, as discussed earlier, one can model devices in this parameter range quantitatively only through elaborate extensions of the RSJ model, therefore a simple scalar temperature is most likely insufficient to parameterize the complex dynamics of this system. Since all of these issues are of great complexity, they

most likely cannot be resolved without a more detailed quantitative study of these and related systems.

One final conclusion may be drawn by studying the effective temperature analysis presented in this chapter. It seems that Eq. (3-7) for the escape rate retains its validity for all three devices A, B and C. This is remarkable because the ranges of reduced current s for which switching occurred were quite different for the devices. For example, device B switched at approximately $s = 0.36$ while device A switched at the much smaller value $s = 0.06$. A look at the washboard potential reveals that for $s > 0.216$ there is a single energy barrier for escape to the 1-state, while for $s = 0.06$ there are multiple barriers. Initially I had suspected the downward curvature observed in the escape rates was caused by the onset of multiple barrier effects as one went to smaller values of bias current and thus to smaller values of s. However, I failed in all attempts to model this in a way that reproduced the trends in the data. Given the overall success of the thermal activation formula used in conjunction with a hot electron model for providing a current-dependent effective temperaure, I can conclude that the presence of multiple barriers does not play a dominant role in determining the escape rate in the high temperature limit.

CHAPTER 7

Conclusion

Although the experimental investigation presented in this thesis failed in its goal of observing a signature of resonant tunneling, it did reveal some important general features of superconducting devices of very small capacitance operating at low temperatures, and served to identify specific problems which need to be addressed in order to further pursue the goal of observing resonant tunneling.

In this chapter I wish to first explore the possibility of using minor variations of the present approach in order to avoid the problem of the heating of the isolation resistor. Then I will outline some experimental tests designed to obtain better quantitative understanding of the resistor heating. Next I will describe theoretical work which needs to be undertaken, first to put the results already obtained in this experiment on a firmer quantitative ground, and secondly, to advance the quantum theory of resonant tunneling, especially as it is affected by dissipation.

7.1 Can Hot Leads Be Avoided?

The primary roadblock to observing resonant tunneling using my adopted approach is the heating of the on-chip thin film resistors by the bias current. The question is, can this heating be avoided by making some minor change of either the parameters of the device or the parameters or design of the resistor?

First, consider a change in the capacitance C or the critical current I_c. Since the resonant tunneling effect will only occur for $\nu \geq 1.7$, and because inter-well coupling will be suppressed in the large ν limit, I conclude that the value of ν is constrained to values near those it assumed in the devices already tested, with $\nu \approx 4$ a good value to aim for specifically. To avoid heating, one should reduce the value of the bias current required, which is determined by the resonance current $I_m^{res} = I_c m/\pi\nu$ and which thus scales with I_c for fixed ν. The hot electron theory for the heating of the resistors then predicts that the effective temperature T_{eff} will scale roughly as $T_{eff} \sim I_c^{2/5}$. However, since $\nu \sim (I_c C)^{1/2}$ and is held fixed while I_c and C are varied, the plasma frequency will vary in proportion to I_c. Because the plasma frequency determines the energy level spacing, $\hbar\omega_p/k_B$ must be kept larger than the effective temperature. By examining Table 4-1, which displays the values of $\hbar\omega_p/k_B$ for device A, and Fig. 6-9 (a), which displays the observed effective temperature of this device, one can see that these quantities were comparable. As I_c is lowered, the level spacing will decrease much faster than the effective temperature, and, perhaps contrary to intuition, the heating problem is actually made worse. Thus, there is little advantage to be gained by changing I_c or C.

Next, consider the possibility of changing the resistor itself, first by substituting a material of higher resistivity for the SiCr alloy. For a resistor with a uniform cross section of area A and length Λ carrying a fixed bias current, the hot electron model predicts T_{eff} will depend on the resistivity ρ and the cross sectional area as $T_{eff} \sim (\rho/A^2)^{1/5}$. Meanwhile, in the high frequency limit, the impedance Z_{lead} of the lead

scales as $Z_{lead} \sim (R_L/C_L)^{1/2} \sim (\rho/A)^{1/2}$, assuming the capacitance does not vary much if A is varied by v ying the film thickness. It is clear from these scaling laws that it is difficult to reduce the temperature T_{eff} without reducing the lead impedance as well. One can only accomplish this by increasing both ρ and A while keeping the ratio ρ/A constant. In this case the effective temperature is very weakly dependent on ρ as $T_{eff} \sim (1/\rho)^{1/5}$. Thus, a factor of 32 increase in resistivity results in only a factor of 2 in the reduction of the effective temperature. Tests by Andrew Cleland indicate that flash evaporating a SiO-Cr sinter which is 50% Cr by weight produces films with resistivities which are about a factor of 3 to 4 larger than that produced by the SiO-Cr sinter I used, which was 65% Cr by weight. This represents only a small increase in resistivity. For metal/semiconductor alloys too rich in the semiconductor material, conduction is by thermally activated carriers which freeze out at low temperatures, making these materials unacceptable for this application. I do not know of any other materials which have significantly higher resistivity which also satisfy the requirement of conduction at low temperatures. Thus, changing the resistor material is an unlikely solution to the heating problem.

The geometry I used for the resistor was a line of uniform cross section. There is a possibility that a geometry where the cross section increases with the distance from the SQUID could be used in such a way that a lower effective temperature is realized while presenting the same impedance to the SQUID. This would not be possible if the resistor were in thermal equilibrium at a uniform temperature, for the temperature and the impedance seen by the SQUID would completely determine the current noise introduced to the SQUID. However, in this case the effective temperature will vary as a function of distance from the SQUID, and segments of the resistor with wider cross section will be colder and will thus generate less Nyquist noise where the resistor connects to the SQUID. It is conceivable that this increase of the cross section with distance from the device could be accomplished without reducing the impedance Z_{lead} significantly,

because at high frequencies only a small segment of the resistor contributes to the impedance. For example, at the plasma frequency of device A, a 3 μm segment of its isolation resistor would present approximately the same impedance as the full length of the resistor. A model to determine the impedance and effective temperature of a resistor with increasing cross section could be devised and its treatment of the hot electron effects should include the spatial effects described by Wellstood [69]. I have not yet pursued an analysis of this sort.

Finally, one might consider a pulsed measurement of the switching current where the current is very quickly increased from zero current so that the device switches before the electron gas in the resistor heats up. However, because the volume of the resistor is small, the heat capacity of the electron gas is also small, and the heating of the electrons takes very little time. For the isolation resistors of device A, I have estimated that a bias current pulse equal in magnitude to the typical switching currents observed in that device would heat the resistor to half its final effective temperature in a few nanoseconds. This is a time scale much shorter than the lifetime of the 0-state, and so a measurement of this nature would not avoid heating.

7.2 Suggestions For Further Research

In my analysis of my experimental data, the effective temperature was inferred from the switching characteristics of the device. This method of obtaining the temperature from measurements of the escape rate possesses some inherent inaccuracy, because the thermal activation formula given by Eq. (3-7) is not necessarily exact and is in fact probably oversimplified, and because the escape rate depends on the inverse temperature exponentially, which serves to magnify any errors in the formula or measurements. Thus, an important next experimental step would be to make careful direct measurements of the temperature of the electron gas of the resistors using noise thermometry. This would confirm the hot electron behavior, provide a more accurate measurement of the effective temperature, and perhaps give a better understanding of the geometrical effects involved in the heating, thereby allowing the possibility of intelligent modifications to the resistor design. The process of carrying out a noise thermometry measurement is the subject of Appendix A.

The primary need for further theoretical work at this point is to provide accurate quantitative modeling of the device behavior as a support to further experimental research. The first step would be to perform detailed modeling along the lines of the Kautz and Martinis model in order to understand the complex classical behavior of the devices I have tested, and devices proposed for testing in the future. I envision a Monte Carlo simulation of the combined system of the SQUID, the isolation resistors, and the measurement setup, which utilizes a more accurate model of the heating in the resistors obtained through the noise thermometry experiment described above. The analysis of Section 7.1 showed that it is unlikely that a major improvement could be made by any single change in the design of the device or resistors. However, by using this simulation as a tool one could explore the effects of a combination of several minor variations in device and resistor design, and perhaps an accurate simulation would also reveal that

some of the constraints imposed by the analysis presented in this thesis may be relaxed enough that it is possible to move to within the limit where resonant tunneling could be observed.

While the quantum theory presented in Chapter 2 gives an overview of what sort of effects one could expect to observe which arise from resonant tunneling, some features must be added to the theory before firm quantitative predictions can be made. I believe the primary deficiency of the theory is the proper treatment of dissipation and the effects of temperatures greater than zero. The most significant effect that dissipation and nonzero temperature have on the system is to cause direct incoherent relaxation of the system from the ground state of one well to the ground state of the adjacent well. These effects have been thoroughly studied by several authors for the double well system which is illustrated in Fig. 7-1 (a). A review of the theoretical studies of this system is given by ref. [40]. The assumption made in these studies is that the excited states in each well can be neglected because they are of energies which are much greater than the available thermal energy, the energy difference between the two local ground states, and the tunnel splitting between the states. While the analysis is quite complex, the qualitative result for ohmic damping is that the coherent oscillations characteristic of resonance occur between the two states only for very low damping and very low temperatures. Eventually, these oscillations are damped out, and the system relaxes to a steady-state configuration which also depends on the damping and temperature. While the behavior of the two well system gives one some feeling for the effects of damping and nonzero temperature on nearly degenerate states which are weakly coupled, the two well system is far enough removed from the resonant tunneling system I have studied for these results to be applied.

For this reason, I propose a theoretical study of the asymmetric two well system illustrated in Fig. 7-1 (b). In this model the first excited state B of the right well is nearly degenerate with the ground state A of the left well. Solving the dynamics of this system

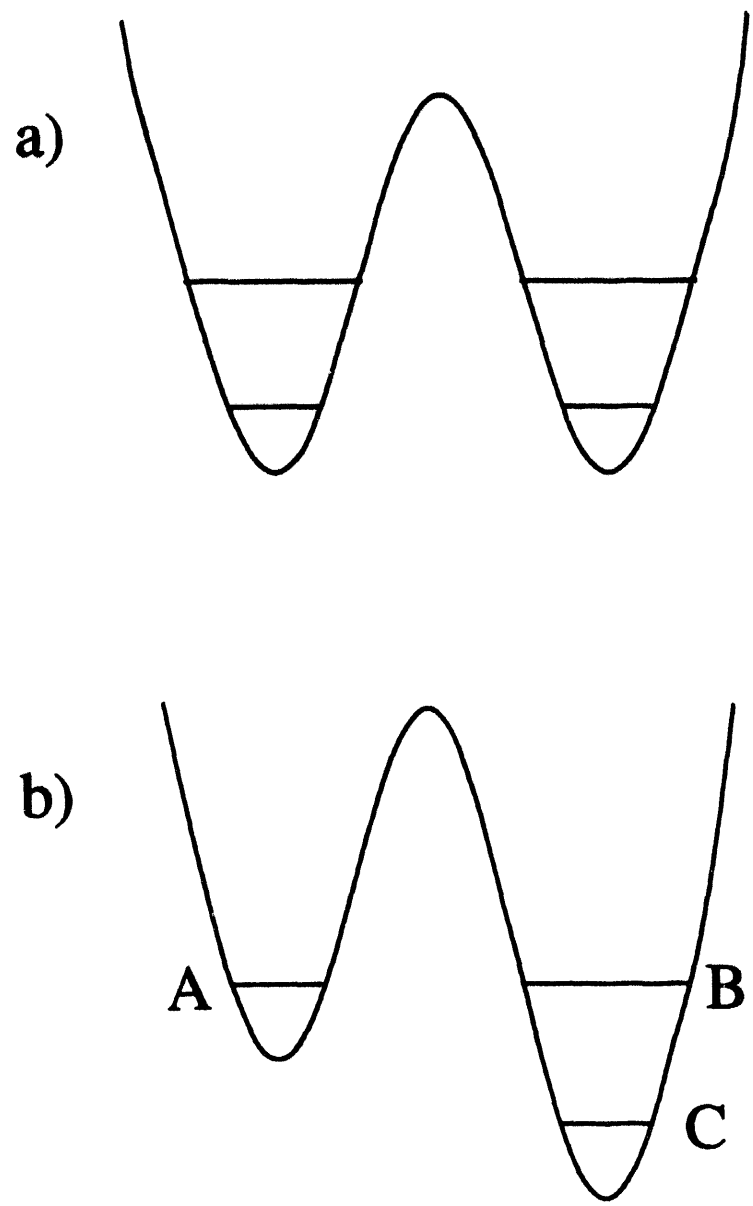

FIGURE 7-1. (a) Two state system studied in ref. [40], represented as a double well. The excited states in each well are assumed to be of sufficiently high energy that they may be ignored in the analysis. (b) Three state system proposed for theoretical study. States A and B are nearly degenerate. Damping in the system creates a coupling which induces direct transitions from state A to state C. This process competes with the process which involves a resonant transition from A to B followed by a decay transition from B to C.

should reveal the competing effects of the resonant coupling between A and B and the incoherent coupling between the ground states A and C provided by dissipation.

To obtain a sense of the importance of this incoherent relaxation, I have estimated the rate Γ_{relax} of relaxation of the system shown in Fig. 7-1 (b) from state A directly to state C using the perturbation theory of damping described in Section 3.2. I wish to compare this result to the rate $\Gamma_{RT/decay} = \omega_p\gamma/2$, where γ is given by Eq. (2-39), which is the rate of steady motion down the washboard potential achieved through resonant tunneling and decay, shown as path A in Fig. 1-1. In order to make this comparison I assume that the double well potential is equal to the washboard potential over the region of the two wells, and define the parameters of the three state system in an fashion analogous to the parameters for the RSJ model which were given in Chapter 2. In actual inverse time units, I obtained the relaxation rate

$$\Gamma_{relax} = \frac{\pi\omega_p}{4}\frac{R_Q}{R}\Delta^2 \ . \tag{7-1}$$

As usual, ω_p is the plasma frequency, R is the shunt resistance which provides the damping, and R_Q is the quantum of resistance. Here, however, $\Delta/2$ is the matrix element of the Hamiltonian between states A and C in units of $\hbar\omega_p/2$, which is distinct from the matrix element between states A and B, which I again denote as $\Delta_1/2$ as in Chapter 2. Values for the coupling Δ_1 and the decay rate Γ_d are typically in the limit $\Delta_1 << \Gamma_d$, so the rate $\Gamma_{RT/decay}$ is given by

$$\Gamma_{RT/decay} = \frac{\pi\omega_p}{4}\nu\frac{R}{R_Q}\Delta_1^2 \ . \tag{7-2}$$

The expressions for the rates Γ_{relax} and $\Gamma_{RT/decay}$ are very similar. Apart from a factor of ν and differences in the couplings Δ and Δ_1, the important distinction between these

rates is that Γ_{relax} is proportional to R_Q/R, whereas $\Gamma_{RT/decay}$ is proportional to R/R_Q. While my estimate for Γ_{relax} is admittedly crude, the point to be made is that although these rates may be comparable under some circumstances, I expect that by decreasing the damping the incoherent relaxation may be suppressed while the resonant transition rate is enhanced. A full theoretical analysis of the three state system is necessary to obtain accurate predictions regarding these effects, which have important implications for the observation of resonant tunneling.

7.3 Epilogue

The subject of resonant tunneling in a current biased Josephson junction remains an interesting problem, primarily because it is simple in conception, yet as one looks at the problem with greater scrutiny, its complexity does not cease to grow.

The research presented in this thesis is a good example of the complementary development of theory and experiment. Although my experimental work failed to produce a signature of resonant tunneling and thus provide a test of the theory I developed, I did achieve my goals which were twofold: first, to perform a straightforward test based on the predictions of my theory for whether the effect was readily observable, and second, to direct future theoretical research toward the most crucial areas of study.

The heating of the isolation resistors caused by the hot electron effect serves as an important guide to any experimenter operating thin film devices at millikelvin temperatures. Although this heating creates a substantial difficulty for advancing the experiment to observe resonant tunneling using my approach, the possibility remains open for taking other approaches to achieving this goal.

APPENDIX A

Noise Thermometry

According to the Nyquist theorem, the voltage across a resistor R_L which is in thermal equilibrium at temperature T_L randomly fluctuates. This is modeled as a fluctuating voltage source V_L in series with the resistor R_L. The noise power spectrum of these fluctuations is frequency independent, with mean square fluctuations per unit bandwidth given by

$$S_{V_L} = 4k_B T_L R_L \ . \qquad \text{(A-1)}$$

Thus, through a measurement of the noise power, the temperature T_L can be obtained.

This method of measuring the temperature is referred to as noise thermometry, and it is a technique of general usefulness. Specifically, it was used by Wellstood [69] for measurements of the hot electron effect in thin films of AuCu, the material commonly used to form resistive shunts for SQUID magnetometers. This was also the method I used in an attempt I made to directly measure the effective temperature $T_{eff}(I_{Bias})$ of the isolation resistors as a function of the DC bias current I_{Bias} they carried.

The switching behavior discussed in Chapter 6 implied that the effective temperature was on the order of 0.5 K to 1 K. Assuming a temperature of T_L = 1 K to be definite, the noise power produced by a resistor of value R_L = 1.5 MΩ (which was approximately the series resistance of two of the isolation resistors) should be 8.3×10^{-17} V^2/Hz.

I experienced several difficulties while carrying out this noise measurement. Some of these problems were associated with my particular setup, while others were more fundamental. First of all, the PAR 113 amplifier I used had an input noise power of about 5.6×10^{-17} V^2/Hz, which was comparable to the noise level I expected to measure. Through the use of signal averaging, this problem could conceivably be minimized. The second main problem was more fundamental in nature, and that was the fact that a current source had to be used to provide the DC bias current which was sufficiently quiet that it did not overwhelm the noise of interest generated by R_L.

To understand this, consider the circuit illustrated in Fig. A-1 (a). The resistor R_L and its associated noise source V_L is shown at the right of the circuit, and is at a temperature T_L. The current source supplying the current I_{Bias}, shown at the left of the Figure, is at the temperature T_B and has a finite impedance R_B. The current source also obeys the Nyquist theorem, and can be modeled as having a fluctuating current source I_N which has the noise power spectrum

$$S_{I_B} = \frac{4k_B T_B}{R_B} \quad . \tag{A-2}$$

The fluctuating voltage measured at the terminals V_{out} shown in the figure contains contributions from both V_L and I_B. The total noise power which appears at the output terminals is

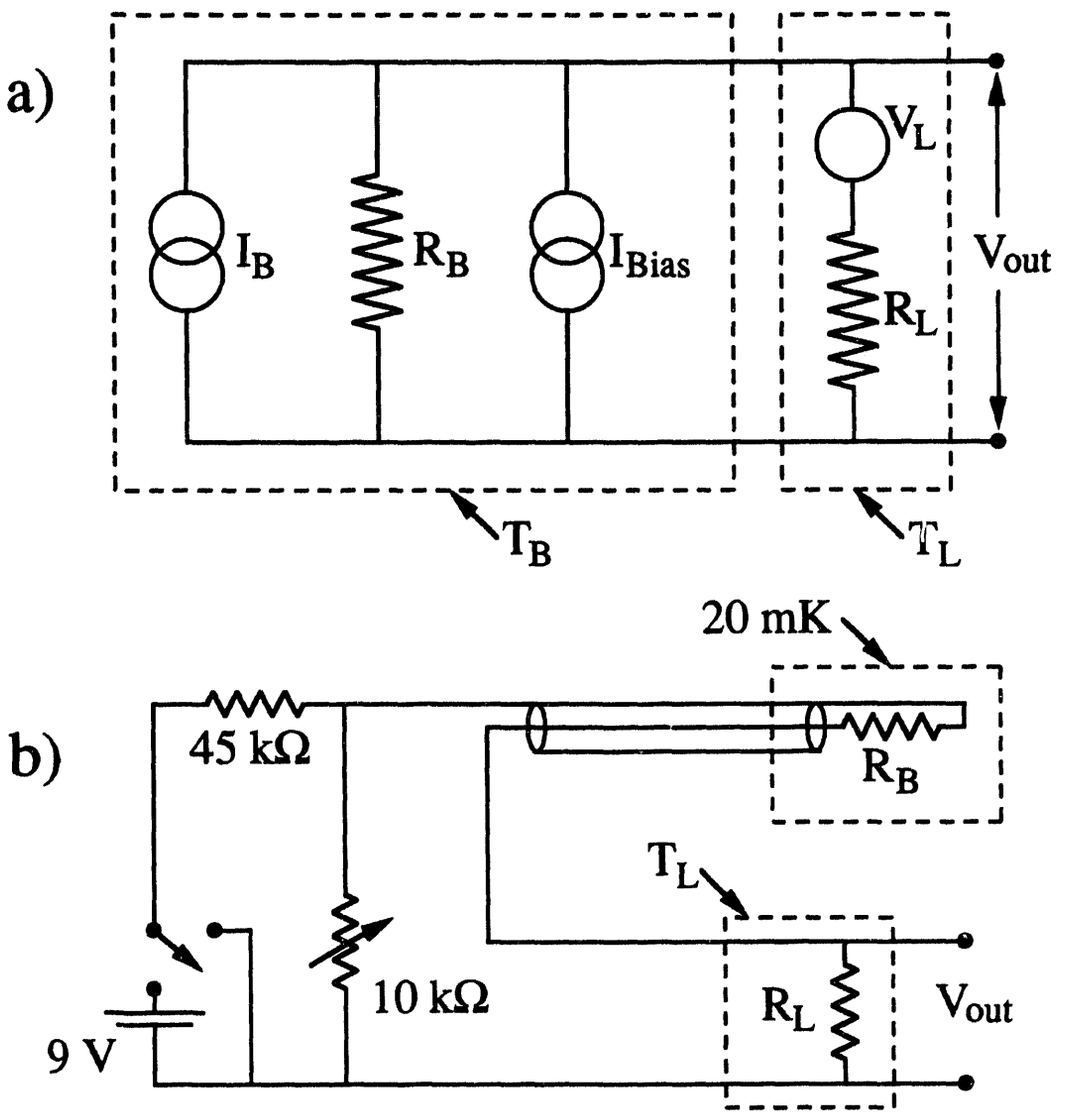

FIGURE A-1. (a) Circuit diagram for a noise thermometry measurement of the effective temperature of the resistor R_L, shown at the right and assumed to be at a temperature T_L. A DC current bias I_{Bias} is provided by the current source shown at the left of the Figure, which has a finite impedance R_B and is at the temperature T_B. (b) Circuit diagram of an actual circuit used in an attempt to measure the effective temperature of the isolation resistors of device A.

$$S_{V_{out}} = \left(S_{V_L} + S_{I_B} R_L^2\right)\left(\frac{R_B}{R_L + R_B}\right)^2 ,$$

which can be written in terms of S_{V_L} as

$$S_{V_{out}} = S_{V_L}\left[1 + \frac{T_B R_L}{T_L R_B}\right]\left(\frac{R_B}{R_L + R_B}\right)^2 . \qquad \text{(A-3)}$$

In order to avoid the detrimental effects of the current source noise, the second term in the square brackets must be made negligible. This precludes the use of a room temperature current source because the large ratio of T_B/T_L forces a choice of source impedance $R_B >> 450$ MΩ, which creates great experimental difficulty. The alternative is to use a cold current source.

For this reason I attempted to use the circuit setup shown in Fig. A-1 (b) with the bias resistor R_L = 100 MΩ located at the end of a long piece of coaxial cable so it could be submerged in liquid He contained in a storage dewar separate from the dilution refrigerator cryostat. Unfortunately, the problem with this setup was that the microphonic current noise generated in the coaxial cable and the cryostat wires combined with the high impedance of R_L created too much noise to observe the desired signal. Substitution of a 10 MΩ resistor for R_L did not improve the situation much. Because these tests were performed while the dilution refrigerator remained running with the device *in situ*, I was not able to set up a circuit which avoided long cable lengths for the express purpose of making this noise measurement.

Instead, I turned to the current-sense resistor already located on the chip carrier, which was at a temperature of approximately 20 mK and had a resistance of 1.3 MΩ. I used this resistor as the bias resistor R_B. Unfortunately, the small value of R_B meant that the term in the right parenthesis in Eq. (A-3) was equal to about 0.2, which made the

signal at V_{out} even weaker compared to the amplifier noise. Also, some microphonics generated by the cryostat leads remained to obscure the signal further.

In spite of these difficulties, the measured noise spectrum was found to display a definite systematic increase when a bias current of about 15 nA was applied, compared to the noise spectrum observed when zero bias current was applied. The noise power increase was about 2.1×10^{-17} to 3.5×10^{-17} V^2/Hz, starting with a base noise power of about 1.6×10^{-16} V^2/Hz. This increase is not inconsistent with the estimated noise power increase of 1.7×10^{-17} V^2/Hz based on an assumed effective temperature of 1 K for R_L.

A carefully designed measurement setup could be devised which avoids the problems described above by using a larger bias resistance at low temperatures and a quieter preamplifier, with the circuit designed to reduce the microphonic pickup as much as possible.

REFERENCES

1. A. J. Leggett, Prog. Theor. Phys. (Suppl.) **69**, 80 (1980).

2. A. J. Leggett, in *Essays in Theoretical Physics in Honour of Dirk Ter Haar*, (Pergamon, Oxford, 1984), p. 95.

3. W. C. Stewart, Appl. Phys. Lett. **12**, 277 (1968).

4. D. E. McCumber, J. Appl. Phys. **39**, 3133 (1968).

5. J. M. Martinis, M. H. Devoret, and J. Clarke, Phys. Rev. B **35**, 4682 (1987).

6. R. V. Voss and R. A. Webb, Phys. Rev. Lett. **47**, 265 (1981).

7. S. Washburn, R. A. Webb, R. V. Voss, and S. F. Faris, Phys. Rev. Lett. **54**, 2712 (1985).

8. L. D. Jackel, J. P. Gordon, E. L. Hu, R. E. Howard, L. A. Fetter, D. M. Tennant, R. W. Epworth, and J. Kurkijarvi, Phys. Rev. Lett. **47**, 697 (1981).

9. A. N. Cleland, J. M. Martinis, and J. Clarke, Phys. Rev. B **37**, 5950 (1988).

10. D. Esteve, J. M. Martinis, C. Urbina, E. Turlot, M. H. Devoret, H. Grabert, and S. Linkwitz, Phys. Scrip. **T29**, 121 (1989).

11. K. K. Likharev and A. B. Zorin, J. Low Temp. Phys. **59**, 347 (1985).

12. M. Iansiti, A. T. Johnson, W. F. Smith, H. Rogalla, C. J. Lobb, and M. Tinkham, Phys. Rev. Lett. **59**, 489 (1987).

13. M. Iansiti, M. Tinkham, A. T. Johnson, W. F. Smith, and C. J. Lobb, Phys. Rev. B **39**, 6465 (1989).

14. K. K. Likharev, *Dynamics of Josephson Junctions and Circuits* (Gordon and Breach Science Publishers, New York, 1986).

15. N. Hatakenaka and S. Kurihara, Solid State Comm. **64**, 943 (1987).

16. R. F. Kazarinov and R. A. Suris, Fiz. Tekh. Poluprovodn. **6**, 148 (1972) [Sov. Phys.-Semicond. **6**, 120 (1972)].

17. L. L. Chang, L. Esaki, W. E. Howard, and R. Ludeke, J. Vac. Sci. Technol. **10**, 655 (1973).

18. D. V. Averin and K. K. Likharev, in *Quantum Effects in Small Disordered Systems,* edited by B. L. Altschuler, P. A. Lee, and R. A. Webb (Elsevier, Amsterdam, 1991).

19. J. Kondo, in *Superconducting Materials,* edited by S. Nakajima and H. Fukuyama (Publication Office, Jpn. J. Appl. Phys., Tokyo, 1988).

20. K. Mullin, D. Loss, and H. T. C. Stoof, Phys. Rev. B **47**, 2689 (1993).

21. N. Hatakenaka and S. Kurihara, Solid State Comm. **68**, 131 (1988).

22. A. V. Zhuravlev and A. B. Zorin, **16**, 184 (1990) [Sov. J. Low Temp. Phys. **16**, 102 (1990)].

23. M. H. Devoret, D. Esteve, J. M. Martinis, and C. Urbina, Phys. Scrip. **T25**, 118 (1989).

24. A. N. Cleland, J. M. Schmidt, and J. Clarke, Phys. Rev. Lett. **64**, 1565 (1990).

25. A. N. Cleland, J. M. Schmidt, and J. Clarke, Phys. Rev. B **45**, 2950 (1992).

26. R. L. Kautz and J. M. Martinis, Phys. Rev. B **42**, 9903 (1990).

27. J. M. Schmidt, A. N. Cleland, and J. Clarke, Phys. Rev. B **43**, 229 (1991).

28. A. O. Caldeira and A. J. Leggett, Phys. Rev. Lett. **46**, 211 (1981).

29. A. O. Caldeira and A. J. Leggett, Annals of Physics **149**, 374 (1983).

30. V. Ambegaokar and A. Baratoff, Phys. Rev. Lett. **10**, 486 (1963).

31. *Handbook of Mathematical functions*, edited by M. Abromowitz and I. A. Stegun, (Dover, New York, 1969), Chap. 20.

32. D. Esteve, M. H. Devoret, and J. M. Martinis, Phys. Rev. B **34**, 158 (1986).

33. A. Barone and G. Paterno, *Physics and Applications of the Josephson Effect* (Wiley, New York, 1982).

34. V. Ambegaokar and B. I. Halperin, Phys. Rev. Lett. **23**, 1364 (1969).

35. P. A. Lee, J. Appl. Phys. **42**, 325 (1971).

36. Y. M. Ivanchenko and L. M. Zil'berman, Zh. Eksp. Teor. Fiz. **55**, 2395 (1968) [Sov. Phys.-JETP **28**, 1272 (1969)].

37. A. C. Biswas and S. S. Jha, Phys. Rev. B **2**, 2543 (1970).

38. H. A. Kramers, Physica (Amsterdam) **7**, 284 (1940).

39. P. Silvestrini and R. Cristiano, Nuovo Cimento **9**, 1433 (1987).

40. A. J. Leggett, S. Chakravarty, A. T. Dorsey, M. P. A. Fisher, A. Garg, and W. Zwerger, Rev. Mod. Phys. **59**, 1 (1987).

41. A. Schmid, Phys. Rev. Lett. **51**, 1506 (1983).

42. M. P. A. Fisher and W. Zwerger, Phys. Rev. B **32**, 6190 (1985).

43. F. Guinea, V. Hakim, and A. Muramatsu, Phys. Rev. Lett. **54**, 464 (1985).

44. V. Hakim and V. Ambegaokar, Phys. Rev. A **32**, 423 (1985).

45. T. A. Fulton and L. N. Dunkleberger, Phys.Rev. B **9**, 4760 (1974).

46. S. Han, J. Lapointe, and J. E. Lukens, Phys. Rev. Lett. **63**, 1712 (1989).

47. S. Han, J. Lapointe, and J. E. Lukens, Phys. Rev. Lett. **66**, 810 (1991).

48. C. D. Tesche, J. Low Temp. Phys. **44**, 119 (1981).

49. E. Ben-Jacob, D. J. Bergman, Y. Imry, B. J. Matkowsky, and Z. Schuss, J. Appl. Phys. **54**, 6533 (1983).

50. Z. Schuss, SIAM Rev. **22**, 119 (1980).

51. T. S. Tighe, Ph.D. Thesis, (Harvard University, 1993).

52. A. W. Lichtenberger, C. P. McClay, R. J. Mattauch, and M. J. Feldman, IEEE Trans. Magn. **MAG-25**, 1247 (1989).

53. J. M. Jaycox and M. B. Ketchen, IEEE Trans. Magn. **MAG-17**, 400 (1981).

54. A. N. Cleland, Ph.D. Thesis, (University of California, Berkeley, 1991).

55. G. J. Dolan, Appl. Phys. Lett. **31**, 337 (1977).

56. R. E. Howard, E. L. Hu, L. D. Jackel, L. A. Fetter, and R. H. Bosworth, Appl. Phys. Lett. **35**, 879 (1979).

57. *Introduction to Microlithography*, edited by L. F. Thompson, C. G. Wilson, and M. J. Bowden (American Chemical Society, Washington, D. C., 1983).

58. M. Hatzakis, J. Vac. Sci. Technol. **16**, 1984 (1979).

59. S. Mackie and S. P. Beaumont, Solid State Technol. **August**, 117 (1985).

60. G. H. Bernstein and D. A. Hill, Superlattices and Microstructures **11**, 237 (1992).

61. J. S. Greeneich, J. Electrochem. Soc. **122**, 970 (1975).

62. J. S. Greeneich, J. Vac. Sci. Technol. **16**, 1749 (1979).

63. Y. Todokoro, IEEE Trans. El. Dev. **ED-27**, 1443 (1980).

64. M. G. Rosenfield and A. R. Neureuther, IEEE Trans. El. Dev. **ED-28**, 1289 (1981).

65. G. I. Rochlin, Rev. Sci. Inst. **41**, 73 (1970).

66. J. R. Clem, IEEE Trans. Magn. **MAG-23**, 1093 (1987).

67. J. Clarke, W. M. Goubau, and M. B. Ketchen, J. Low Temp. Phys. **25**, 99 (1976).

68. D. Middleton, *An Introduction to Statistical Communication Theory* (McGraw-Hill, New York, 1960).

69. F. C. Wellstood, Ph.D. Thesis, (University of California, Berkeley, 1988).

70. F. C. Wellstood and C. Urbina, Phys. Rev. B, to be published.

71. M. L. Roukes, M. R. Freeman, R. S. Germain, R. C. Richardson, and M. B. Ketchen, Phys. Rev. Lett. **55**, 422 (1985).

72. R. L. Kautz, G. Zimmerli, and J. M. Martinis, to be published (1994).

73. B. L. Blackford and R. H. March, Can. J. Phys. **46**, 141 (1968).

74. R. L. Kautz, Phys. Rev. A **38**, 2066 (1988).

75. W. A. Little, Can. J. Phys. **37**, 334 (1959).

76. M. R. Arai, Appl. Phys. Lett. **42**, 906 (1983).

DATE
FILMED
9/7/94
END